
Towards Bottom-up Reconstitution of a Minimal Division Machinery: Characterization of FtsZ chimera protein in different membrane systems

Daniela Azucena García Soriano



2018

Towards Bottom-up Reconstitution of a Minimal Division Machinery: Characterization of FtsZ chimera protein in different membrane systems

Daniela Azucena García Soriano

Dissertation
an der Fakultät für Physik
der Ludwig-Maximilians-Universität
München

vorgelegt von
Daniela Azucena García Soriano
aus Puebla, Mexiko

München, den 27th September 2018

Erstgutachter: Prof. Dr. Petra Schulle

Zweitgutachter: Prof. Dr. Elena Conti

Drittgutachter: Prof. Dr. Ulrich Gerland

Tag der mündlichen Prüfung: 4th December 2018

A mi familia y a mi familia extendida en todo el mundo

Kurzfassung

Synthetische Biologie versucht lebende Materie unter einem technischen Ansatz zu charakterisieren und zu verstehen, um biologische Funktionen zu verbessern oder sogar neu zu erzeugen. Ein Hauptziel ist dabei die Entwicklung funktionaler Module welche sich zu einer minimalen Zelle kombinieren lassen. Solche Module bilden elementare biochemische und biophysikalische Prozesse von Grund auf ab, wobei synthetische oder organische zelluläre Komponenten kombiniert werden. Die daraus resultierenden Modellsysteme sollen essentielle Eigenschaften einer lebenden Zelle besitzen, also beispielsweise in der Lage sein, einen elementaren Stoffwechsel aufrechtzuerhalten oder auf äußere Reize reagieren können. Dadurch stellt die synthetische Biologie einen minimalen Rahmen zur Erforschung von biologischen Prozessen bereit, welche unabhängig von der Vielzahl, in einer lebenden Zelle, parallel auflaufender Reaktionen analysiert werden können. Sobald die zellulären Komponenten, wie Replikation, Metabolismus oder Zellteilung charakterisiert wurden, sollen diese langfristig in ein ganzes vom Menschen geschaffenes Gebilde zusammengefügt werden, welches leicht zu prognostizieren, zu manipulieren und zu kontrollieren ist.

Sich zu Teilen ist eine der grundlegendsten Eigenschaften lebender Zellen und wird durch eine gut organisierte Gruppe von Proteinen orchestriert. Dabei teilt sich eine Mutterzelle in zwei Hälften wobei das Erbgut und alle anderen Zellteile so verteilt werden, dass die neuen Tochterzellen überleben. In Bakterien, insbesondere *Escherichia Coli*, wird FtsZ als das wichtigste Protein für die Zellteilung angesehen. Im Rahmen dieser Arbeit wurde das FtsZ-Proteins als potentieller Bestandteil einer minimalen Teilungsmaschinerie in synthetischen Zellen untersucht. Ferner wurden Technologien zur Durchführung von In-vitro-Rekonstitutionsexperimenten in Kompartimenten zur Nachahmung einer künstlichen Zellhülle erarbeitet.

Zunächst haben wir das FtsZ-Protein mit einer membranspezifischen Anker konjugiert und näher charakterisiert. Hier waren unsere Hauptziele, die Mechanismen zu verstehen, die die Emergenz und stationäre Dynamik von chiralen FtsZ Wirbeln auf planaren Lipidmembranen bestimmen. Dazu untersuchten wir verschiedenen Faktoren, wie Membranbindung, laterale Wechselwirkungen und GTPase-Aktivität auf deren Einfluss auf die dynamischen Eigenschaften der FtsZ-Ringe zu untersuchen.

Zweitens werfen wir einen Blick auf neu entstehende Technologien, die nicht nur für FtsZ, sondern auch für verschiedene zelluläre Module und letztlich minimale Zellen implementiert werden könnten. Unter dem Ziel, unsere Untersuchungen in eine zellähnlichere Umgebung zu übertragen, wurden 3D-Umgebungen mit einer bakterienähnlichen Form für weitere Untersuchungen von FtsZ-Filamenten implementiert. Ebenso konnte festgestellt werden, dass noch einige Hürden für eine bessere Charakterisierung biologischer Prozesse

zu überwinden sind, die die Implementierung von Technologien zur schnellen Charakterisierung biologischer Systeme erfordern.

In der Gesamtheit bietet diese Arbeit eine detaillierte Untersuchung einer Komponente der Zellteilungsmaschinerie sowie die Implementierung verschiedener Technologien, um diese Studien in biomimetische Zellkompartimente zu integrieren.

Abstract

Synthetic biology aims to understand living matter under an engineering approach, improving or even generating new biological systems. In the protocell approach, the main goal is to produce life from very basic elements by means of a bottom-up perspective, combining synthetic or organic cellular components. Such life forms would possess some of the characteristics of a living cell, being capable to maintain an elemental metabolism and to respond to external stimuli. To obtain a minimal cell, functional modules are required and cell-free synthetic biology represents a minimal framework for the understanding of biological process outside the intrinsic noisy environment of cells. With the use of different technologies such as biomimetic membranes, cell-free expression reactions and microfluidics; modules such as replication, metabolism or cell division can be in depth characterized. Once cellular components are deeply characterised the ultimate goal is to build an entire man-made entity, that is easy to predict, manipulate and control.

Cell division is one of the most distinctive characteristics of living cells. The machinery has evolved into a well organised set of proteins which ultimate goal is to split a mother cell in half preserving DNA material in a way that the new daughter cells will survive. In the case of bacteria, and more specifically *Escherichia coli*, the main protein in charge of cell-division is FtsZ. Within the framework of a minimal cell, this thesis presents the efforts to characterise the FtsZ protein as a main component of a minimal division machinery in synthetic cells, and the implementation of technologies to take our *in vitro* reconstitution experiments in compartments that will mimic cellular properties.

Firstly, we characterised the FtsZ protein, using a membrane-targeted version. Here, our main goals were to understand the mechanisms governing the emergence and steady-state dynamics of FtsZ chiral vortices in supported bilayers and to characterize the different factors that play a role in the dynamic properties of the FtsZ rings on supported bilayers e.g. membrane binding, lateral interactions and GTPase activity.

Secondly, we have a look into nascent technologies that could be implemented for the study not only of FtsZ but also for different cellular modules and ultimate minimal cells. With the aim to take our studies into a more cell-like environment we implemented 3D environments, with a shape similar to bacteria, for the further study of FtsZ filaments. We also noticed that there are still some hurdles to overcome for a better characterization of biological process which motivate the implementation of technologies for the rapid characterization of biochemical systems.

The thesis as a whole, offers a detailed study of one component of the cell-division machinery and the implementation of different technologies to take these studies into biomimetic cellular compartments.

Publications and manuscripts

1. Ramirez D, **Garcia-Soriano, D. A.**, Raso A, Feingold M, Rivas G, Schwille P. (2016) Chiral vortex dynamics on membranes is an intrinsic property of FtsZ, driven by GTP hydrolysis. bioRxiv 079533; doi: <https://doi.org/10.1101/079533>
2. Ramirez-Diaz, D. A., **Garcia-Soriano, D. A.**, Raso, A., Mücksch, J., Feingold, M., Rivas, G., Schwille, P. (2018). Treadmilling analysis reveals new insights into dynamic FtsZ ring architecture. PLoS Biology. <https://doi.org/10.1371/journal.pbio.2004845>
3. Ramm, B., Glock, P., Mücksch, J., Blumhardt, P., Heymann, M., **Garcia-Soriano, D. A.**, Schwille, P. (2018) The MinDE system is a generic spatial cue for membrane protein distribution *in vitro*. Nature Communications. <https://10.1038/s41467-018-06310-1>
4. Jia, H., Kai, L., Heymann, M., **Garcia-Soriano, D. A.**, Härtel, T., Schwille, P. (2018) Light-induced Printing of Protein Structures on Membranes *in vitro*. (*in revision*)
5. **Garcia-Soriano, D. A.**, Raso, A., Heermann, T., Ramirez-Diaz, D. A., Feingold, M., Rivas, G., Schwille, P. Site directed mutagenesis, insertions and deletions to tune the treadmilling dynamics of FtsZ-YFP-mts rings. (*in preparation*)

Contents

| | |
|---|-------------|
| Kurzfassung | v |
| Abstract | vii |
| Publications | viii |
| 1 Introduction | 1 |
| 1.1 Cell division in bacteria | 1 |
| 1.1.1 Z-ring disassembly and constriction generation in cytokinesis | 3 |
| 1.1.2 The central component of bacterial cell division, FtsZ | 4 |
| 1.1.3 Membrane tethered FtsZ | 5 |
| 1.2 Biometric membranes for the study of Z-ring | 6 |
| 1.2.1 Z-ring reconstitution on biomimetic membranes | 8 |
| 1.3 Techniques to generate cell-like environments | 8 |
| 1.3.1 Cell-free protein synthesis | 8 |
| 1.3.2 Microfluidics | 11 |
| 1.3.3 Contained cell-free expression reactions | 11 |
| 2 Objectives | 13 |
| 3 Materials and Methods | 15 |
| 4 Treadmilling analysis reveals new insights into dynamic FtsZ ring architecture | 22 |
| 4.1 RESULTS | 24 |
| 4.1.1 Membrane-targeted FtsZ self-organizes into dynamic rotating vortices | 24 |
| 4.1.2 Surface FtsZ concentration -linked to Mg- critically modulates the emergence of dynamic chiral ring-like structures | 25 |
| 4.1.3 Directionality of vortices and destabilization of the trailing edge | 28 |
| 4.2 DISCUSSION | 32 |
| 5 Site directed mutagenesis, insertions and deletions to tune the treadmilling dynamics of FtsZ-YFP-mts rings | 37 |
| 5.1 RESULTS | 38 |

CONTENTS

| | | |
|----------|--|-----------|
| 5.1.1 | Inefficient membrane binding and absent of lateral interactions hinder FtsZ-ring formation | 38 |
| 5.1.2 | Mutations in the FtsZ GTPase domain have a direct effect on FtsZ ring treadmilling | 39 |
| 5.1.3 | Binding affinity of the membrane targeted sequences (mts) has a direct impact on FtsZ treadmilling | 41 |
| 5.1.4 | Treadmilling tuning by the presence of FtsZ-YFP-mts-His ₆ variant | 43 |
| 5.2 | DISCUSSION | 44 |
| 6 | Study of FtsZ chimera protein in cell-like environments | 47 |
| 6.1 | RESULTS | 48 |
| 6.1.1 | The synthesized FtsZ-YFP-mts is capable to form dynamic FtsZ-rings on planar bilayers | 48 |
| 6.1.2 | FtsZ-YFP-mts encapsulation in giant unilamellar vesicles: purified and synthesized protein showed different organization behaviour | 49 |
| 6.1.3 | Microfluidics traps to capture and deform spherical droplets into a cell-like shape | 51 |
| 6.2 | DISCUSSION AND OUTLOOK | 54 |
| 7 | Rapid characterization of FtsZ in a droplet barcoding microfluidics system | 57 |
| 7.1 | RESULTS | 58 |
| 7.1.1 | Implementation and troubleshooting of a droplet barcoding microfluidics set-up | 58 |
| 7.1.2 | Titration of Mg ²⁺ and Ficoll for FtsZ-YFP-mts polymerization inside surfactant droplets | 61 |
| 7.1.3 | Titration of Mg ²⁺ for optimal cell-free expression of GFP | 65 |
| 7.2 | DISCUSSION AND OUTLOOK | 67 |
| A | Appendix to chapter IV | 78 |
| A.1 | Figures | 78 |
| A.2 | Scripts | 81 |
| B | Appendix to chapter V | 89 |
| B.1 | Figures | 89 |
| B.2 | Tables | 92 |
| C | Appendix to chapter VI | 93 |
| C.1 | Figures | 93 |
| D | Appendix to chapter VII | 94 |
| D.1 | Figures | 94 |
| D.2 | Scripts | 96 |

CONTENTS

Acronyms

106

List of Figures

| | | |
|-----|---|----|
| 1.1 | E. coli Z-ring. | 2 |
| 1.2 | Main regulators for FtsZ positioning | 3 |
| 1.3 | FtsZ main protein domains | 4 |
| 1.4 | Membrane-targeted FtsZ protein | 6 |
| 1.5 | FtsZ on biomimetic membranes | 9 |
| 1.6 | Main components of cell-free expression reaction | 10 |
| 4.1 | Nucleation and growth of FtsZ filaments into rings on supported lipid bilayers | 24 |
| 4.2 | Representative images of FtsZ-YFP-mts at low and high protein concentrations | 26 |
| 4.3 | Dependence of FtsZ-YFP-mts vortex formation on protein surface concentration. | 27 |
| 4.4 | Free Mg^{2+} regulates protein surface concentration | 28 |
| 4.5 | Effect of GTP concentration on the FtsZ-YFP-mts rings formation. | 29 |
| 4.6 | Steady-state treadmilling and chirality of FtsZ vortices | 30 |
| 4.7 | Residence times of single membrane-targeted FtsZ molecules at the bilayer | 31 |
| 4.8 | Representative diagrams of the main findings of Section 4 | 35 |
| 5.1 | FtsZ-YFP-mts ring formation is impaired when membrane binding and lateral interactions are disrupted. | 38 |
| 5.2 | GTPase effect on treadmilling FtsZ rings | 40 |
| 5.3 | Membrane-binding affinity affects FtsZ treadmilling rings | 42 |
| 5.4 | FtsZ-YFP-mts-His ₆ variant affects treadmilling velocity of FtsZ rings | 43 |
| 5.5 | Factors that influence FtsZ treadmilling rings | 46 |
| 6.1 | FtsZ-YFP-mts synthesis in batch | 49 |
| 6.2 | Purified FtsZ-YFP-mts inside vesicles | 50 |
| 6.3 | Synthesized FtsZ-YFP-mts inside vesicles | 51 |
| 6.4 | Vesicle trapping to allow buffer exchange | 52 |
| 6.5 | Deformation of giant vesicles | 53 |
| 6.6 | Schematic representation of Z-ring reconstitution inside cell-like environments | 55 |
| 7.1 | Microfluidics set-up with default parameters | 58 |
| 7.2 | Effect on titration by different parameters on the pressure pump script | 60 |

LIST OF FIGURES

| | | |
|-----|--|----|
| 7.3 | Effect of Mg^{2+} titration of FtsZ polymerization in the presence of 100 mg/ml Ficoll | 62 |
| 7.4 | Effect of Ficoll titration on FtsZ polymerization in the presence of Mg^{2+} | 63 |
| 7.5 | Effect of Mg^{2+} and Ficoll titration of FtsZ polymerization | 64 |
| 7.6 | Effect of titration of Mg^{2+} in a cell-free expression reaction | 65 |
| 7.7 | Effect of titration of plasmid in a cell-free expression reaction for FtsZ | 66 |
| A.1 | FtsZ-YFP-mts sedimentation velocity analysis. | 78 |
| A.2 | GTPase activity of different FtsZ proteins | 79 |
| A.3 | Cumulative probability plots of single-molecule experiments | 80 |
| B.1 | Ring formation of different FtsZ mutants | 89 |
| B.2 | Example of a characteristic QCM data | 90 |
| B.3 | GTPase activity for the different variants | 91 |
| C.1 | FtsZ-YFP-mts on EggPG:DOPC, 80:20 mol % | 93 |
| D.1 | Effect of Mg^{2+} titration of FtsZ polymerization | 94 |
| D.2 | In the presence of Ficoll, FtsZ filaments tend to dissociate | 95 |

List of Tables

| | | |
|-----|--|----|
| 3.1 | Primers used to generate FtsZ-YFP-mts mutants and variants. | 16 |
| 3.2 | List of components for a in-house produced cell-free reaction. | 18 |
| B.1 | Sedimentation velocity analysis | 92 |

Chapter 1

Introduction

1.1 Cell division in bacteria

The bacterial cell cycle comprises three major processes: mass growth, chromosome replication and cell division; together they allow bacterial proliferation in a well-controlled manner, preserving cell integrity and its information material [Dewachter et al., 2018]. In each cell cycle, by partition, two progeny cells will derive from a mother cell with an intact and complete genome, assuring the survival of each of them. Such an event is called cytokinesis, and it provides the required force to split an *Escherichia coli* mother cell into two. Due to its tight spatial regulation, cytokinesis allows a precise distribution of the genetic material that is required by the daughter cells to propagate [Margolin, 2005]. An important player during cytokinesis is the bacterial membrane, it does not only play a role as a passive physical barrier, but it also represents a dynamic platform for the interaction between lipids, membrane binding proteins and general cytoskeletal elements [Loose and Schwille, 2009]. It is on the membrane where major events will take place, such as identification of the cell division site, correct localization of the cell division machinery and simultaneous constriction of the bacterial membrane and cell wall.

In *E. coli*, cell division is based on a ring-like contractile structure. The macromolecular machinery will transiently interact to form, close to the end of the cell cycle, a contractile ring at the mid cell position. The first component to assemble at the division site is FtsZ. FtsZ is a tubulin homologue well-conserved among different bacterial species, it will self-assemble in the presence of GTP due to its GTPase activity. The protein cannot bind to the membrane by itself, and it requires accessory proteins to interact with the membrane: FtsA and ZipA [Haeusser and Margolin, 2016]. Together these three proteins will form the so-called Z-ring (also called divisome) that will recruit further machinery for cytokinesis to take place. The divisome machinery has more than 20 known proteins, among the most important are: FtsZ, FtsA, ZipA, FtsK, FtsQ, FtsL, FtsB, FtsW, FtsI and FtsN [Rico et al., 2013]. The formation of the division machinery occurs in two sets: i) early and ii) late division proteins. The early division proteins set includes FtsZ along with FtsA and ZipA. The process starts with FtsZ polymerization on the inner membrane anchored by its

1.1 Cell division in bacteria

recruiter proteins. Through transient interactions, FtsZ associates with the amphitropic protein FtsA and the bitopic membrane protein ZipA. Mutants lacking either FtsA or ZipA can still divide, but absence of both impairs completely cell division (**Figure 1.1**) [Rico et al., 2013, Rivas et al., 2013].

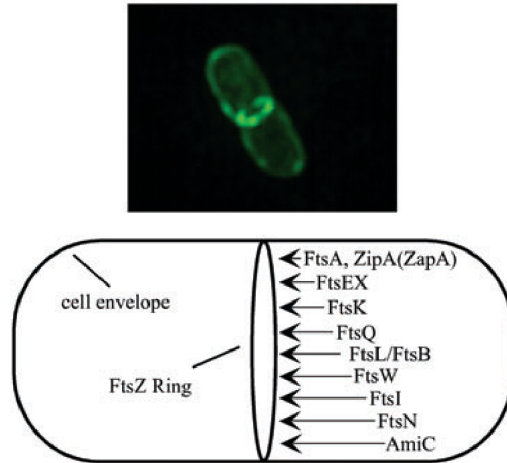


Figure 1.1: *E. coli* Z-ring. Upper panel, GFP-FtsL imaged by deconvolution microscopy. Bottom diagram illustrate the order of incorporation of division proteins into the division ring [Weiss, 2004].

Once the early set of proteins are in place, the late set of division proteins bind as follows: FtsE+FtsX, FtsK, FtsQ, FtsL+FtsB, FtsW, FtsI, FtsN and AmiC [Weiss, 2004, den Blaauwen et al., 2017]. Another important set of players are proteins involved in the septal wall synthesis. Septal wall formation requires the late proteins FtsI and FtsW, and also the transpeptidase-trans glycosylase PBP1b. However, it is FtsN, the final trigger of cytokinesis that will ultimately signal to split the cell in two [den Blaauwen et al., 2017].

Z-ring initiation is tightly controlled spatially and also temporally. Improper FtsZ assembly leads to aberrant cells, with different size and different genetic content. The main regulation for FtsZ positioning is protein concentration and there are two systems that control such: nucleoid occlusion and Min proteins oscillations (**Figure 1.2**) [Romberg and Levin, 2003].

Spatial regulation is provided by the nucleoid occlusion system that prevents FtsZ polymerization in the vicinity of the bacterial chromosome. Such negative regulation is provided by SlmA that specifically binds to *E. coli* chromosome and avoids cell constriction near to the chromosome [Lutkenhaus et al., 2012]. Spatiotemporal regulation is given by the oscillatory Min system that will localize FtsZ at the mid cell position. In this system, oscillations from pole to pole will recruit and let FtsZ polymerize only at the region with the lowest concentration of FtsZ inhibitor: MinC [Kretschmer and Schwillle, 2016]. Recently, two additional mechanisms for the correct positioning of FtsZ have been reported: 1) The Ter macrodomain. It is a replication terminus region in the *E. coli* chromosome that guides division and promotes assembly of the Z-ring close to it. An anchor, called Ter linkage

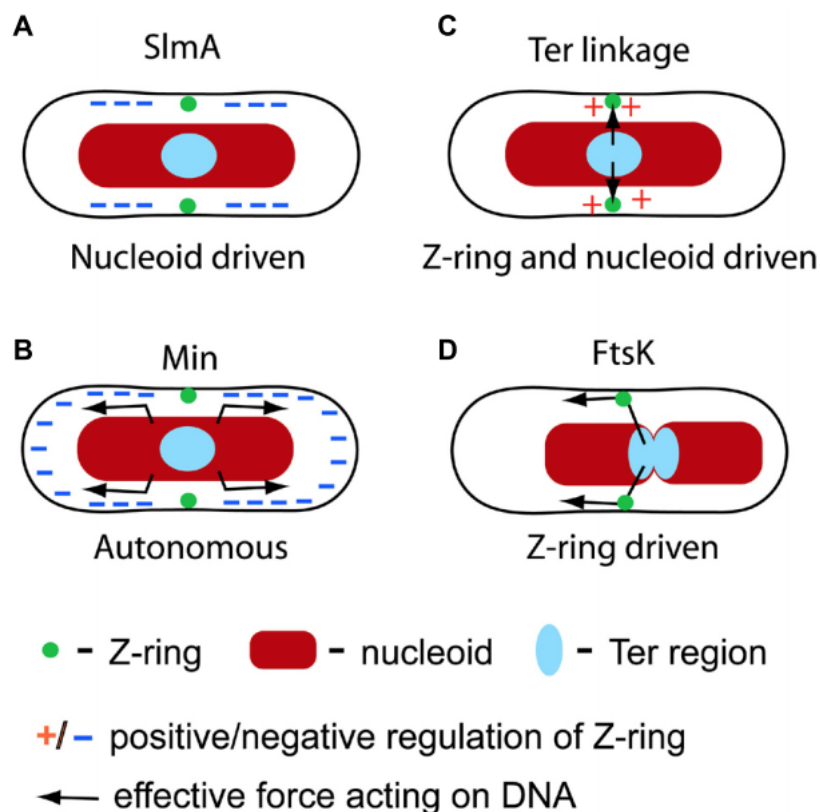


Figure 1.2: Main regulators that dictate the correct positioning of the FtsZ-ring [Maupin-Furlow et al., 2015]. A) Nucleoid occlusion SlmA-dependent. B) MinCDE system. C) Ter linkage. D) FtsK localization.

regulates the localization of the Z-ring and the Ter macrodomain. 2) FtsK is one protein that belongs to the late division proteins set. It leads the correct positioning of DNA and localizes the chromosome with respect to the Z-ring.

1.1.1.1 Z-ring disassembly and constriction generation in cytokinesis

After more than 25 years of study, there are still many missing details on the mechanistic side of the FtsZ-ring. For instance, disassembly process that takes place after division has happened is still not known in detail. Recently, it has been described that disassembly occurs in a coordinated set of events initiated by FtsZ. FtsZ will disassemble right before closure of the cell envelope. After fusion of the inner membrane in the daughter cells, ZipA and FtsA will disassemble, followed by the late set of division proteins. The last one to abandoned the cell division site is FtsN, once all the FtsN has been removed, the new cells separate and a new round of cell-cycle starts [Söderström et al., 2016, Söderström et al., 2014].

One important question that still remains to be answered is the origin of the constriction force during cytokinesis. It has been believed that FtsZ has a force-generating role during cell division. Here, the constant rearrangement of FtsZ filaments along the membrane can provide the necessary force to split a mother cell in two. In this scenario, FtsZ do not only acts as a scaffold but also as a force generator [Rico et al., 2013, Holden, 2018]. Another scenario proposes that FtsZ only acts as a spatiotemporal regulator of other cell division proteins such as the ones involve in septal wall synthesis. In this scenario, FtsZ will be the driving force that will initiate invagination of the bacterial membrane, and later Peptidoglycan (PG) synthesis will provide the final constriction force that will allow complete constriction of the inner membrane [Bisson-Filho et al., 2017, Holden, 2018, Monteiro et al., 2018].

1.1.2 The central component of bacterial cell division, FtsZ

The FtsZ protein is a 40 kDa self-assembling GTPase present in the cytoplasm. It has two globular subdomains that can independently fold. The N-terminal side possess a GTP-binding and hydrolysis site as well as residues for lateral interactions [Erickson et al., 2010]. The C-terminal side has three important regions: i) an unstructured C-terminal linker (CTL) that influences lateral interactions with a mechanism of electrostatic repulsion with a direct effect on monomers on and off rates, as well as fragmentation and annealing [Sundararajan et al., 2018] ii) C-terminal constant region (CTC) or C-terminal tail (CTT) and iii) C-terminal variable region (CTV), both responsible for interaction with other proteins from the division machinery (**Figure 1.5**) [Huang et al., 2013].

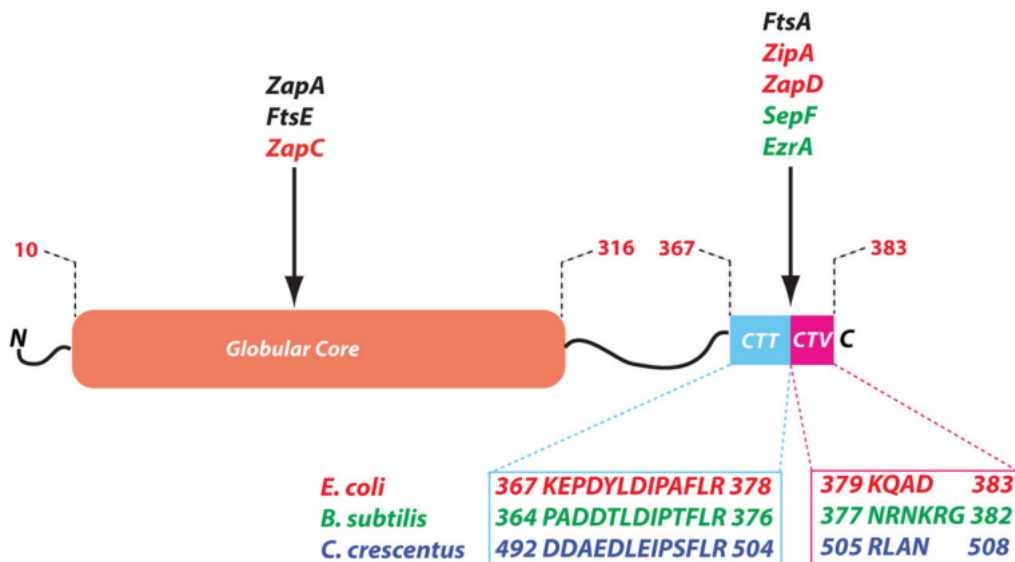


Figure 1.3: Schematic representation of FtsZ, the main protein domains and proteins that interact with each of them [Huang et al., 2013]

For membrane attachment, in *E. coli*, FtsZ requires two additional divisome proteins,

FtsA and ZipA. FtsA is an amphitropic protein that associates to the membrane by an ATP-linked process mediated by a short amphipathic helix [Pichoff and Lutkenhaus, 2005]. The bitopic membrane protein ZipA contains a short N-terminal intracellular region, a transmembrane region, and an extracellular C-terminal FtsZ-interacting domain connected by a flexible linker region [Ohashi et al., 2002].

As mentioned before, FtsZ can self-polymerize into long filaments, that together constitute the Z-ring. *In vitro* studies have shown that FtsZ monomer can bind magnesium with low affinity [Rico et al., 2013]. In the presence of GDP, FtsZ-GDP oligomerizes to form linear single-stranded oligomers in a Mg-dependent manner. In contrast, in the presence of GTP, FtsZ-GTP monomers will assemble to form narrow-size distributed single stranded filaments. The cooperative process do not only depend on GTP but also on Mg^{2+} , and it is stimulated by K^+ [Mingorance et al., 2010]. The cooperative behaviour has been demonstrated by the fact that there is always a proportion of unpolymerized FtsZ in polymer solution, this indicates that a critical concentration of polymerization exists ($\sim 1 \mu M$) [Erickson et al., 2010]. FtsZ polymers have a flexible structure that depending on the conditions, can further organise in high order polymers such as multi-stranded fibers, bundles, circles, toroids, etc [González et al., 2003, Erickson et al., 2010].

Super resolution data has shed light on the structural organization of the Z-ring *in vivo*, where the FtsZ ring appears to be an heterogeneous structure, with large nodes of high protein concentration with intercalated thinner regions of low protein concentration [Holden, 2018]. Lateral interactions seem to be paramount for FtsZ protofilaments organization going from a loose arrangement into a Z ring composed of dynamic points with short and overlapping protofilaments [Meier and Goley, 2014]. *In vitro*, lateral interactions have been seen to depend on factors like protein concentration, pH, divalent cations concentration and the effect of crowding agents [Erickson et al., 2010].

FtsZ polymers have a highly dynamic behaviour that is GTP dependent. Monomers assembly and disassembly are crucial for Z-ring formation and maintenance. Fluorescent recovery after photobleaching (FRAP) experiments have shown the dynamic exchange of FtsZ monomers and short oligomers with the *E. coli* cytokinetic ring, with a half-time of 8-30 s [Chen and Erickson, 2005]. The progressive movement of FtsZ polymers is compatible with a treadmilling mechanism, where individual molecules have been observed to remain in a particular point while one end of the polymer grows (polymerization) and the other shrinks (depolymerization) [Wagstaff et al., 2017]; with different polymerization and depolymerization rates in the so-called plus and minus ends [Wagstaff et al., 2017]. As a matter of fact, multiple studies have shown not only FtsZ treadmilling *in vitro* [Wagstaff et al., 2017, Ramirez-diaz et al., 2018], but also *in vivo* [Yang et al., 2017, Bisson-Filho et al., 2017], confirming a polymerization mechanism for FtsZ filaments.

1.1.3 Membrane tethered FtsZ

It has been mentioned that FtsZ does not bind to the membrane by itself, and it required natural anchors to interact with the lipidic interface of the membrane. To bypass the need of natural anchors in *in vitro* studies a membrane-tethered FtsZ chimera was

1.2 Biometric membranes for the study of Z-ring

generated. The synthetic protein has a YFP, FtsZ's central hub and the amphipathic helix of *E. coli* MinD (FtsZ-YFP-mts) [Osawa et al., 2008].

The membrane targeted sequence is a 15 - amino acids sequence [FIEEEKKGFLKRLFGG] with positive charges, the hydrophobic region promotes membrane binding, and in MinD, enhances the interaction of the protein with anionic phospholipids [Renner and Weibel, 2012]. Furthermore, the anionic sequence can be attached to either the C-terminal (FtsZ-YFP-mts) or the N-terminal (mts-FtsZ-YFP) side (**Figure 1.4**). Using synthetic membranes, it was revealed that the chimeric proteins were able to form static ring-like structures and induces deformation and tabulation of liposomes in the presence of GTP [Osawa et al., 2009, Osawa et al., 2008].

It is important to mention, that the chimera protein behaves in a similar fashion as the wild-type version. It has been shown that FtsZ-YFP-mts can assemble on supported lipid bilayers, the filaments are not static and have a fast exchange of subunits with a half-life time of 10 s [Arumugam et al., 2014], similar to the exchange rate *in vivo* [Anderson et al., 2004] and in solution [Chen and Erickson, 2005].

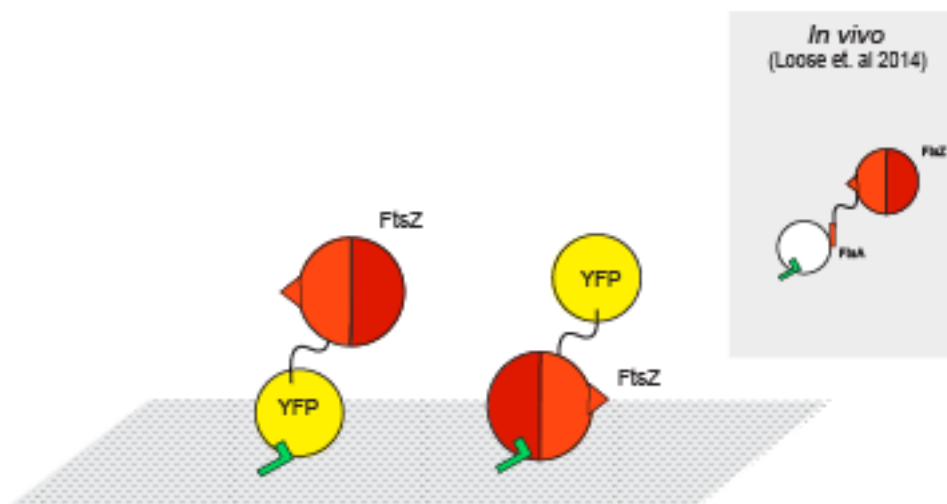


Figure 1.4: Schematic representation of membrane-targeted chimera proteins: FtsZ-YFP-mts (left) and mts-FtsZ-YFP. As comparison, the *in vivo* complex FtsZ-FtsA for membrane binding is illustrated.

1.2 Biometric membranes for the study of Z-ring

Membrane models represent an alternative for the study of minimal systems when compared with *in vivo* approaches. Such models are able to reproduce crucial cellular properties, allowing *in vivo* reconstitution of cellular modules at physiological levels. The main advantage relies on two important points: i) Model membranes are simpler than cellular environments with experimental conditions easy to manipulate and tinker (composition,

concentrations and geometry. ii) Membrane models are capable to preserve intrinsic parameters of biological membranes such as fluidity and mechanical properties. All together these make membrane models suitable systems to mimic biological membranes [Keller et al., 2013].

Given the complexity of biomembranes, there are different types of membrane models with different properties and characteristics, most of them preserving the bilayer structure of natural membranes. Membrane models are generally classified according to its shape and size, characteristics that dictate the method compatibility to biochemical and biophysical assays. They can be obtained either from purified or synthetic cellular components, namely bottom-up reconstitution; or directly from cells, top-down approach.

A widely used membrane model is a lipid bilayer deposited on a solid support [Loose and Schwille, 2009]. Supported lipid bilayers (SLB) are robust and easy to manipulate. Due to the fact that the planar structure is unable to impose spatial boundaries, one might be cautious of the type of behaviour obtained in this model membranes since supported bilayers might have a direct influence on some lipid properties such as fluidity. However, the addition of functional proteins on the supported bilayer lowers the rate of diffusion when compared with molecules in pure solution. Thus, this model is considered as the most suitable for the reconstitution of process that occur on the membrane [Loose and Schwille, 2009].

Small unilamellar vesicles (SUV) are a very frequent starting material for SLB production. Incubated on a hydrophilic surface (glass, mica or silica), SUV are forced to fuse on a glass coverslip aided by the use of Ca^{+2} or any other divalent cation. Vesicles of approximately 100 nm of diameter coalesce to form a homogenous bilayer on the top of the solid surface. Divalent cations not only reduce the repulsion between negatively charged lipids but also allows the formation of clusters composed of lipids with negative charge. Between the bilayer and the solid support, a thin layer of water promotes the preservation of important properties of biological membranes, such as the rate of diffusion and fluidity of the components. These properties that are particularly enhance on the top of the bilayer.

SLBs are suitable for characterizations using different techniques. Fluorescence Recovery After Photobleaching (FRAP) allows not only the characterization of lipids and proteins, but also their visualization. Techniques like Surface Plasmon Resonance (SPR) or Total Internal Reflection Fluorescence Microscopy (TIRFM) allow the quantification of protein-membrane interactions. Finally, given the planar structure of supported bilayers, mechanical techniques can also be employed such as Atomic Force Microscopy (AFM).

Going from a planar surface to a more cell-like conformation, with diameter sizes ranging from 10 to 100 μm . Giant unilamellar vesicles (GUV) are used for the encapsulation of components in their internal volume, controlling biophysical and biochemical properties in and outside the vesicles. In such models, it is possible to reproduce some physiological conditions, in particular ionic strength and crowding effects. In the literature there are many publications about successful encapsulation of cellular macromolecular complexes. For instance, in a report published by Pontani et al. 2009 [Pontani et al., 2009], actin polymerization was triggered inside giant vesicles. Pores in the vesicle membrane allowed the delivery of ATP and salts, elements required for polymerization to happen.

Several methods have been described for GUVs generation, relying on the use of different devices and physical properties. From the methods based on lipid hydration, the most effective way for GUVs obtainment is by electro formation. It requires a specific device with two electrodes tied to a chamber that is filled with the desired buffer. Methods based on water/oil emulsions are capable to enhance the total percentage of encapsulated macromolecules. A third class of method relies on the use of microfluidic systems. They can produce giant vesicles having approximately the same size with the best performance for macromolecules encapsulation. Although, control at the micrometre scale can be achieved, the only drawback is the used of sophisticated apparatus, small vesicle size ($50 \mu\text{m}$) and oil traces [Williams, 2013, Encinar et al., 2013, Pautot et al., 2003].

1.2.1 Z-ring reconstitution on biomimetic membranes

One of the pioneers works of Z-ring reconstitution on biomimetic membranes was done using the membrane-tethered FtsZ protein. FtsZ was observed to form static-ring like structures inside tubular liposomes, in particular it accumulated in narrow regions of $1 \mu\text{m}$ diameter. Filaments were formed in the presence of GTP, however GTP hydrolysis was not required for vesicle deformation [Osawa et al., 2008]. When the protein was added in the buffer surrounding the vesicles, the protein was capable to form outwards deformations on the membrane. On the other hand, inward deformations was generated when a chimera protein with a mts in the N-terminal was employed [Osawa et al., 2009] (**Figure 1.5**).

Using a more *in vivo* scenario, FtsZ has been reconstituted along with ZipA and also with FtsA. Two-dimensional networks have been observed on supported lipid bilayers when FtsZ and a soluble variant of ZipA are employed [Mateos-Gil et al., 2012b]. When both proteins are encapsulated in vesicles their interaction leads to dynamic structures that generate vesicle shrinkage [Cabré et al., 2013]. In a different scenario, when FtsZ and FtsA are reconstituted together on a lipid bilayer, dynamic rotating rings are observed [Loose and Mitchison, 2014].

1.3 Techniques to generate cell-like environments

1.3.1 Cell-free protein synthesis

Cell-free expression reactions contain all the required components for energy production and protein synthesis **Figure 1.6**. The biggest advantage of this technology, when compared to *in vivo* protein production, is that the whole machinery and energetic resources are focused on the production of one or a couple of proteins of interest, leaving behind the necessity to preserve cell viability and growth. The absence of cell wall permits the active monitoring and manipulation of the protein under expression. Also, genetic information can be directly provided in the form of linear or plasmidic DNA, as a consequence, there is no need to worry about time consuming cloning steps (Carlson et al. 2012).

Like with any technology, a couple of drawbacks exist. In general, reactions are typically

1.3 Techniques to generate cell-like environments



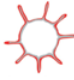




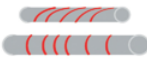
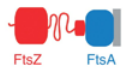

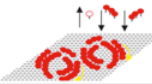




| Membrane targeting method | Membrane system | Outcome | Model |
|---|---|--|---|
|  | Protein inside tubulated vesicles | Z-ring formation and constriction |  |
| | Protein outside spherical vesicles | Concave depressions, membrane tubulation |  |
| | Protein on lipid bilayers assembled on curved substrate | Alignment of FtsZ filaments with preferred curvature |  |
|  | Protein outside spherical vesicles | Convex bulges |  |
| | Protein outside tubulated vesicles | "Inside-out" Z-ring formation and constriction |  |
| | Protein on lipid bilayers-coated glass capillaries of different diameters | Alignment of FtsZ filaments with preferred curvature |  |
|  | Protein inside giant unilamellar inner membrane vesicles | Luminal accumulation of FtsZ-FtsA bundles |  |
| | Protein on supported lipid bilayers | FtsA and FtsZ self-organize into dynamic patterns |  |
|  | Protein inside giant unilamellar vesicles | FtsZ and ZipA induce vesicle shrinkage and cell membrane invagination |  |
| | Protein outside giant unilamellar vesicles | Membrane tubulation of vesicles containing ZipA driven by native FtsZ polymers |  |
| | Protein on supported lipid bilayers | ZipA-FtsZ dynamic networks |  |

Figure 1.5: Schematic representation of FtsZ reconstitution on biomimetic membranes. Wild-type systems: FtsZ-FtsA and FtsZ-ZipA systems are depicted; both membrane-targeted version of FtsZ are also shown.

short, with limited amount of resources for energy supply and substrate availability. As time goes by, accumulation of toxic bioproducts can hinder protein synthesis and even protein functionality. As a consequence, low protein production, or non-functional protein products are obtained. In the literature, there are several methods reported to improve protein production. In recent years, cell free-protein systems have caught the attention of synthetic biologist interested in the generation of minimal cells by a bottom-up approach [Jia et al., 2017]. Recently, a lot of work has been put in optimization, for instance, the use of flow or passive dilution removes the presence of inhibitory products. What is

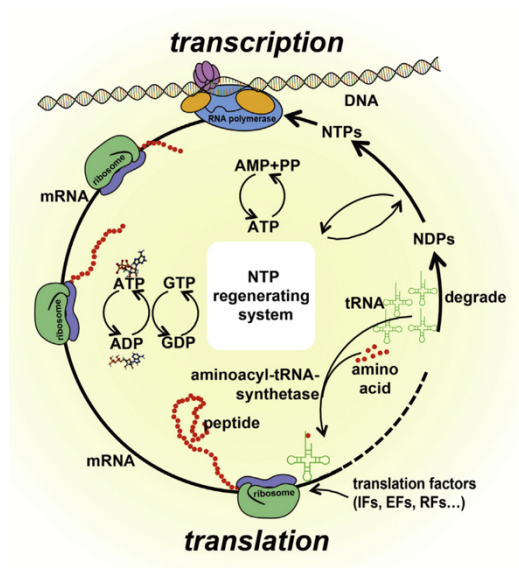


Figure 1.6: Schematic representation of the main components generally present in a cell-free expression reaction. The system contains all the main components for transcription and translation to happen upon DNA addition.

more, it is possible to reduce the monetary cost of the reaction by implementing energy production through ATP regeneration systems like glucose-6-phosphate or fructose-1,6-biphosphate, making this system available for a broader market. Translation components have also been improved by the use of purified pre-charged aminoacyl-tRNAs, translation factors or aminoacyl-tRNA synthetases [Zemella et al., 2015]. For cell lysate production, any organism can be employed. One of the most commonly used is *E. coli* because the preparation is simple and inexpensive, it can generate high protein yields, with a high rate of production. The biggest disadvantage of this system is the limited post-translational modifications, particularly important when eukaryotic proteins want to be expressed. As a consequence of years of study and improvement Cell-free expression reactions, a better understanding of the components and reactions involved have been provided [Carlson et al., 2012].

One of the better described and also characterized systems is the Protein synthesis using recombinant elements (PURE) system [Shimizu and Ueda, 2010]. The system contains translation and ribosome-recycling factors, 20 aminoacyl-tRNA synthetases, methionyl-rRNA transformylase, T7 RNA polymerase and ribosomes. If the aim is to use cell-free protein synthesis as a base for a minimal cell, the system must be capable to replicate one of the most important machinery for protein production, the ribosome. In *E. coli*, the ribosome contains 54 proteins: 33 50S and 21 30S [Forster and Church, 2006]. As a first step towards the reconstitution of a minimal cell from a bottom-up approach, the PURE system has been capable to synthesise 30 out of 35 50S and all the 30S proteins [Li et al., 2017].

1.3.2 Microfluidics

Microfluidics represents a promising technology for the automation of tedious experimental work. General considerations for the generation of devices are the materials and fluids used. Poly-(dimethyl)-siloxane (PDMS) is an inexpensive and commonly used material, which is easy to deform and manipulate. When the use of strong solvents is required, PDMS is no longer suitable since it undergoes swelling and deformation. Different materials can be employed as a substitute, such as glass or silicon. Fluid viscosity can determine droplet size, also the type of surfactants, and hydrophilicity or hydrophobicity of the channel.

Droplet-based microfluidics permits the encapsulation of reagents in a defined microvolume, mimicking one of the key features of life: compartmentalization [Vyawahare et al., 2010]. By definition, droplet-based microfluidics deals with the generation of highly monodisperse droplets and their manipulation. Manipulation can be performed independently on each droplet, allowing the generation of isolated microreactors that are easier to analyse, transport and mix.

Droplet formation relies on two different methods with specific geometries: T-junction and flow-focusing. The first one has an inlet channel with a disperse phase that perpendicularly intersects the continuous phase. In the second geometry, disperse and continuous phases are flowed through a narrow channel. Improvements in the microdevice design have allowed the integration of electrical control in droplet formation with the use of electrodes.

Once generated, droplets can be manipulated. There is a broad catalogue of designs for droplet fission, fusion and mixing. The number of applications in biology is broad, from protein expression to the synthesis of organic compounds, with high reproducibility and performance. Droplets can be seen as microreactors where reactions are carried out in microscale volumes, using only small volumes of precious reagents. It also reduces the generation of waste and the parallelization of reactions [Teh et al., 2008, Theberge et al., 2010]. Recent technology allows the injections of volumes in the picolitre volume, microchannels can be integrated with a small electric field that will destabilize the monolayer surface of the droplet, facilitating the delivery of aqueous solution inside the droplet [Abate et al., 2010].

Microfluidics systems do not only provide a way to generate cell-like containers in a high-throughput fashion. The technology is also useful for downstream analysis, for instance it provides a suitable platform for imaging and manipulation with devices capable to immobilize droplets or even vesicles using small poles and hydrodynamic forces [Robinson et al., 2014].

1.3.3 Contained cell-free expression reactions

Some examples among the literature have showed successful implementation of *in vitro* protein expression inside droplets, most of the articles reporting the use of emulsion droplets. For instance, in Maeda et al. 2012 [Maeda et al., 2012], they reconstituted two key elements of the bacterial cytoskeleton: MreB and MreC, encapsulating a cell-free

expression reaction inside liposomes. They observed that MreB filaments were only visible when both proteins were expressed and only in vesicles with a diameter smaller than $15 \mu\text{m}$. Recently, proteins from the cell division machinery of *E. coli* were reconstituted inside vesicles and some deformation were reported when either FtsZ-FtsA or FtsZ-ZipA were co-expressed. These works represent a milestone in the field of cell-free synthetic biology since the authors showed how valuable the implementation of cell-free expression reactions for the study of particular cell modules can be. One example that reported that a lab-on-chip approach could generate better reproducible and high-throughput performance is the work of Dittrich et al. 2005 [Dittrich et al., 2005]. Here, the authors implemented a microfluidics chip for the generation of water-in-oil emulsions capable to contain and support an in-vitro expression reaction. The final outcome was the successful expression of a fluorescent protein in the intraluminal space of highly monodisperse biocontainers. Microfluidics can also be used to study the parameter space of a reaction, using a DNA-processing biochemical reaction Genot et al. 2016 showed the implementation of a droplet-based microfluidics technology to quickly characterise a set of reactions in a high-throughput manner [Genot et al., 2016].

Chapter 2

Objectives

The general aim of the present doctoral thesis has been to characterise the self-organisation behaviour of FtsZ when reconstituted in supported membranes and 3D compartments. We aimed to elucidate the principles that lead to the Z-ring formation. The overall project has been organized into four sub-projects covering complementary and interconnected aspects of the main objective.

1. **Self-organization of membrane-tethered FtsZ in flat supported membranes** (Section 4) to understand the mechanisms governing the emergence and steady-state dynamics of FtsZ chiral vortices in supported bilayers, as a minimal membrane system. The specific aims of this sub-project have been: 1) the biochemical characterization of a membrane tethered FtsZ variant (FtsZ-YFP-mts) in solution and in membrane systems; and 2) the analysis of FtsZ-YFP-mts self-organization in bilayers, to elucidate whether FtsZ by itself is able to self-organize into dynamic vortices and if this is the case, determine of the biochemical factors that control their emergence.
2. **In depth characterization of FtsZ treadmilling vortices** (Section 5) to understand how various factors e.g. membrane binding, lateral interactions, GTPase activity and membrane binding, play a role in the dynamic properties of the FtsZ rings on supported bilayers. The specific aims have been: 1) the generation of multiple mutants by site-directed mutagenesis, insertions and deletions in different domains in the chimera protein; and 2) the characterization of each mutant variant and its ability to form dynamic FtsZ-rings on supported bilayers.
3. **Self-organization of membrane-tethered FtsZ inside cell-like environments** (Section 6) implementation of 3D biomimetic environments to further study the effects on ring formation. The particular aims of this sub-project were: 1) to primarily synthesize FtsZ-YFP-mts inside vesicles by means of a cell-free expression reaction and compare with purified FtsZ-YFP-mts; and 2) to generate a deformation system by means of microfluidics to go from a spherical vesicle to a rod-shape vesicle.
4. **Implementation of a massive titration approach for the generation of biochemical reactions** (Section 7) as a tool for the rapid characterization of biochem-

ical systems. The aims of this sub-project were: 1) implementation in our lab of a published microfluidics system from hardware to software; 2) trouble-shooting of the best conditions to generate a linear titration between two inlets, suitable for 1D or 2D titrations, 3) proof of concept using a) purified FtsZ over different concentration ranges of Mg^{2+} , crowding agent and both, b) cell-free expression system titration over Mg^{2+} .

Chapter 3

Materials and Methods

Materials: Reagents, salts and buffer components were purchased from Sigma, Merck or Invitrogen. All reagents were of analytical or spectroscopic grade. *E. coli* polar lipid extract, DOPC, DOPG and EggPC were acquired from Avanti Polar Lipids (Alabama, USA). Bradford and BCA colorimetric protein quantitation assays were from Bio-Rad (California, USA) and Pierce (Illinois, USA), respectively. Ultraviolet-curable glue was from Norland Optical Adhesive 63, (Norland Products, Cranbury, NJ). 5 ml HiTrap Q HP column, 5 ml HisTap FF column and 5ml HiTrap Desalting column were purchased from GE Healthcare. GTP was purchased from Sigma-Aldrich. Nano-body GFP-Booster Atto647N was from ChromoTek, (Germany). BIOMOL GREEN reagent for phosphate detection was from Enzo, Life Science. PUREXpress In Vitro Protein Synthesis Kits was purchased from New England BioLabs, Inc (NEB). FluoroTectm Green_{Lys} *in vitro* Translation Labelling System was purchased from Promega. CYTOP was acquired from Asahi glass (CTL-809M). PDMS base SylgardTM 184 and curing agent were from Dow Corning GmbH, Germany. Dextran CascadeBlue and Alexa Fluor 647 (10,000 MW, anionic fixable) were purchased from Thermo Fisher (cat. no. D1976 and D22914, respectively). Pico-Surf (TM) was purchased from Dolomite. PEEK Tubing Natural 1/16-inch outer diameter x 0.010-inch inner diameter x 50 feet was purchased from IDEX (cat. no. 1531 BL). Biopsy punch was acquired from Miltex Biopsy Punch with plunger, diameter 1.5 mm (cat. no. 33-31A-P/25). Microfluidic pressure controller and its Maesflow software (cat. no. MFCS-EZ; four channels for 1D or 2D titration, 0–1,000 mbar), its Fluiwell reservoir holder and pneumatic tubes were purchased from Fluigent.

DNA and Cloning: Plasmids corresponding to FtsZ-YFP-*mts* and *mts*-H-FtsZ-YFP were kindly provided by Dr. Harold P. Erickson (Durham, US). FtsZ-YFP-*mts* variants were constructed through site-directed mutagenesis or whole sequence replacement using the oligonucleotides specified in Table 3.1. Briefly, each gene was first amplified using the forward (FW) and reverse (RV) oligonucleotides in different PCR reactions, testing three different temperatures: 54°C, 58.5°C and 65°C. In a second PCR reaction, the PCR products from the FW and RV oligonucleotides were mixed; also three different temperatures were tested, 54°C, 58.5°C and 65°C. After DpnI digestion, vector constructs were

| Primer name | Sequence (5'-3') |
|-----------------------------------|---|
| FtsZ-YFP-mts* [L629E]_FW | atcctccgaactcgcgtttgagg |
| FtsZ-YFP-mts* [L629E]_RV | cctcaaacgcgagttcggaggat |
| FtsZ* [Δ -CTL]-YFP-mts_FW | acctgtcgcaacaacggtta |
| FtsZ* [Δ -CTL]-YFP-mts_FW | taaggatccggctgctaacaag |
| FtsZ* [D299A]-YFP-mts_FW | tcatatccggggcaagagaagtac |
| FtsZ* [D299A]-YFP-mts_RV | gtacttctcttgccccggatatga |
| FtsZ* [D212G]-YFP-mts_FW | acggtgcgtacgcctgcaaagtcca |
| FtsZ* [D212G]-YFP-mts_RV | tggactttgcaggcgtacgcaccgt |
| FtsZ* [T108A]-YFP-mts_FW | ggtggtggtgccggtacaggt |
| FtsZ* [T108A]-YFP-mts_RV | acctgtaccggcaccaccacc |
| FtsZ-YFP-mtsFtsA_FW | attgagtcgcttgatccacgagccgcccgccttgta |
| FtsZ-YFP-mtsFtsA_RV | agttggctgcgaaaagagttttaaggatccggctgctaacaag |

Table 3.1: Primers used to generate FtsZ-YFP-mts mutants and variants.

transformed into competent *E. coli* CH3-Blue cells and cultured in LB medium containing 50 g/ml ampicillin (37°C, overnight). DNA purification was performed according to the manufacturer's instructions (NucleoBond Xtra Midi, Macherey-Nagel, Düren, Germany). Successful plasmid construction was confirmed through next-generation sequencing (Eurofins, Brussel, Luxembourg).

PCoofy plasmid containing a sGFP protein was cloned using seamless cloning.

Protein purification: All proteins were purified as previously described [Osawa et al., 2008]. Briefly, the proteins of interest were cloned into pET-11b expression vectors. Expression vectors were transformed into *E. coli* BL21 DE3 and grow at 37°C overnight in the presence of ampicillin. For protein over-expression, LB medium was inoculated and cells were grown to an OD of 0.8 until protein synthesis was induced through 0.5 mM IPTG. Then, cells were incubated at 20°C (FtsZ-YFP-mts and FtsZ* ^[T108A]-YFP-mts) or 37°C (mts-H-FtsZ-YFP) overnight. Cells were sonicated and centrifugation at 3200 rpm (4°C). Subsequently, proteins of interest were precipitated from the supernatant through 30% ammonium sulphate and a 20 min incubation on ice (slow shaking). After centrifugation (3200 rpm, 4°C) and re-suspension of the pellet, proteins were purified by anion exchange chromatography using a 5 x 5 ml Hi-Trap Q-Sepharose column (GE Healthcare, Chicago, USA). The purity of the proteins was confirmed by SDS-PAGE and mass spectrometry.

GTPase activity: FtsZ GTPase activity was determined using the BIOMOL GREEN reagent for phosphate detection (Enzo). In brief FtsZ at 5 μ M concentration is measured every 20 seconds after adding 1 mM GTP for a total of 7 time points. After 15 minutes of incubation with BIOMOL GREEN, the samples are measured at OD 620. The data is later fit to a standard curve of 40 μ M phosphate.

Small unilamellar vesicles (SUVs) for supported lipid bilayers (SLBs) on glass and on quartz crystal sensors: Either DOPC:DOPC, 70:30 mol% (quartz) or *E. coli* polar lipid extract (glass; Avanti, AL, USA), initially dissolved in chloroform, were dehumidified under a gas nitrogen stream. Chloroform traces were further removed through desiccation (1 h). Subsequently, the lipid film was hydrated with SLB-buffer (50 mM Tris-HCl, 150 mM KCl, pH 7.5) to a final lipid concentration of 4 mg/ml. Then, multilamellar *E. coli* polar lipid extract vesicles were sonicated (10 min) to obtain SUVs. In contrast, a freeze-thaw protocol (8 cycles) with successive extrusion (37 x, 50 nm Whatman membrane) was used to obtain DOPC:DOPG SUVs [Cho et al., 2010].

Supported lipid bilayers (SLBs): #1.5 glass coverslips (Menzel, Germany) were cleaned in air plasma for 10 min at 60 W (0.3 mbar). Then a plastic chamber was attached to the cleaned coverslip using an ultraviolet-curable glue (NOA 63, Norland Products Inc., USA). The SUV stock was diluted in SLB buffer (50 mM Tris-HCl at pH 7.5, 150 mM KCl) to 0.5 mg/ml and 50 or 75 μ l were added to the reaction chamber depending the purpose (50 μ l for synthesized FtsZ-YFP-mts or 75 for self-organization assay with purified FtsZ-YFP-mts of giant unilamellar vesicles imaging.) CaCl_2 was further added to a final concentration of 3 mM to promote vesicle fusion and the formation of a lipid bilayer on the glass surface. The chambers were then incubated at 37°C for 20 min and subsequently washed with pre-warmed SLB buffer to remove non-fused vesicles. Finally, SLBs were washed with reaction buffer depending on the case: 50 mM Tris-HCl at pH 7.5, 150 mM KCl and MgCl_2 (5 mM or 1 mM) for self-organization assays or 150 mM KCl, 50 mM Tris-HCl at pH 7.5 and 550 mM Sucrose for vesicles experiments.

Giant unilamellar vesicles (GUVs) for protein and cell-free reaction encapsulation. Vesicles were prepared using the water-in-oil (w/o) emulsion transfer method [Pontani et al., 2009]. The encapsulation of purified FtsZ-YFP-mts was performed either with PURExpress reaction as inner buffer or with a 125 mM KCl, 25 mM Tris-HCl and 6.25 mM Mg^{2+} (use also as outer buffer in this case). When PURExpress was used as an inner buffer, an outer buffer with 150 mM KCl, 50 mM Tris-HCl at pH 7.5 and 550 mM Sucrose was used (\approx 949 mOsm). The phospholipid solution was prepared by dissolving EggPG:DOPC, 80:20 mol % in mineral oil. 15 μ l of PURExpress reaction (supplemented with a final concentration of 85 ng/ μ l) or 15 μ l inner buffer (150 mM KCl, 50 mM Tris-HCl at pH 7.5 and 550 mM Sucrose) and 1 μ M purified protein (supplemented with 15% optiprep to allow vesicle sedimentation) were added into a 500 μ l of phospholipid solution, and vortexed to generate an emulsion. The liposomes were formed into the same buffers to match the osmolality of the inner solution by centrifugation. Liposomes were harvested and imaged on an SLB, right away or after 2 hours of incubation at 37°C.

Self-organization assays: Either 0.5 μ M or 0.2 μ M FtsZ-YFP-mts (purified or *de novo* expressed) or FtsZ-YFP-mts-mutants were added to the SLB coated reaction chamber (200 μ l reaction volume). Polymerization was induced at 4 mM of GTP concentration.

| | Stock conc. | Final conc. | unit |
|---------------------|--------------------|--------------------|-------------------------|
| 3.2 x EM | 3.2 | 1 | fold |
| Amino acid mix | 25 | 2 | mM |
| T7RNAP | 700 | 10 | $\mu\text{g}/\text{ml}$ |
| Plasmid template | 500 | 15 | $\text{ng}/\mu\text{l}$ |
| E. coli S30 extract | 100 | 40 | % |
| DTT | 1000 | 1 | mM |
| CK | 20000 | 250 | $\mu\text{g}/\text{ml}$ |
| H ₂ O | | | |

Table 3.2: List of components for a in-house produced cell-free reaction.

Cell-free expression reaction: PURExpress reaction was prepared as indicated by the supplier. Briefly, reaction B was added to reaction A, later, a final volume of 7.5 μl of plasmid at a concentration of 170 $\text{ng}/\mu\text{l}$ was added. In batch experiments, the reaction was supplemented with 1 μl of FluoroTectm Green_{Lys} for protein labelling. For the barcoding droplets experiment an in-house cell-free reaction was used, a detail list of the components used is depicted in Table 3.2 .

QCM-D Measurements: Quartz crystal sensors (Biolin Scientific, Gotheburg, Sweden) were pre-treated with piranha-solution ($\text{H}_2\text{SO}_4:\text{H}_2\text{O}_2$, 3:1; 1 h), thoroughly cleaned with ddH₂O and dried under a nitrogen stream. Subsequently, sensors were immediately mounted in the flow cells of the QSense Analyzer (Biolin Scientific, Gothenburg, Sweden) and the crystals resonance frequencies were obtained in air and reaction buffer (QSoft Version 2.5.36; Biolin Scientific, Gothenburg, Sweden). After the stabilization of the resonance frequency in response to the deposition of ions on the measurement surface (flow rate: 0.15 ml/min), 1 mg/mL SUVs (DOPC:DOPG, 70:30 mol %) with 5 mM CaCl_2 were introduced to the crystal. Successful SLB formation was verified through a characteristic frequency change (Δf) of 25 ± 1 Hz [Cho et al., 2010]. Succeeding the formation of a stable signal base line, the flow rate was reduced to 0.1 ml/min and protein solutions ranging between 0.1 to 5 μM , with either 4 mM GTP or GDP, were successively adsorbed to the SLB and desorbed under constant flow (0.1 ml/min). Raw data export was performed using QTools 3 Version 3.1.25.604 (Biolin Scientific, Gothenburg, Sweden) and the extraction of the maximum frequency changes, in relation to protein concentration, was performed with R. All measurements were performed under constant temperature (24°C). If not indicated otherwise, all in the following used data depict frequency changes of the 9th overtone.

Microfluidics device preparation: For this study, we prepared PDMS microfluidics devices as previously elsewhere [Robinson et al., 2013, Baccouche et al., 2017]. Briefly, resist micro-patterns were produced on silicon wafers using a new photolithography instrument (μPG 101, Heidelberg Instruments) using a modified and adapted CAD-designs [Robinson et al., 2013, Baccouche et al., 2017]. PDMS was mixed with the curing agent at a ratio

(monomer to cross-linker) of 10:1 and degassed. The PDMS mixture was then poured on top of the wafer. After curing the PDMS at 80°C overnight, the device was peeled off. Inlets and outlets were punched with a biopsy punch of different diameters depending on the outer tubing diameter (0.5 mm to 1.5 mm). PDMS and glass bonding was done in a plasma oxygen chamber at 50% power, 0.3 mbar pressure during 15 seconds. The PDMS chip was further bake at 80°C overnight. Later, the devices were treated with -casein (1st generation) or pluronic (2nd generation) for trap experiments or CYTOP (CTL-809 M with CT-Solv 180 1:100) for droplet barcoding experiments. When casein/pluronic was used, the devices were centrifuged at 800 rpm for 10 min at room-temperature. Devices treated with CYTOP were incubated for 30 min at 180°C to evaporate the excess of CYTOP and avoid channels clogging.

Microfluidic traps set-up: Devices were loaded with approximately 250 μl volume of vesicles solution in the inlet reservoir. An syringe filled with 50 μl of 20% ethanol was connected to the outlet of the device, avoiding any air in between. Vesicle solution was sucked inside the device at a flow rate of approximately 5 $\mu\text{l}/\text{h}$. After approximately 30 min, vesicles were trapped. Deformation happens between 5 $\mu\text{l}/\text{h}$ - 50 $\mu\text{l}/\text{h}$. If required, buffer exchange was performed by removing and adding the new buffer solution into the inner reservoir.

Microfluidic generation of droplets and sample preparation for imaging: Droplets with a radii of $\approx 30 \mu\text{m}$ were generated by mixing aqueous channels with either a self-organisation FtsZ reaction or a cell-free expression reaction with an oil channel that contained Pico-Surf surfactant. Briefly, aqueous solution was prepared as follows: 1) Cell-free reaction reaction: 200 μl volume of reaction were supplemented with 0.5% vol of Dextran Cascade-Blue (dye 1) and 0.5% of Alexa Fluor 647 (dye2) (resuspended in $1 \times \text{TE}$ to achieve a stock concentration of 20 μM), solution was then divided in eppendorf two tubes (1.5 ml) and in each dye 1 or dye 2 was added at a 0.75% vol; 2) self-organisation FtsZ reaction, a total volume of 200 μl in 125 mM KCl and 25 mM Tris-HCl buffer was prepared with a final protein concentration of 1.5 μM and 1.4 mM GTP. Channels were pressurized by a controller MFCS-EZ from Fluigent. We harvested approximately 200 μl of emulsion each time, the reaction was then loaded into thin capillaries #1 and later fixed on a cover-slide. The capillary extremes were sealed with two-component glue.

Confocal microscopy: For all giant unilamellar vesicles experiments (on SLBs or in traps) as well as all the droplet experiments, image acquisition was performed on a Zeiss (Jena, Germany) LSM780 confocal laser scanning microscope equipped with a Zeiss Plan-Apochromat 40X/NA 1.2 W corr and Plan- Apochromat 20X/NA 0.8 objectives.

Total internal reflection fluorescence microscopy (TIRFM): All experiments on supported lipid bilayers were performed on a WF1 GE DeltaVision Elite total internal reflection fluorescence microscope (GE Healthcare Life Sciences, Germany) equipped with an OLYMPUS 100x TIRF objective (NA 1.49; Olympus K.K., Tokyo, Japan) and the

DeltaVision Elite system (GE Healthcare, Chicago, USA). Images were acquired with a PCO sCMOS 5.5 camera (PCO AG, Kelheim, Germany) controlled by the softWoRx® Software (GE Healthcare, Chicago, USA). All used FtsZ-YFP-mts variants were excited at 488 nm (diode laser: 10 mW, before objective). A standard FITC filter set was used for fluorescence imaging. For time-lapse experiments, images were acquired every 3 or 10 s, with a 0.05 s exposure time and shut light illumination between acquisitions.

Image analysis and processing of self-organization experiments on SLBs: Image analysis was carried out in MATLAB 2016 (MATLAB and Image Processing and Computer Vision Toolbox Release 2016a, The MathWorks, Inc., Natick, Massachusetts, United States.) and processing with Fiji/ImageJ (Rasband, W. S., ImageJ, US National Institutes of Health, Bethesda, <http://rsb.info.nih.gov/ij/>, 1997–2007). Images correspond to average of 5-10 frames from a time-series experiment. For the kymograph analysis, time-series acquisitions were filtered using a standard mean filter and were drift corrected (Image J). A Matlab script allows the user to define a ring by providing two coordinates. Every ring is automatically fitted to a circle with radius r . Then, three trajectories corresponding to three concentric circles having radii r , $r+1$ and $r-1$ pixels are determined. At this point, the script will read the time-series data and calculate a kymograph for each time point and trajectory.

The final kymograph corresponds to the average of the three different trajectories. To automatically calculate the slope, we first smooth the kymograph with a Savitzky-Golay filter of order 2 and enhance its contrast using a contrast-limited-adaptive-histogram-equalization (CLAHE) routine (Matlab). Next, using Fourier analysis, we find the characteristic frequency for the patterns on the kymograph. Finally, the slope corresponds the change in phase at this frequency. Quality criteria are properly chosen to reject low quality regions over the kymograph. To synchronize time lapse acquisitions, the initial frame (time 0) was defined when surface mean intensity was around 200 a.u.

Image analysis and processing of barcoding experiments: Image analysis was carried out in MATLAB 2016 (MATLAB and Image Processing and Computer Vision Toolbox Release 2016a, The MathWorks, Inc., Natick, Massachusetts, United States.) and processing with Fiji/ImageJ (Rasband, W. S., ImageJ, US National Institutes of Health, Bethesda, <http://rsb.info.nih.gov/ij/>, 1997–2007). Each image corresponds to average of 8 frames. Files from each channel (405 - Cascade blue, 488 - GFP/FtsZ-YFP-mts or 655 - Alexa 647) were collected as a stack file and analysed using the modified script provided by Baccouche et al. 2017 [Baccouche et al., 2017]. The main modification was done for FtsZ analysis, where the image was converted to edges to better identify the presence or absence of filaments.

Single-molecule imaging and residence time measurement: FtsZ-YFP-mts previously incubated 1:1 with the nano-body GFP-Booster Atto647N (ChromoTek, Germany) for at least 1 hour at 4°C under agitation. To filter out non-bound nano-body, we centrifuge our protein in a 30 kDa Amicon unit. The GFP-Booster Atto647N was excited

with a 640 nm diode laser (30 mW, before objective). Single molecule imaging was performed using a standard Cy5 filter set. After 10 minutes upon GTP addition, a significant number of spots in the single molecule channel (Atto647N) were observed and imaged at a rate of 1 fps or 3 fps with 0.3 s exposure time. To improve imaging conditions, we added 10 nM PCD, and 2 mM PCA as an oxygen scavenging system. To determine the position of every single molecule and calculate its residence time, we employed a Matlab routine designed by Weimann & Ganzinger [Weimann et al., 2013]. Briefly, a band pass filter was used to remove low and high frequency noise. Then, single molecule positions with intensity above a user-defined threshold were determined by their brightness-weighted centroid. The detection algorithm is highly efficient for detecting particles with a signal to noise ratio above 1.5. The user-defined threshold was chosen to detect the largest number of spots and kept constant for all experiments. Single molecules were tracked among consecutive frames in an area given by a radius of 10 pixels (pixel size = 0.042 μm). Thus, the residence time is defined as the time that the particle stays in this area before its signal vanishes.

To calculate the mean residence time, we calculated the probability as a function of time t to obtain a loss of signal event at times $\leq t$ (cumulative probability). We fitted to a double exponential function $Ae^{-kt} + Be^{-k_p t}$ where k refers to the inverse of the mean residence time and k_p corresponds to the photobleaching rate. A and B are constrained since the photobleaching contribution is limited to be between 0.2 - 0.25 in the fitting routine for all conditions (Matlab). The photobleaching rate was calculated as $k_p = 0.031\text{s}^{-1}$ using a single exponential fit.

Events shorter than 2 frames are below the accuracy of our method and were not included in the statistics. The cumulative probability was measured for 5 different experiments having total number of events (N) in each experiment. For GDP forms: 5 mM Mg^{2+} , N varies in the range of 3000 - 5300 events (1 fps) and 660 - 8800 events (3 fps). 1 mM Mg^{2+} , $N = 3000 - 11000$ (3 fps). For GTP forms: 0.04 mM GTP, $N = 1300 - 3000$ (1 fps). 4 mM GTP, $N = 1200 - 6700$. In the case of FtsZ*^[T108A]-YFP-mts at 4 mM GTP, $N = 180 - 800$.

Data processing: Data processing from section 4 and 7 was performed with Matlab 2016 and R 2016 was used for section 5 and 6.

Chapter 4

Treadmilling analysis reveals new insights into dynamic FtsZ ring architecture

FtsZ, the primary protein of the bacterial Z ring guiding cell division, has been recently shown to engage in intriguing treadmilling dynamics along the circumference of the division plane. When co-reconstituted *in vitro* with FtsA, one of its natural membrane anchors, on flat supported membranes, these proteins assemble into dynamic chiral vortices, compatible with treadmilling of curved polar filaments. Replacing FtsA by a membrane targeting sequence to FtsZ, we have discovered conditions for the formation of dynamic rings, showing that the phenomenon is intrinsic to FtsZ. Ring formation is only observed for a narrow range of protein concentrations at the bilayer which is highly modulated by free magnesium and depends upon GTP hydrolysis. Interestingly, the direction of rotation can be reversed by switching the membrane targeting sequence from the C-terminus to the N-terminus of the protein, implying that the filament attachment must have a perpendicular component to both, curvature and polarity. Remarkably, this chirality switch concurs with previously shown inward or outward membrane deformations by the respective FtsZ mutants. Our results lead us to suggest an intrinsic helicity of FtsZ filaments with more than one direction of curvature, supporting earlier hypotheses and experimental evidence.

This section corresponds to the published article:

Authors: Diego Ramirez^{*1,2}, Daniela A. García-Soriano^{*1,2}, Ana Raso^{*1,3}, Jonas Muücksch¹, Mario Feingold⁴, Germaán Rivas³ and Petra Schwiller^{#1}

¹Department of Cellular and Molecular Biophysics, Max Planck Institute for Biochemistry, Martinsried, Germany, ² Graduate School for Quantitative Biosciences (QBM), Ludwig-Maximilians-University, Munich, Germany, ³Centro de Investigaciones Biológicas, Consejo Superior de Investigaciones Científicas (CSIC), Madrid, Spain, ⁴Department of Physics, Ben Gurion University, Beer Sheva, Israel.

*Contributed equally

Journal: PLoS Biol. 2018,16(5): e2004845.

4.1 RESULTS

4.1.1 Membrane-targeted FtsZ self-organizes into dynamic rotating vortices

The protein chimera FtsZ-YFP-mts ($0.5 \mu\text{M}$) in its GDP-bound form (corresponding to a non-assembled state, according to sedimentation velocity **Figure A.1**, did not form visible structures on a supported lipid membrane, as revealed by TIRFM. We have found that FtsZ-YFP-mts under assembly-promoting conditions (4 mM GTP , 5 mM Mg^{2+}) formed filaments on supported lipid bilayers, which self-organize with time into dynamic ring-like structures. The assembly of the dynamic rings is a time-dependent phenomenon. After several minutes upon GTP addition, in which highly dynamic short filaments were observed to attach, detach and diffuse on the surface, longer curved filaments appeared to grow directionally (**Figure 4.1A, panel 5:00**). At this stage, intrinsic motion drives filament-filament interactions to create small and dim closed circular structures (**Figure 4.1A, panel 15:00**). These structures tend to be highly unstable: closed filaments were able to open, fuse with adjacent filaments or to close back. At later times, closed circular strands turned into thicker ring-like structures (**Figure 4.1A, panel 30:00**).

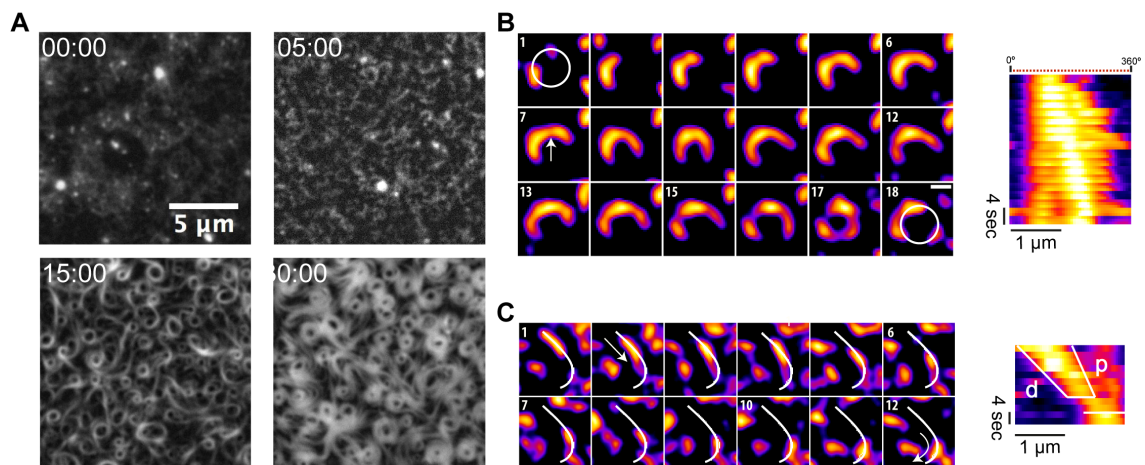


Figure 4.1: Nucleation and growth of FtsZ filaments into rings on supported lipid bilayers. (A) Representative snapshots from a time-lapse experiment displaying different stages of ring formation. Images were taken every 10 sec using TIRF illumination (YFP channel). Frames correspond to the times (min) indicated after the addition of GTP and Mg^{2+} . (B) Polar clockwise growth of a single FtsZ from a nucleation point. Growth seems to occur stepwise and depend on the accessibility of small filaments nearby (panel 1 and 2). Lower local protein density (white arrow) correlates with a higher flexibility of the polymer (panels 7-12). Breakage occurs primarily in trailing regions (15). After ca. 3 min, a primitive ring made of three distinct short filaments is exhibited (17). (C) Directional filament gliding via treadmilling. Fragmentation or depolymerization destabilizes the trailing (“older”) edge as shown in the kymograph (d-labeled white line). Images in (B) and (C) were taken every 2 sec and the scale bar represents 500 nm. Further details are under “Results”.

To understand the formation of circular structures and how they evolve into stable and thicker rings, we resolved and tracked individual filaments (consisting of several protofilaments) before stable ring formation. Here, we identified nucleation sites where clockwise chiral growth leads to the formation of circular structures (**Figure 4.1B**). Despite the fact that growth seems to be a discontinuous phenomenon limited by the accessibility of soluble protein, we can estimate a mean growth rate (slope p in the kymograph) which was found to be around 60 nm/s. Strikingly, these images also showed filament flexibility (panels 7-12) and breakage (panels 15-18) resulting in the formation of short free fragments. Such fragments were found to glide and "explore" the surface via treadmilling (**4.1C**, indicating that this process fuels filament-filament interactions and therefore formation of closed circular structures. The kymograph in **Figure 4.1C** showed a representative example of one filament growing in the leading edge (p-line) and shrinking in the trailing edge (d-line). A coarse estimation of the velocity of displacement of this filament was about 55 nm/s.

4.1.2 Surface FtsZ concentration -linked to Mg- critically modulates the emergence of dynamic chiral ring-like structures

We further investigated the impact of protein concentration on the stability and dynamics of FtsZ vortex formation, in the presence of GTP (4 mM) and Mg^{2+} (5 mM). Below 0.2 μM , no FtsZ filaments could be detected (**Figure 4.2**). Interestingly, increasing the protein concentration to around 1.0 μM resulted in the formation of abundant three-dimensional polymer networks on the membrane, and no dynamic FtsZ rings were observed (**Figure 4.2**, [Loose and Mitchison, 2014]). These results showed that the self-organization behaviour of membrane-targeted FtsZ polymers was critically dependent on total protein concentration.

Next, we compared the kinetics of protein binding to the membrane at 0.2 μM and 0.5 μM of protein (**Figure 4.3A**), under conditions previously used to detect the swirling rings (see **Figure 4.1**). Upon the addition of GTP (4 mM) and Mg^{2+} (5 mM) a similar membrane adsorption rate (**Figure 4.3**) and the parallel appearance of short and highly dynamic filaments (**Figure 4.3B**) were initially found for the two protein concentrations. Remarkably, the transition from short filaments to rudimentary circular structures (grey area in **Figure 4.3A**) also occurred at similar times in both cases. After a lag time of around 10 min, the adsorption rate was found to be significantly slower at 0.2 μM than at 0.5 μM , suggesting that the kinetics of ring stabilization and widening of the structures was concentration-dependent (**Figure 4.3A**). These differences, found at elapsed times greater than 10 min, also correlated with the fact that the morphology of the rings observed at a protein concentration of 0.2 μM after 45 min incubation (**Figure 4.3B, bottom right panel**) were similar to the ones obtained after a lag time of 20 min when 0.5 μM protein was used (**Figure 4.3B, upper mid panel**). The morphological similarity found at these two time points (denoted as 2 and 3 in **Figure 4.3A**) occurred at a similar protein coverage of the membrane, suggesting that protein surface density, rather than bulk concentration, is the key parameter determining the nature of the network that assembles on the membrane.

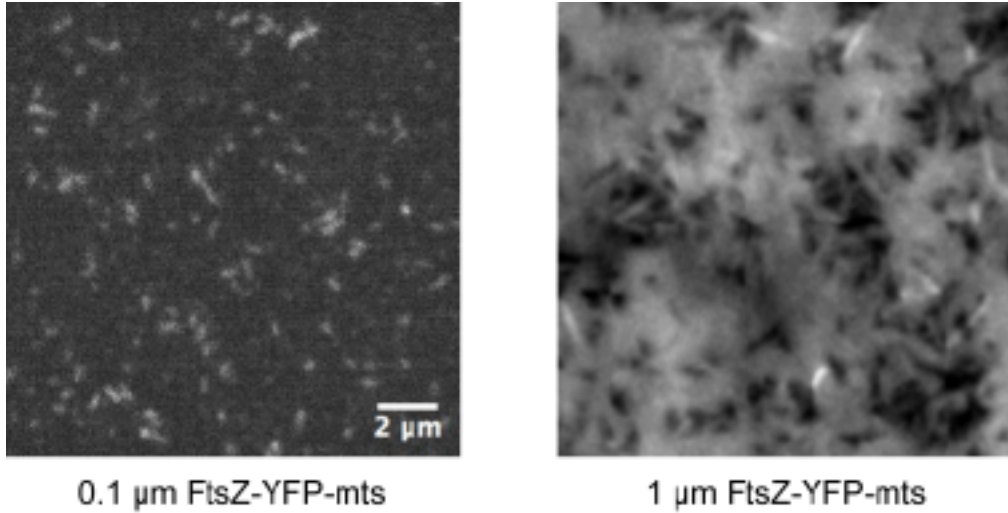


Figure 4.2: Representative images of FtsZ-YFP-mts at low (left panel) and high (right panel) protein concentrations. Only short filaments could be detected at $0.1 \mu\text{M}$, no further structures were later observed. On the contrary, when $1 \mu\text{M}$ of FtsZ-TFP-mts is added, polymer networks were observed almost instantly at the vicinity of the membrane. Dynamic rings were only noticed at intermediated protein concentrations.

The correlation between the morphologies at time points 2 and 3 of **Figure 4.3A** was further established by determining the average diameter of the formed rings to be about $1 \mu\text{m}$ at both protein concentrations, (**Figure 4.3B**). This suggests that although the adsorption rates were different at these time points, the proteins condensed into similar structures.

Then, we monitored the impact of GTP concentration (0.04 , 0.4 , and 4 mM) on the formation of swirlings vortices at fixed protein ($0.2 \mu\text{M}$) and Mg^{2+} (5 mM) concentration. Surprisingly, at the lowest GTP assayed (0.04 mM), a highly ordered mesh of static filaments was found at $t = 0$. These filaments retained a certain degree of curvature and behaved as a nematic phase that entirely covered the membrane area (**Figure 4.4, left panel**). Notably, the surface mean intensity is 3-fold (≈ 1500) increased, compared to the minimal density to form rings (**Figure 4.3**), suggesting that the parallel arrangement of filaments correlates with a high-density regime of protein.

It is known that Mg^{2+} favours self-association and assembly of FtsZ both in solution and at membranes [Monterroso et al., 2013, Rivas et al., 2013]. Therefore, one possibility could be that the free Mg^{2+} controls the surface protein density, rather than the total GTP concentration, since GTP is known to bind Mg^{2+} with affinity in the millimolar range [Menéndez et al., 1998]. To examine this alternative, we repeated the self-organization assays at 0.04 mM GTP in the presence of 1 mM free Mg^{2+} , which resulted in the formation of chiral vortices (**Figure 4.4, right panel**). Interestingly, the emergence of chiral vortices was found to correlate with a significantly lower mean surface protein density than the one measured at 0.04 mM GTP and 5 mM Mg^{2+} which resulted in the dense packing of static

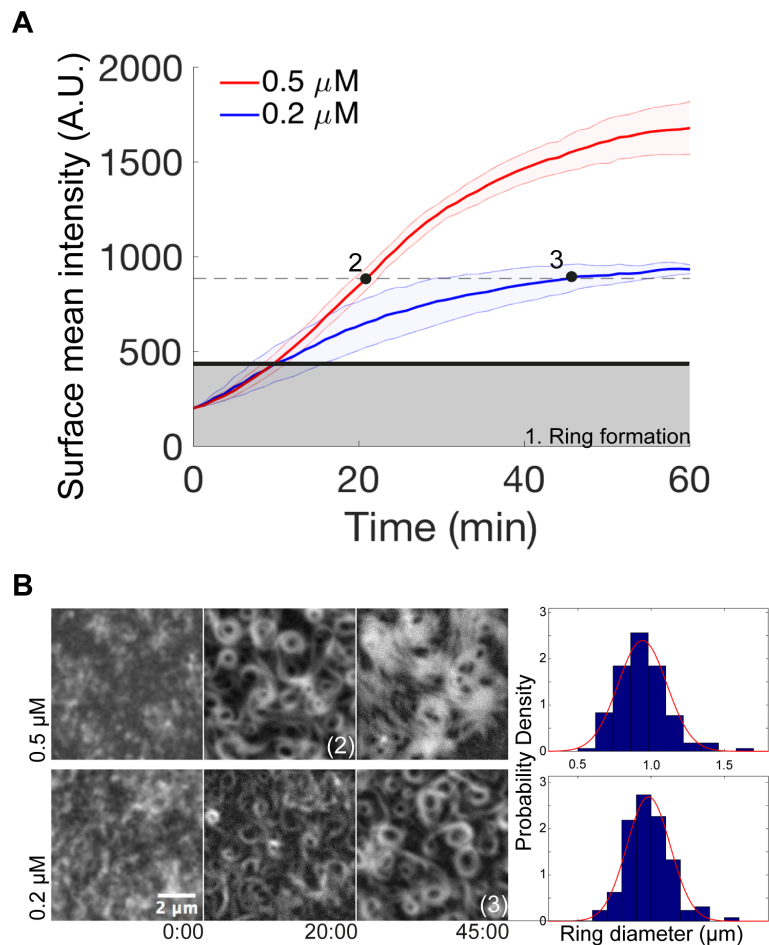


Figure 4.3: Dependence of FtsZ-YFP-mts vortex formation on protein surface concentration. (A) Time-dependence of the average fluorescence intensity of FtsZ-YFP-mts on the bilayer upon 4 mM GTP and 5 mM Mg^{2+} addition, as measured by TIRFM, at 0.2 (blue line) and 0.5 (red line) μM protein concentration. The grey area marks the intensity when first closed rings are observed, which is approximately the same for both protein concentrations. After closed rings have formed, the further accumulation of protein at the surface is strongly concentration dependent. The dashed line represents the phase in which clearly discernible, locally stable dynamic vortices are observed. While at 0.2 μM the system reaches this regime after an elapsed time of 45 min (time point 3), at 0.5 μM it only takes ≈ 20 min (time point 2). (B) Representative images of the experiment shown in panel (A). Frames were taken at elapsed times in minutes. Right: Ring size distributions at time points 2 and 3, indicated in panel (A), with average diameters of $0.94 \pm 0.16 \mu\text{m}$, $N = 140$ and $0.98 \pm 0.14 \mu\text{m}$, $N = 128$ respectively. Size distributions of rings are similar, since both correspond to the same protein surface density (≈ 880 A.U.).

polymers (**Figure 4.4, left panel**). These findings show that free Mg^{2+} controls the concentration of GTP on FtsZ-YFP-mts polymers at the membrane and then the self-assembly of the FtsZ filaments in the membrane.

A similar behaviour was also observed at intermediate GTP concentration (0.4 mM)

4.1 RESULTS

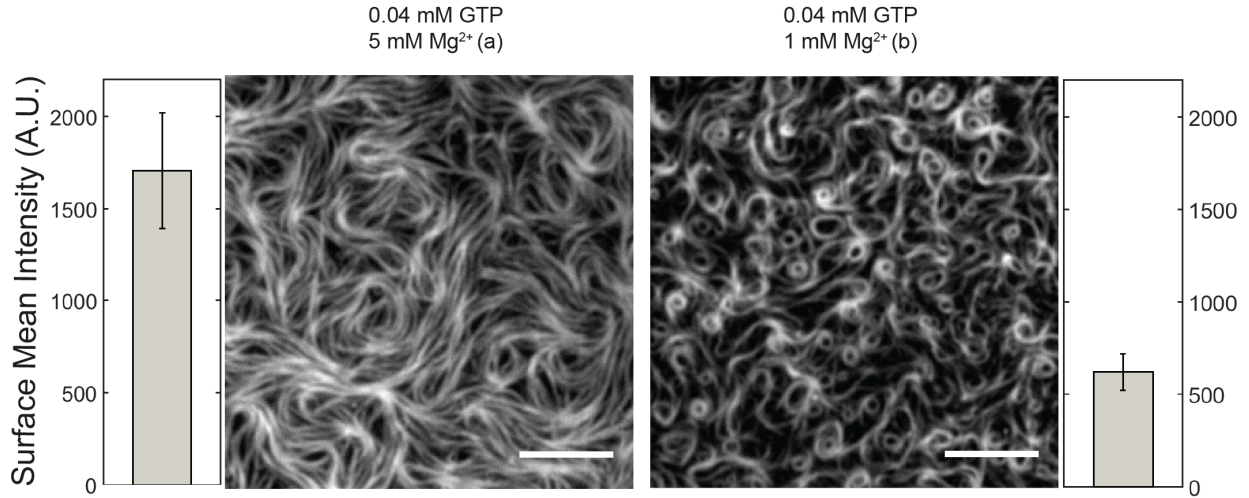


Figure 4.4: Free Mg^{2+} regulates protein surface concentration and thus, self-organization of membrane-targeted GTP-FtsZ. Representative snapshots showing TIRFM images of FtsZ-YFP-mts ($0.2 \mu\text{M}$) polymers on the bilayer taken 2-3 min after the addition of 0.04 mM GTP in the presence of 1 mM and 5 mM free Mg^{2+} concentrations, respectively. Next to each image, the mean fluorescence intensity, proportional to the FtsZ-YFP-mts density on the membrane, is shown (average of 3 experiments). The protein network observed at 5 mM free Mg^{2+} correlates with a high FtsZ-YFP-mts density regime, at least 3-fold larger (≈ 1500 A.U.) than required for ring formation (≈ 500 A.U.).

(**Figure 4.5**). Furthermore, aligned filaments showed no significant change after 10 min, in contrast to dynamic rings (**Figure 4.5**).

4.1.3 Directionality of vortices and destabilization of the trailing edge

After formation, single rings reach a quasi-steady-state as rotating vortices, meaning that the light intensity along their perimeter shows a nearly periodic time dependence. These rotating structures formed by the membrane-targeted FtsZ-YFP-mts (mts C-terminal) consistently showed a chiral clockwise rotation (**Figure 4.6A**). The directional ring dynamics was confirmed by the positive slope of kymographs generated along the ring circumference. Quantifying the slope of the kymograph (see Materials and Methods and **Figure 4.6**) of $N = 60$ rings, we calculated the velocity distribution with a mean velocity of 34 nm/s or $3.9^\circ \text{sec}^{-1}$ for rings of about 500 nm radius (**Figure 4.6D**). Interestingly, the rotational velocities measured here are in good agreement with those reported *in vivo* (30 nm/s), in spite of the significantly reduced complexity of the reconstituted system [Yang et al., 2017, Bisson-Filho et al., 2017].

We next sought to understand whether there was any relationship between the structural features of the protein and the obviously chiral dynamics of our FtsZ mutants. Hence, we made use of previously established chimera variant that was shown to have opposite

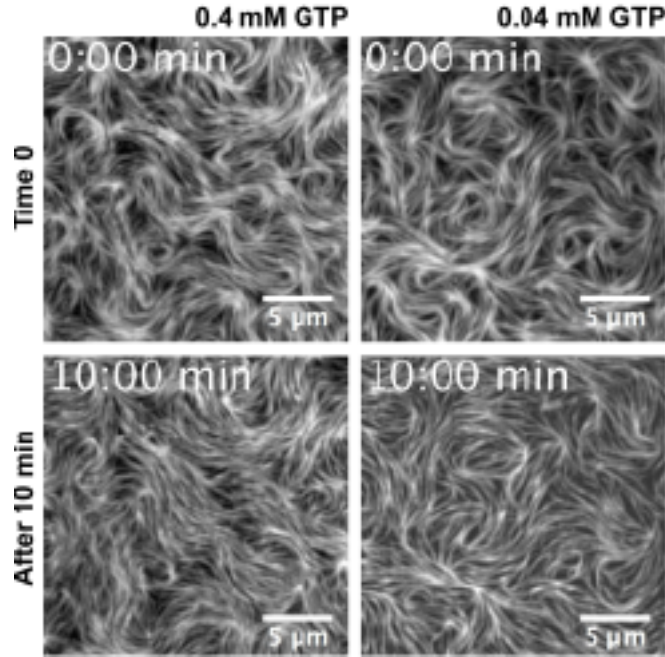


Figure 4.5: Effect of GTP concentration on the FtsZ-YFP-mts rings formation. (A) Images of $0.2 \mu\text{M}$ FtsZ-YFP-mts bundles after the addition of 0.4 mM GTP and 0.04 mM GTP showing long filaments with a parallel arrangement. Images of upper panels were taken 1-2 min (initial acquisition) after GTP addition. Lower panels represent images after 10 min.

effects on deformable membranes [Osawa et al., 2009, Arumugam et al., 2012]. In the presence of GTP, FtsZ-YFP-mts is able to induce inwards (concave) deformations on lipid vesicles. Strikingly, when the mts sequence is switched to the N-terminus, an outwards (convex) deformation is observed [Osawa et al., 2009]. To study the role of the position of the mts in our dynamic vortices, we carried out similar self-organization assays using an FtsZ chimera in which the membrane attachment was located at the opposite, N-terminal, end (mts-H-FtsZ-YFP). Upon addition of GTP and Mg^{2+} , defined dynamic rings were observed (**Figure 4.6B**). Strikingly, now the FtsZ swirls appeared to rotate anti-clockwise, a feature that was confirmed by the negative slope of the kymographs (**Figure 4.6B**). As before, we measured the slope of kymographs for $N = 50$ different rings to calculate the velocity distribution with a mean of about 25 nm/s or $2.8^\circ \text{ sec}^{-1}$ for a ring of 500 nm radius. This velocity is slower than that of the FtsZ-YFP-mts vortices (34 nm/s) (**Figure 4.6D**). These observations show that the positioning of the membrane targeting sequence determines the direction of polymerization as it does for membrane binding and transformation. The fact that the N-terminal mts mutant, without a protein spacer between the FtsZ and the membrane attachment, results in the same qualitative dynamic behaviour, although being inverted in chirality, also refutes potential speculations that YFP may take over a necessary (sterical) role of FtsA [Loose and Mitchison, 2014].

To further investigate how exactly GTP hydrolysis influences the formation of col-

4.1 RESULTS

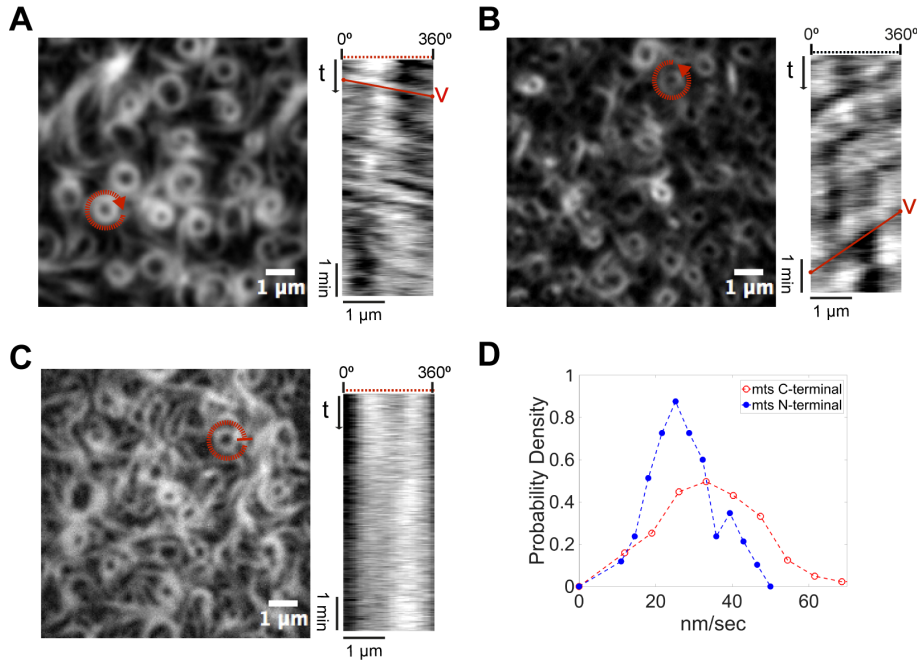


Figure 4.6: Steady-state treadmilling and chirality of FtsZ vortices: dependence on GTPase activity and location of the membrane targeting sequence (mts). (A-C) Left panels: Representative snapshots of the rings formed upon addition of GTP (4 mM) and Mg^{2+} (5 mM) by (A) FtsZ-YFP-mts, whose membrane-targeting sequence is located at the C-terminus of FtsZ, (B) mts-H-FtsZ-YFP, with mts located at the N-terminus of FtsZ, and (C) FtsZ*^[T108A]-YFP-mts, a variant of FtsZ-mts with diminished GTPase activity. Right panels: Kymograph analysis showing (A) a positive slope that corresponds to the apparent clockwise rotation time of the selected ring (red circle), (B) a negative slope that corresponds to an apparent anti-clockwise rotation, indicating that the position of the membrane targeting sequence determines the chirality of the apparent rotation, (C) no apparent slope corresponding to static rings, suggesting that the apparent rotation in (A) and (B) is mediated by GTP hydrolysis. (D) Velocity distributions for FtsZ-YFP-mts (red) and mts-H-FtsZ-YFP (blue) with mean rotational speed values of 34 nm/s and 25 nm/s respectively.

lective streams, we carried out similar self-organization assays using a variant of the FtsZ chimera with no GTPase activity (**Figure A.2**), in which the Threonine at position 108 was replaced by an Alanine (FtsZ*^[T108A]-YFP-mts). Well-defined rings similar in size to the ones found with FtsZ-YFP-mts could be observed upon the addition of GTP and Mg^{2+} (**Figure 4.6C**). Interestingly, these rings did not seem to treadmill and rotate, as evidenced by the lack of clear patterns in the kymographs generated to track polymer dynamics (**Figure 4.6C**). Interestingly, FtsZ*^[T108A]-YFP-mts rings grow from nucleation points in a less dynamic manner compared to FtsZ-YFP-mts. From these results, we conclude that GTPase activity is not required for the formation, but for the quasi-steady-state rotational dynamics of the ring patterns, suggesting that GTPase activity particularly promotes filament destabilization in the trailing edge.

4.1 RESULTS

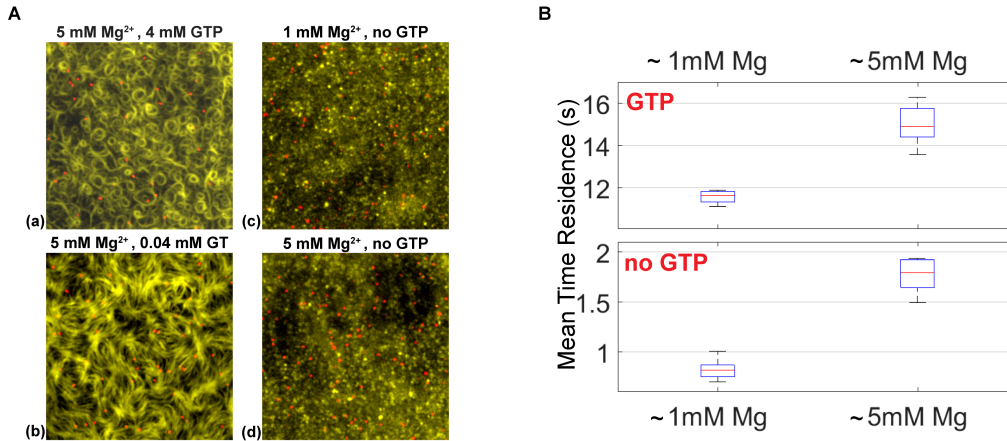


Figure 4.7: Residence times of single membrane-targeted FtsZ molecules at the bilayer, dependent on nucleotide and free Mg^{2+} (A) Overlaid images of FtsZ-YFP-mts structures (yellow channel) incubated with GFP-Booster-Atto647N (nanobody) (single molecules: red channel) in the presence of GTP (a, b), GDP (c, d) and indicated free Mg^{2+} concentration. The protein concentration in all cases was $\approx 0.2 \mu\text{M}$. (B) Mean residence times of FtsZ-YFP-mts were calculated using an exponential fit of the cumulative residence time distribution. Mean residence times were measured for different GTP and Mg^{2+} conditions.

Treadmilling can be explained by an imbalance between growth and shrinkage at the two opposite ends of the polar filament. Since treadmilling is obviously GTP turnover-dependent, and the growth into ring-like structures by capturing pre-formed diffusing filaments is not, the critical requirement for treadmilling seems to be the destabilization and shrinkage at the trailing edge. In order to directly visualize the destabilization dependent on nucleotide state, we developed a single molecule assay using FtsZ-YFP-mts incubated with fluorescently labelled nanobodies (GFP-Booster-Atto647N, see Materials and Methods) (**Figure 4.7A**) to investigate the protein turnover at the membrane, implying that faster disassembly suggests higher destabilization. By measuring the probability of protein detachment as a function of time (**Figure A.3**), we could calculate the mean residence time of single FtsZ subunits within the filaments on the membrane. Using this analysis, we found that the mean residence time of FtsZ-YFP-mts in fragments forming dynamic rings was $t_r = 11.5 \text{ sec}$ (**Figure 4.7**), in good agreement with previous FRAP studies with native FtsZ [Anderson et al., 2004, Chen and Erickson, 2005]. These residence time turns out to be significantly faster than for the GTP hydrolysis-deficient mutant FtsZ*^[T108A]-YFP-mts, (**Figure A.3**, similar to the photobleaching time scale contribution $\approx 32 \text{ sec}$). Interestingly, by considering the rotational speed as measured in **Figure 4.6D** and this residence time, we reason that rings are assembled by multiple filaments that treadmill in a synchronized manner, with a mean length of $\langle l \rangle = \underline{v} * t_{res} = 390 \text{ nm}$ (78 monomers). In comparison, *in vitro* assembly of native FtsZ showed shorter filaments, that were on average 120 to 200 nm long (30-50 monomers) [Loose and Mitchison, 2014]. In addition, we measured the residence time without GTP (GDP form) with 1 mM free Mg^{2+} . As-

4.2 DISCUSSION

suming that the residence time of a polymer of n -monomers scales to the power of n ($t_r^{pol} \sim (t_r^{mon})^n$), one can estimate that the residence time associated to one monomer is ≈ 1 sec, which agrees with our results (≈ 0.8 sec) in GDP form at 1 mM free Mg^{2+} .

Our single molecule experiments also allowed to directly elucidate the impact of free Mg^{2+} and in particular, the obvious role in the formation of the high density FtsZ mesh. It was found that the protein release from the membrane upon GTP addition was slower at 5 mM $t_r = 15.1$ sec than at 1 mM free Mg^{2+} (**Figure 4.7B**). These findings represent compelling evidence that the formation of a high-density mesh of filaments is linked to the slow detachment of protein, at least when compared to the dynamic rings at lower free Mg^{2+} (1 mM). Also, the residence time of FtsZ in GDP form at 5 mM free Mg^{2+} was increased $t_r = 1.72$ sec compared to 1 mM. This general increase in the residence time implies that lateral interactions (bundling), favoured by free Mg^{2+} , promote larger and more crosslinked polymeric species with higher membrane affinity and less susceptibility to destabilization.

4.2 DISCUSSION

In our minimalistic *in vitro* reconstitution study, we found that polymers of an artificially membrane-targeted variant of FtsZ autonomously and without the presence of FtsA self-organize on a supported bilayer upon addition of GTP and Mg^{2+} , to form chiral ring-like dynamic patterns (**Figure 4.1**), displaying a clockwise or anti-clockwise protein movement, dependent on whether the membrane attachment was enforced through the C-terminal or N-terminal end of the protein, respectively (**Figure 4.6A-B**). The membrane targeting sequence in both cases was taken from MinD, one of the elements of the site-selection MinCDE complex, which allows FtsZ to be peripherally attached to the membrane. We thus showed that the ability of FtsZ to create dynamic patterns is an intrinsic property (**Figure 4.1A**) rather than a specific interaction with a specific protein anchor. Instead, the formation of dynamic FtsZ ring structures *in vitro* is highly linked to (i) the surface protein density and (ii) GTPase activity, destabilizing surface-bound filaments and thus being key for treadmilling [Yang et al., 2017].

We found that the most decisive factor for the emergence of dynamic vortices of FtsZ on membranes is the overall surface coverage by protein monomers and filaments (**Figure 4.8A**), which varies over time upon protein adsorption to the membrane (**Figure 4.3**) and is controlled by free Mg^{2+} concentration (**Figure 4.4**). Dynamic vortices appear primarily in an intermediate density regime (surface mean intensity: 450-1000 A.U.) and isotropic bundles in a high-density regime (surface mean intensity > 1000 A.U.). Transitions from highly dynamic vortices to isotropic bundles occur upon an increase in lateral contacts that arrest treadmilling filaments, increasing their mean effective length (as in the case of ZipA [Loose and Mitchison, 2014]). This was clearly observed in our single molecule assay (**Figure 4.7B**) that shows a slower turnover in the situation of dense isotropic bundles, i.e., longer filaments. Along these lines, the increase in lateral interactions at high free Mg^{2+} also explains the rapid formation of filaments at 5 mM free Mg^{2+} (**Figure 4.7**),

since larger FtsZ assemblies bind to the membrane and interact with each other more frequently (**Figure 4.7B**). Presumably, the main reason why Loose and Mitchison failed to observe dynamic vortices in the case of the FtsZ-YFP-mts [Loose and Mitchison, 2014], is because of the high protein concentration used in their experiments (1.5 μM).

Interestingly, our results are compatible with previous atomic force microscopy analysis of static structures formed by FtsZ polymers on mica as a function of protein concentration at the surface [Mingorance et al., 2005]. The protein concentration-dependent formation of dynamic FtsZ patterns also nicely correlates with a recent theoretical study suggesting that protein density at the membrane controls the formation of vortex patterns on membranes in a phase-like behaviour [Denk et al., 2016]. According to this, independent curved polar filaments showing chiral motion and repulsion can self-assemble into vortex or ring-like structures in an intermediate density regime. While at low protein densities, filaments travel independently, at the high-density regime they form isotropic networks and jammed bundles [Weiss, 2004].

With gradually increasing protein concentration on the membrane, we were able to investigate the initial formation phase of dynamic rings. At low density (surface mean intensity < 450 A.U.), curved and polar filaments initially emerge from nucleation points, which presumably are small attached filaments above a critical length. Intriguingly, the overall adsorption rates to the membrane at this stage are similar for protein concentrations of 0.2 μM and 0.5 μM (**Figure 4.3A**). Upon sufficiently high membrane coverage of nucleating filaments after the initial phase, protein binding from solution begins to scale with total (i.e., bulk) protein concentration. Whether nucleators are directly formed on the membrane after GTP addition or whether short polymers are formed in solution and an increase in affinity with growth brings them to the membrane cannot be determined based on our data, and will be the topic of further investigation.

We found that filaments growing from nucleators are prone to fragmentation, resulting in free fragments which may stay connected to the membrane. There, they assemble with other attached filaments by diffusion and directional treadmilling, which ultimately results in closed rings, in which the treadmilling continues. Our experiments demonstrate that treadmilling, particularly via destabilization of the trailing edge, is highly regulated by GTPase activity. When GTPase activity is switched off (FtsZ*^[T108A]-YFP-mts), rings seemed to grow only from nucleation points and do not treadmill, at least on time scales found for FtsZ-YFP-mts (**Figure 4.6C**). Moreover, the residence time of single FtsZ*^[T108A]-YFP-mts subunits in the filaments is comparable with the photobleaching control, implying that protein turnover is almost non-existent (**Figure A.3**). It has been suggested that a kinetic and structural polarity, at monomeric level, and a GTP/GDP gradient are requirements for robust treadmilling [Wagstaff et al., 2017]. As seen from our experiments of the initial vortex growth phase, a GTP/GDP gradient along the treadmilling direction is likely to result from the preferential addition of GTP subunits to the existing filaments at the polar front, and a more likely GTP turnover towards the "older" tail.

In light of the role of GTPase activity for the formation of dynamic vortices, the measured velocity of the FtsZ + FtsA vortices reported by Loose and Mitchison is about three-fold faster (108 nm/s) compared to our FtsZ-YFP-mts rings (34 nm/s). In addition, these

authors reported a higher GTPase activity of the FtsZ + FtsA compared the FtsZ-YFP-*mts*. Nonetheless, it is not clear how variables such as GTPase activity and attachment strength influence the speed of rotation. For instance, our mutant *mts*-H-FtsZ-YFP has shown a considerable decrease in rotation speed compared to the FtsZ-YFP-*mts*. Remarkably, to observe *mts*-H-FtsZ-YFP dynamic rings, we had to increase the bulk concentration to 1.25 μM . This may be due to a reduced affinity for membranes, affecting the overall dynamics as discussed above.

The most remarkable outcome of this study is the clear dependence of vortex chirality on the positioning of the membrane anchor, which in turn has severe effects on the topology of membrane deformation by FtsZ. Chirality is inverted by switching the membrane anchor from the C-terminus (clockwise) to the N-terminus (anticlockwise). Intriguingly, these two different mutants cause concave (C-terminal) or convex (N-terminal) deformations when bound to deformable liposomes [Osawa et al., 2009]. To explain these different deformations, Erickson and coworkers have previously depicted FtsZ filaments as arc segments with a direction of membrane attachment either parallel or antiparallel to the vector of curvature. In order to support the here observed chiral treadmilling of curved rings on planar membranes, however, attachment through the preferential binding face of the filaments needs to have a perpendicular component to both, the ring curvature and filament polarity. **Figure 4.8B** shows a curved filament with a C-terminal (clear gray) and N-terminal (dark gray) face perpendicular to the curvature of the filament. Note that the *mts* is represented here with one parallel component to the curvature, as suggested by Erickson, and one perpendicular component to accommodate flat membrane binding. In this flat representation of a curved FtsZ filament, treadmilling is explained by a polar growth at the leading edge and a destabilization mechanism, driven by GTP hydrolysis, towards the GDP enriched region at the trailing edge [Wagstaff et al., 2017].

Nevertheless, the fact that curved structures can be either attached along their axis of apparent curvature (*in vivo*, Osawa & Erickson [Osawa et al., 2009]) or perpendicular to their axis of primary curvature (as reported here), we have to conclude that either the membrane attachment of the filament is immensely flexible, or – and this is more likely based on previous structural investigations – that the filament does not have a single, but rather more than one direction of curvature, like a helix or a twisted arc [Arumugam et al., 2012, González de Prado Salas et al., 2014]. Indeed, a very similar geometry with more than one curvature direction has recently been reported for ESCRTIII filaments (nicely reviewed by Chiaruttini and Roux [Chiaruttini and Roux, 2017]). This is particularly intriguing, as among many other roles in eukaryotic and prokaryotic cells connected with membrane abscission, ESCRT is the alternative system to FtsZ with respect to cell division in Archaea [Samson et al., 2008, Lindas et al., 2008].

Therefore, in the light of evidence showing that FtsZ forms helical structures *in vivo* [Thanedar and Margolin, 2004, Niu and Yu, 2008, Fu et al., 2010, Holden et al., 2014] and *in vitro* [Arumugam et al., 2012], we here suggest an alternative structural model to the one depicted in **Figure 4.8B** (**Figure 4.8**). We propose that an FtsZ filament with more than one main direction of curvature, such as a helix, would much more elegantly accommodate the combination of inwards/outwards deformations and chiral treadmilling for the opposite

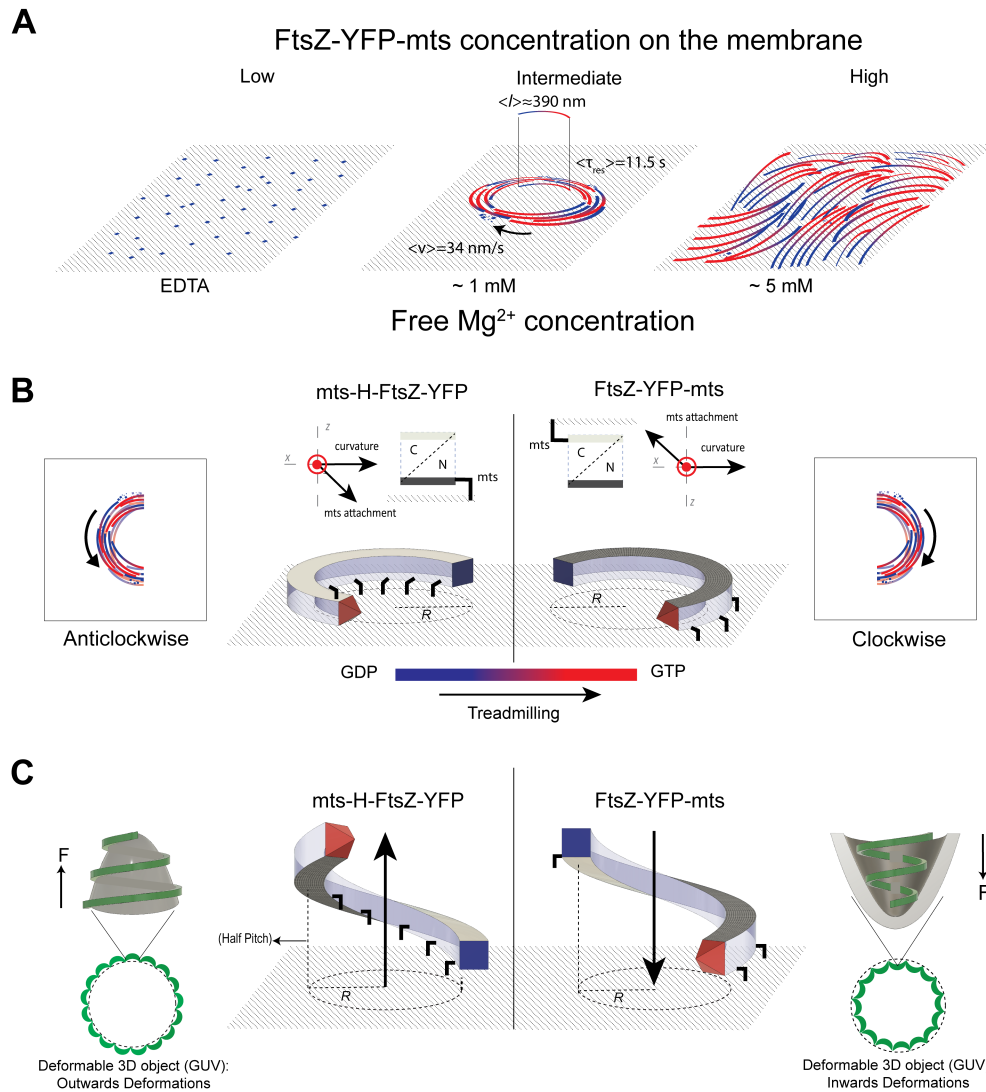


Figure 4.8: (A) FtsZ-YFP-mts ring formation is dependent on GTP and protein surface concentration. At low protein concentration and no GTP and Mg^{2+} , FtsZ transiently binds to the membrane without forming visible structures. With GTP, dynamic chiral rings are formed as a function of time. Once stable swirls are built, they exhibit a mean velocity of 34 nm/s and a turnover time of short fragments of 11.5 sec. From the velocity and the turnover time, the average length of the protofilaments can be estimated to 390 nm. However, ring formation is only observed at intermediate protein density regimes. At high protein density, a parallel network of filaments (nematic phase) is observed. (B) To guarantee chirality, attachment needs to have a perpendicular component to both, the ring curvature and filament polarity to have a preferential binding face. In this case, the mts interacts with the flat-surface on opposite sides of the FtsZ filament, so curvature is also in the opposite direction. (C) We here suggest that an intrinsic helical FtsZ shape, characterized by a radius and a pitch, can alternatively explain previous FtsZ induced inwards/outwards deformations in the following way: due to the intrinsic pitch, the growing filament would either pull up (left) or push down (right) the surface. On the contrary, if the surface is not deformable (SLB), the filament would experience a strain, get destabilized, and eventually break upon growth.

mts mutants. Such a cork-screw like FtsZ filament can be simply described by an intrinsic radius and a pitch, where the latter would reflect on the attachment direction (**Figure 4.8C**). On a deformable surface (deflated liposome), the growing filament would either pull up (left) or push down (right) the surface due to the respective pitch. The interplay between the elastic response of the membrane (increased membrane tension) and local changes in the helix radius, due to GTP hydrolysis [Huecas and Andreu, 2004, Lu et al., 2000], could explain the stabilization of higher curvature or smaller radii regions (**Figure 4.8C**). On a non-deformable surface (SLB), however, since the surface is not resilient, the filament would experience a strain, get destabilized, and eventually break upon growth.

Thus, together with the very recent studies showing the linkage between treadmilling of FtsZ polymers and peptidoglycan synthesis in *E. coli* [Bisson-Filho et al., 2017] and *B. subtilis* [Yang et al., 2017] cells, our findings shed new light on the interplay between FtsZ structure and treadmilling dynamics, but may also hint to a direct mechanical link of these to bacterial division. The minimal system we used unambiguously shows that the observed chiral vortices are the result of intrinsic GTP-linked FtsZ polymerization dynamics on the membrane without the need of additional complex interactions with FtsA and ATP, pointing to a fascinating archetypal feature of this important structural protein. The reduced number of components allowed us to selectively determine the influence of key factors, e.g. the surface density of FtsZ, on the self-organization behaviour, thus contributing to a much better mechanistic understanding of FtsZ's dynamic architecture and its potential physiological implications.

Chapter 5

Site directed mutagenesis, insertions and deletions to tune the treadmilling dynamics of FtsZ-YFP-*mts* rings

FtsZ is one of the key elements in the bacterial cell division machinery and its role as a spatial regulator of cytokinesis seem to be highly mediated by its intrinsic treadmilling dynamics. Here, we dissect the role of lateral interactions, GTPase activity, and membrane affinity on the treadmilling dynamics in the chimera FtsZ protein. By reconstituting different FtsZ-YFP-*mts* variants, in agreement with previous work, we showed that membrane binding and control over lateral interactions are paramount for ring formation, while GTPase activity directly affects treadmilling dynamics. We also report for the first time that membrane binding has a direct effect on the ring rotational speed vortices. The ability to lead to form dynamic vortices in response to different biochemical changes shows a dramatic robustness, where only significant changes, such as null membrane binding or the absence of control over lateral interactions are detrimental for the formation of treadmilling rings.

5.1 RESULTS

5.1.1 Inefficient membrane binding and absent of lateral interactions hinder FtsZ-ring formation

As previously described by Osawa et al., membrane-targeted FtsZ chimeric proteins, possessing the amphipathic helix of *Escherichia coli* MinD, enable the formation of Z rings in liposomes [Osawa et al., 2008]. However, so far it remained rather ambiguous how a membrane tether could induce the assembly of dynamic vortices. Also, control over lateral interactions has been showed as an important cue for the correct FtsZ assembly in *Caulobacter crescentus* [Sundararajan et al., 2018]. In order to elucidate the role of membrane anchoring and lateral surface interactions for the formation of dynamic FtsZ *E. coli* rings, we generated two FtsZ-YFP-mts mutants with either a defective membrane binding motif (FtsZ-YFP-mts*^[L629E]) or a deficiency in the lateral interaction site (FtsZ^{Δ-CTL}-YFP-mts).

Both FtsZ-YFP-mts mutants displayed distinct and sequence-specific phenotypes compared to the wild type form (**Figure 5.1**).

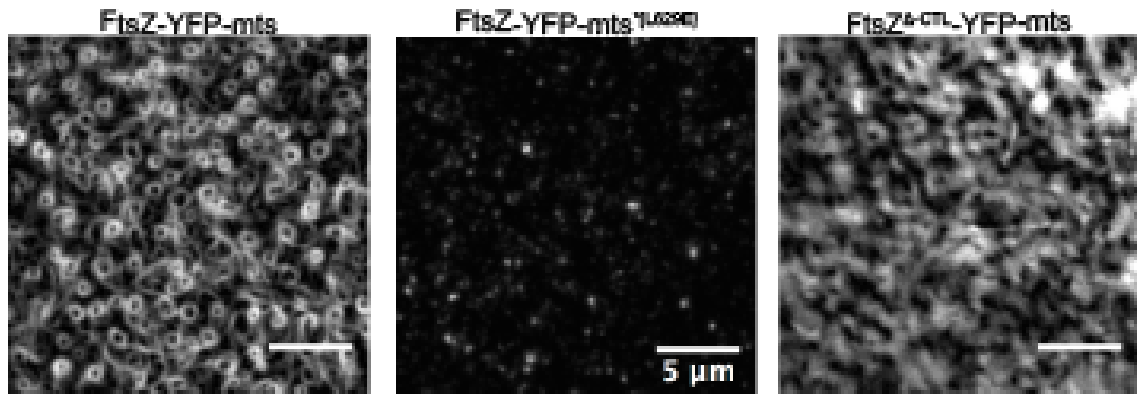


Figure 5.1: The ability of FtsZ-YFP-mts to assemble into treadmilling rings is impaired when membrane binding and lateral interactions are disrupted. Representative snapshots of the in vitro reconstitution of 0.5 μM FtsZ-YFP-mts, 0.5 μM FtsZ-YFP-mts*^[L629E], and 1 μM FtsZ^{Δ-CTL}-YFP-mts on *E. coli* polar lipid extract membranes (4 mM GTP and 5 mM Mg²⁺). (middle panel) FtsZ-YFP-mts*^[L629E] binds as isolated patches to the *E. coli* polar lipid extract membrane. Cooperative protein binding does not seem to overcome binding deficiency, thereby highlighting the importance of membrane binding for FtsZ filaments self-organization. (right panel) FtsZ^{Δ-CTL}-YFP-mts forms filamentous structures on the supported lipid bilayer. The regulation of lateral interactions through CTL seems to be crucial for self-assembly into well-defined rotating vortices.

Considering the FtsZ-YFP-mts*^[L629E], which possess a previously reported disruptive mutation in the membrane target sequence of the *E. coli* MinD [Szeto et al., 2002], only small protein patches were evident on the membrane surface (**Figure 5.1, middle panel**). A sedimentation analysis showed that polymerization properties were impaired when compared with the chimera with the native mts-MinD (**Table B.1**), over time no curved

filaments or vortices were formed since this mutant is incapable to form long oligomers in the presence of GTP and Mg^{2+} . In contrast to the results obtained for the membrane binding deficient mutant, defects in the lateral interaction site had no impact on membrane recruitment or curved filament formation. However, these filaments did not organize further into dynamic vortices (**Figure 5.1, right panel**).

In summary, we concluded that membrane binding and the regulation of lateral interactions are two crucial factors for the formation of dynamic FtsZ rings. It also seems that oligomerization properties play an important role, it could have been the case in the mutant *[L629E] that the presence of long oligomers could have counteracted the weak membrane binding conferred by such mutation.

5.1.2 Mutations in the FtsZ GTPase domain have a direct effect on FtsZ ring treadmilling

In a recent study about the GTPase activity of FtsZ, Yang et al. 2017 were able to show that treadmilling is controlled by GTP hydrolysis and that such dynamics are involved in the spatial organization of the PG synthesis machinery [Yang et al., 2017]. Due to this revelation, we decided to investigate the effect of GTPase activity on the dynamics of FtsZ vortices. For this purpose, two previously reported sequence alterations in the GTPase domain of FtsZ were introduced into the chimeric FtsZ-YFP-mts protein (D212G and D229A). In contrast with previous publications reporting that defects in GTP hydrolysis affect FtsZ polymerization *in vitro* [Lu et al., 2000], our experimental conditions (0.2 - 0.5 μ M, 4 mM GTP, 5 mM Mg^{2+}) enabled the self-assembly of all chimeric protein variants into FtsZ vortices (**Figure B.1, left and middle panels**).

[D212G] mutation on FtsZ wild-type was shown to display normal GTP binding, but completely lack of GTPase activity [Mukherjee and Lutkenhaus, 1994]. Contrary, FtsZ^[D212G]-YFP-mts exhibited almost ten-fold reduced GTPase activity, when compared to FtsZ-YFP-mts (**Figure 5.2 B**). When considering the kymograph of FtsZ*^[D212G]-YFP-mts we could furthermore determine that the protein assembled into static rather than dynamic vortices of $\approx 1 \mu$ M diameter (**Figure 5.2C and Figure 5.2D**). In contrast, *[D299A] mutation displays a 2-fold increased of GTPase activity *in vivo* [Stricker and Erickson, 2003]. However, FtsZ*^[D299A]-YFP-mts did not exhibit increased GTPase activity but rather a 2-fold decreased (**Figure 5.2B**) than the chimera with a wild type FtsZ moiety. In terms of velocity of the rings, FtsZ*^[D299A]-YFP-mts vortices showed a reduced rotational speed of 25 nm/s compared to 34 nm/s for FtsZ-YFP-mts (**Figure 5.2D, right panel**).

In summary, we concluded that our results support the observations made by Yang et al. 2017 and highlight the role of the GTPase activity for FtsZ treadmilling and the resulting dynamic of the FtsZ vortices [Yang et al., 2017].

5.1 RESULTS

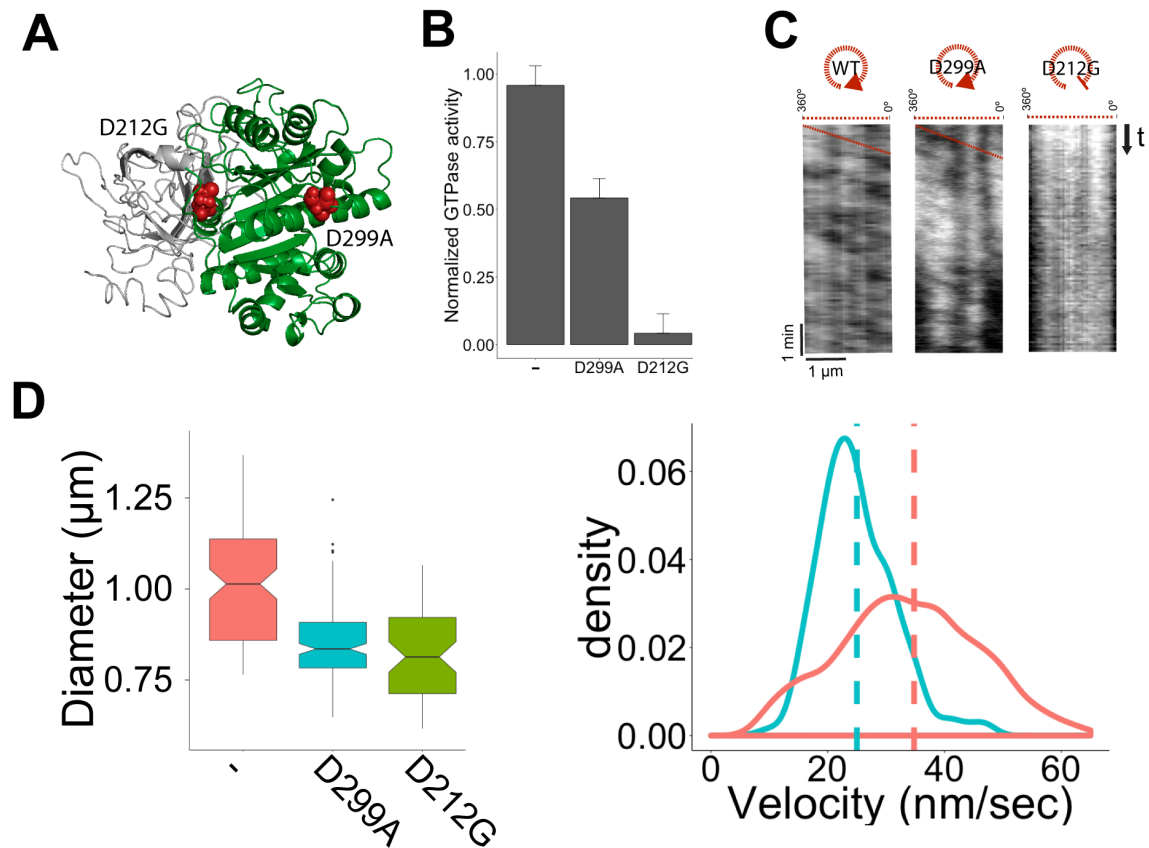


Figure 5.2: GTPase activity has a direct effect on FtsZ treadmilling. (A) Representative protein 3D structure highlighting (red dots) the point mutations in the GTPase domain of FtsZ (green). (B) Bar plot displaying the normalized GTPase activity of each chimeric protein. Compared with the chimera with the WT moiety, *[D299A] exhibits only half of its GTPase activity, while *[D212G] possess reduced GTPase activity. (C) Kymograph analysis showing a negative slope corresponding to the FtsZ treadmilling in the chimera with the WT moiety and in the *[D299A] mutant. In contrast *[D212G] displays no apparent slope, thus represents the static behaviour of the corresponding rings. These results suggest that the rotation in the first two kymographs is mediated by GTP hydrolysis. (D) Representative plots of the FtsZ ring diameter and velocity distributions. The colour code is the same for both plots: red – FtsZ-YFP-mts, cyan – *[D299A], green – *[D212G]. The boxplot in the left panel shows the mean diameter of the FtsZ ring for each protein variant. The mean ring diameter of the GTPase mutants seems to be smaller than the chimera with the WT moiety. The right panel displays the velocity distributions for the chimera with the WT moiety and the chimera with the *[D299A] mutation. Compared to the wild-type chimera FtsZ-YFP-mts (34 nm/s, n = 1359), FtsZ*[D212G]-YFP-mts exhibits a reduction in the mean rotational speed (25 nm/s, n = 216).

5.1.3 Binding affinity of the membrane targeted sequences (mts) has a direct impact on FtsZ treadmilling

In order to clarify the impact of the membrane tethering process on the dynamic behaviour of FtsZ filaments, we generated a new FtsZ-YFP-mts variant with a membrane target sequence of FtsA. This protein variant possesses the membrane target sequence of *E. coli* FtsA (mts[FtsA-*E. coli*]), FtsZ's natural anchor to the membrane [Pichoff and Lutkenhaus, 2005] and that in preliminary binding assays showed higher binding affinity when compared with the chimera FtsZ-YFP-mts[MinD-*E. coli*] protein (data not shown). As in the previous reconstitution experiments, self-organization of the new chimeric variant was promoted in a protein concentration of 0.5 μM and in the presence of GTP and Mg^{2+} . The new construct was able to bind to the supported lipid bilayer system, assemble in filaments and organize into higher-order structures (vortices) (**Figure B.1, right panel**).

To examine the differential binding affinities of our mts-constructs to supported lipid bilayers, we made use of a label-free *in vitro* method: quartz crystal microbalance with dissipation monitoring (QCM-D). QCM-D allows the monitoring of the real-time attachment of proteins to artificial membrane systems (**Figure B.2**). Here, the frequency (Δf) change can be extrapolated to changes in mass, giving an indication of the adsorption of material on the surface. Furthermore, this technique enables the estimation of the apparent binding affinity through changes in the measured frequency upon protein titration. In our experimental approach we considered two different conditions (**Figure 5.3B**): i) in the presence of 4 mM GTP and Mg^{2+} , where mainly long oligomers and polymers are present; ii) in the presence of 4 mM GDP and Mg^{2+} , where short oligomers are present.

We retrieved binding curves by fitting a Hill equation **Equation 5.1** to the data to calculate the apparent binding coefficients as shown elsewhere [Renner and Weibel, 2012].

$$\Gamma(c) = \frac{c^n}{K_d + c^n} \quad (5.1)$$

The surface coverage binding or in other words the binding affinity of each mts-variant to the supported lipid bilayer is given by Γ with respect to the protein concentration c . K_d is expressed as the equilibrium dissociation constant and n relates to the Hill coefficient that gives information about the cooperativity. Since we can not really tell if the affinity of an mts-variant will increase once bound to the bilayer, we decided to fix $n = 1$.

It is interesting to note that the protein with a defective membrane binding (Control, FtsZ-YFP-mts*^[L629E]) displayed a high K_d in both conditions ($K_{d-GDP} = 87$, $K_{d-GTP} = 81$), highlighting the inability of this protein to bind to the SLB. The variant with mts[MinD-*E. coli*] ((a)) in the GDP form as a higher K_d ($K_{d-GDP} = 31$) than in the GTP form $K_{d-GTP} = 2$, that correlates with the presence of short versus long oligomers. Finally, the variant with a mts[FtsA-*E. coli*] ((b)), gave low K_d values in both conditions ($K_{d-GDP} = 2$, $K_{d-GTP} = 1$). Strikingly, the increase in membrane affinity was accompanied by a reduction of the rotational speed compared to the *E. coli* MinD mts chimera (**Figure 5.3C**).

5.1 RESULTS

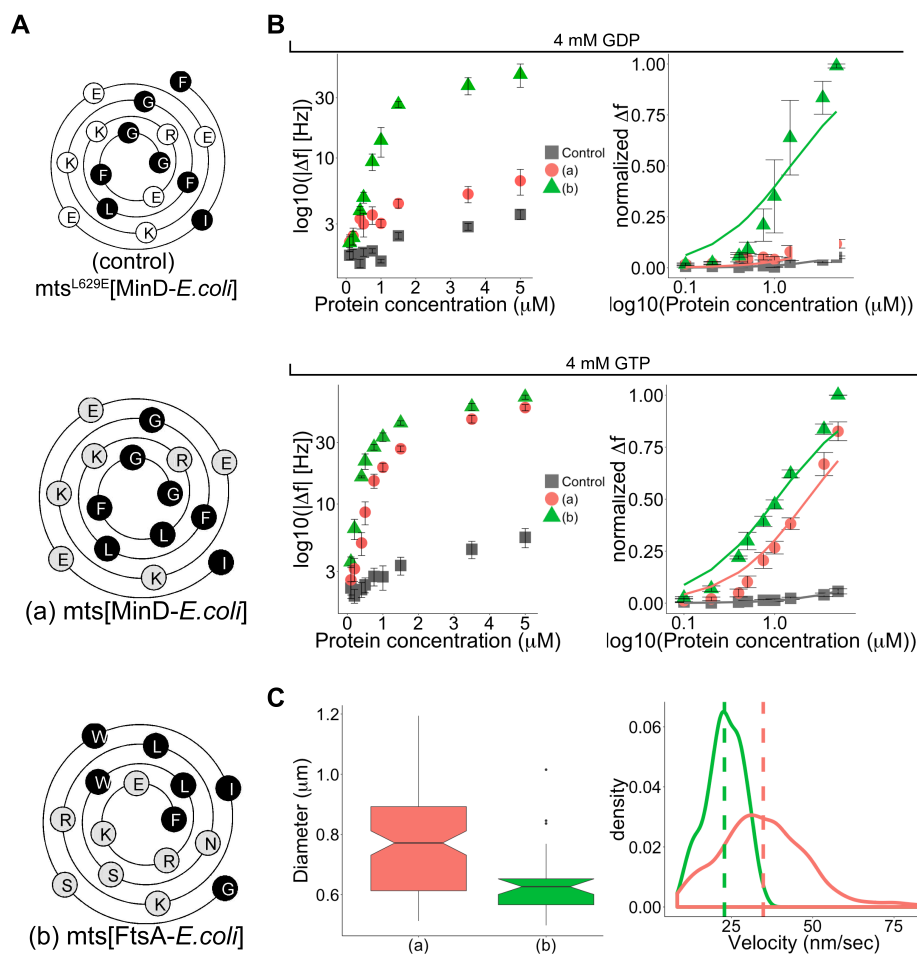


Figure 5.3: Increased membrane affinity correlates with slower treadmilling of FtsZ filaments. (A) Wenxiang diagram representing the amphipathic membrane target sequences used. The plot depicts the conical projection of each alpha-helix onto a plane, with the C-terminus of the helix in the centre and the N-terminus at the edge. Hydrophobic sides are highlighted black and hydrophilic sides in grey. (B) FtsZ chimeric protein adsorption to DOPC:DOPG (70:30 mol%) supported lipid bilayers: red, $mts[MinD-E. coli]$; green, $mts[FtsA-E. coli]$ and grey, $mts^{*}[L629E]$ mutation that detracts membrane binding. Left plots display the measured frequency change measured for the mts -variants. Right plots display the normalized Δf . Measurements were performed in the presence of 5 mM Mg^{2+} and 4 mM GTP (upper panel) or 5 mM Mg^{2+} and 4 mM GDP (lower panel). Measured frequency changes (9th overtone) depict the addition of protein mass to the SLB and thus enable to estimate binding affinities. (C) Diameter and velocity distributions of FtsZ chimera vortices. The boxplot in the upper panel displays the mean diameter of the rings obtained for each protein variant. The mean diameter of the mts variant seems to be smaller than the chimera with $mts[MinD-E. coli]$. The lower panel shows the shift in velocity in (b) when compared to (a), with mean rotational speed values of 23 nm/s ($n = 305$) and 34 ($n = 1359$) nm/s respectively.

5.1 RESULTS

Overall, higher membrane affinity seems to lead to a slower rotational speed of approximately 24 nm/s ($n = 156$) (Figure 5.3C).

5.1.4 Treadmilling tuning by the presence of FtsZ-YFP-*mts*-His₆ variant

Finally, we decided to mimic the interaction of FtsZ to the membrane when ZipA is the tether protein. For such interaction, we generated a variant with a His₆-tag on the C-terminal side of our chimera protein FtsZ-YFP-*mts*. In this sense, in the presence of NTA-lipids on the supported bilayer, our protein will self-organize in a similar way as when FtsZ-ZipA interact together in co-reconstitution experiments [Mateos-Gil et al., 2012a, Martos et al., 2015].

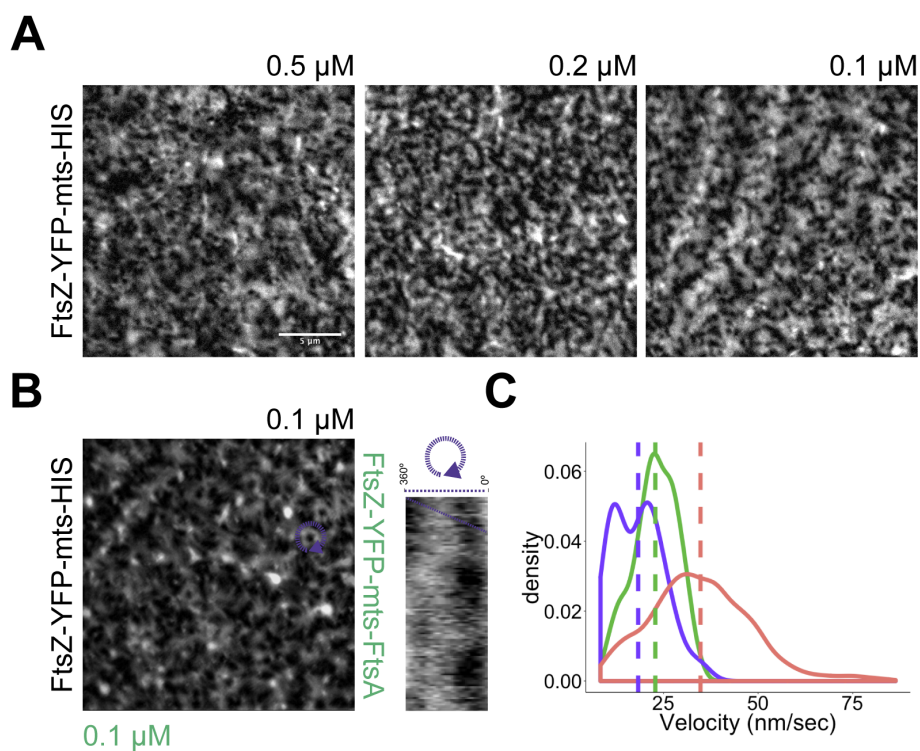


Figure 5.4: A) Representative snapshots of FtsZ-YFP-*mts*-His₆ variant on (*E. coli*) supported membranes doped with 1% DGS-NTAP in the presence of 4 mM GTP and 5 mM Mg²⁺, at different protein concentrations. B) Representative snapshot of a 1:1 titration of FtsZ-YFP-*mts*-His₆ variant and FtsZ-YFP-*mts*[FtsA-*E. coli*], kymograph analysis showed that apparent rotational movement of such rings. Velocity distribution of the Z-rings depicted in (B) -purple- compared with samples were only FtsZ-YFP-*mts*[FtsA-*E. coli*]-green- and FtsZ-YFP-*mts*[MinD-*E. coli*]-red-. Mean velocity were 20 nm/s ($n = 16$), 23 nm/s ($n = 305$) and 34 ($n = 1359$) nm/s respectively.

It has been reported that in the presence of 1% DGS-NTA, FtsZ-sZipA (His₆-tagged)

can form circular structures [Krupka et al., 2018]. We then, tried to mimic such conditions with our His₆-tagged variant using different protein concentrations (0.5, 0.2 and 0.1 μM) in the presence of 4 mM GTP and 5 mM Mg²⁺ (**Figure 5.4A**). We observed the formation of short curved filaments and some closed circular structures on the membrane, and the lower the protein concentration the more likely it is to observe circular structures. We decided to measure the rotational speed of the rings formed by the FtsZ-YFP-*mts*-His₆ variant, and the corresponding kymograph showed that such rings were static. Contrary to what was reported by our reconstitution experiment showed static polymers, but such lack of treadmilling could be a consequence of the presence of 100% of static protein versus the mixture of static (*sZipA*) and mobile (FtsZ) proteins used by Krupka et al. [Krupka et al., 2018]. In a further attempt to recover the dynamic behaviour of the Z-rings, we decided to mix 1:1 the FtsZ-YFP-*mts*-His₆ variant (static component) with FtsZ-YFP-*mts*[FtsA-*E. coli*] (mobile component). Strikingly, we were able to recover Z-rings dynamic behaviour (**Figure 5.4B**), however we manage to capture two different dynamic rings, one that resembles the dynamic behaviour of FtsZ-YFP-*mts*[FtsA-*E. coli*] and one, with a slower rotational speed of 20 nm/s that might capture the dynamic behaviour when both proteins are combined (**Figure 5.4C**).

With this we concluded that membrane affinity and therefore, treadmilling of Z-rings can be control by the presence of static components, like in the case of the transmembranal protein ZipA.

5.2 DISCUSSION

In our minimalistic *in vitro* reconstitution study, as previously reported in Ramirez et al. [Ramirez-diaz et al., 2018], we showed that polymers of artificially membrane-targeted variants of FtsZ-YFP-*mts* autonomously and without the presence of FtsA or ZipA self-organize on a supported bilayer upon addition of GTP and Mg²⁺. A key characteristic of our *in vitro* reconstitution system is the easiness to modify different factors and to dissect the importance of each of them, here by means of point mutations, domain deletions and change of a couple of amino acids we were able to track their effect on FtsZ self-organisation and treadmilling on supported lipid membranes.

We have identified certain structural components in FtsZ required for the formation of ring-like structures with membrane binding and lateral interactions as two important factors. We showed the absence of long curved filaments on the membrane when membrane binding is impaired by means of a point mutation in the membrane-targeted sequence. Either natural anchors such as FtsA [Loose and Mitchison, 2014], as well as non-natural anchors such as an *mts* [Ramirez-diaz et al., 2018] are required for FtsZ polymers to organise and further develop into dynamic rings. We also showed that control of lateral interactions is quite important (**Figure 5.1**). In the absence of the C-terminal linker (CTL) of FtsZ, curved filamentous and discontinuous bundles were observed agreeing with published *in vitro* [Buske and Levin, 2013] and *in vivo* data [Sundararajan et al., 2015, Sundararajan et al., 2018], however we could also see the formation of small circular structures. Even

though deletion of CTL reduces GTPase activity [Sundararajan et al., 2018] (**Figure B.3**), filaments seem to be dynamic along the time.

The emergence and dynamic of these collective patterns are mediated by the intrinsic FtsZ polymerization, linked to Mg^{2+} and GTP hydrolysis. GTP hydrolysis has been shown as a key component to power treadmilling *in vitro* [Ramirez-diaz et al., 2018] and *in vivo* [Yang et al., 2017, Bisson-Filho et al., 2017], here we also showed how in an artificial system, treadmilling is affected by mutations that reduce GTP hydrolysis. On top of that, our experimental set-up allowed us to show that mutants with highly reduced GTPase activity are still able to form FtsZ-rings (**Figure 5.2**). Membrane affinity also plays a role in the dynamics of FtsZ assembly. Here we demonstrated how differences in binding affinities also affects the dynamics of the system (**Figure 5.3**). Also, that the presence of both, static and dynamic components can regulate the treadmilling behaviour of FtsZ rings. In nature, both ZipA and FtsA might regulate the rotational speed of the septal ring, in our *in vitro* system we tried to mimic the presence of both tether proteins and we observed indeed different dynamics in the system. Even though we could not reproduce the mean rotational speed reported *in vivo* [Yang et al., 2017, Bisson-Filho et al., 2017], our measurement are within the ranges.

Our approach shows that *in vitro* systems are paramount to assess phenotypes that could be deleterious *in vivo* or given the high amount of noise in biological systems, difficult to study. First, we could show that GTP-binding and GTP-hydrolysis could be partially dispensable for ring formation, but membrane binding as well as control over lateral interactions needs to be present for the formation of $\approx 1 \mu\text{m}$ diameter Z-ring (**Figure 5.1**). Membrane binding is required for the correct positioning on the membrane, and in principle, this attachment could increase the probability of FtsZ filaments to encounter each other and self-organize on the membrane. Lateral interactions of FtsZ polymers will control how FtsZ filaments interact, such repulsion between filaments could be the main factor to go from straight and amorphous filaments to curve well organize rings [Sundararajan et al., 2018]. Second, GTPase activity and strength of membrane binding influence treadmilling. At low levels of GTP-hydrolysis, filament breakage will be delayed, since monomer will stay longer in a FtsZ-GTP form (**Figure 5.5**). The presence of static components, such as a transmembrane protein as ZipA could regulate also the rotational speed of the septal ring.

Our study provides new hints on the Z-ring architecture; identifying key factors for the formation of dynamic swirls. Since our data correlates quite nicely with *in vivo* studies [Yang et al., 2017, Bisson-Filho et al., 2017], we can be confident about the type of conclusions we can drag from this *in vitro* study. Finally, one possible extrapolation of the information gathered in this work could be apply to control cell-division rate of organisms of interest where changes on GTPase activity [Bisson-Filho et al., 2017], membrane binding or the presence of static components could lead to slower or faster division rate with a possible interest in metabolic engineering.

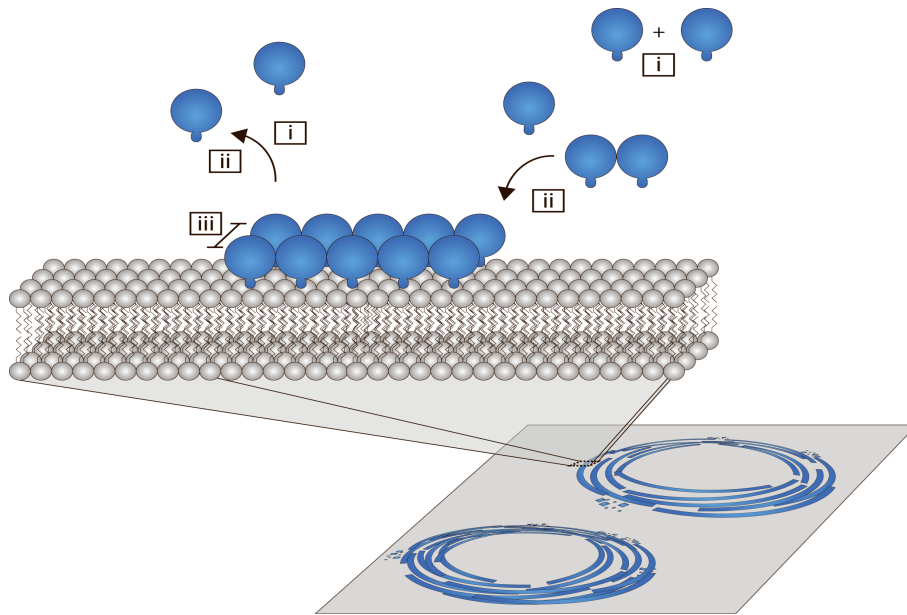


Figure 5.5: FtsZ rings are dependent on three factors: (i) membrane binding, (ii) lateral interactions and (iii) GTPase activity. FtsZ protofilaments (pfs) will form in solution and/or close to the membrane interface. Depending on the GTPase (i) activity of each monomer, filament size will be regulated. Up to a certain threshold (ii) pfs will be attracted to the membrane and the strength of membrane binding will play an important role for the self-assembly into rotating rings. However, if the control of lateral interactions is absent, as in the case of the delta-CTL, filamentous structures will be observed on the membrane. Therefore, (iii) lateral interactions regulate the correct interaction between FtsZ filaments. Lastly, treadmilling will be dictated by (i,ii) GTP-hydrolysis and secondly by membrane binding. Both factors will influence the rate of breakage and off rates between the membrane to solution. Overall, the set of factors will lead to the formation of dynamic Z-rings.

Chapter 6

Study of FtsZ chimera protein in cell-like environments

Cell-free synthetic biology has become an important technology for the reconstitution of cellular modules and even as a baseline for the generation of minimal cells. With this in mind, here we applied two different technologies to study the FtsZ chimera protein in cell-like environments with the main objective to take our system into a framework that mimics the cellular space. The first technology was a cell-free expression (CFE) system approach inside giant unilamellar vesicles to synthesized FtsZ-YFP-mts, the membrane-targeted version of FtsZ. Here first, we aimed to study how the protein behaves in a crowd environment similar to the intracellular space, and second, we aim to have a tool to encapsulate more than one protein at a time without the hurdle of protein purification and tweaking of buffer conditions. We first expressed our protein in batch and quantified the final protein concentration, later we characterized protein functionality on supported lipid bilayers and saw the formation of Z-rings and filaments. Finally, we encapsulated the reaction inside vesicles; expression was observed but protein did not self-organized into curved filaments or rings, as seen when the purified protein is encapsulated along with CFE components at initial times of the experiment. The second technology that we employed were microfluidics. In order to take our vesicles into a more native 3D shape (rod-shaped in *Escherichia coli*) and study how FtsZ behaves when we provide a container similar in shape to living cells. We implemented a microfluidics set-up to trap and deform vesicles into elongated compartments, keeping the liposome integrity along the time.

Together, this study aims to establish an approach combining different technologies to express an array of proteins and cellular modules easy to characterize and study in cell-like compartments.

6.1 RESULTS

6.1.1 The synthesized FtsZ-YFP-mts is capable to form dynamic FtsZ-rings on planar bilayers

Cell-free expression systems represent a novel method for the synthesis of proteins. There are several examples of *E. coli* proteins synthesized inside giant unilamellar vesicles, the most remarkable are the expression of MreB [Maeda et al., 2012], and most recently FtsZ-FtsA-ZipA [Furusato et al., 2018]. Following a similar approach, we decided to express FtsZ-YFP-mts in the commercially available PURExpress reaction. The batch reaction has an average yield of 200-5000 ng/ μ l [Shimizu and Ueda, 2010] and given that we required on average a concentration of 35 ng/ μ l of FtsZ-YFP-mts to observe the formation of Z-rings on SLBs, we decided to use the PURExpress reaction as our standard platform for the synthesis of FtsZ. The reaction has all the necessary components from transcription and translation to happen in a reconstituted system that uses T7 transcription and *E. coli* translation machinery. We supplemented the reaction with a pet11b-FtsZ-YFP-mts plasmid at the recommended plasmid concentration by the supplier (170 ng/ μ l). We tested two different incubation times and observed that the suggested 2-hour incubation time gave the highest final yield (**Figure 6.1**).

To further characterize the final product, we decided to test the capacity of the synthesized protein to self-organize into Z-rings on a supported lipid membrane, quite different from the biochemical characterization that was followed in Furusato et al. 2018 [Furusato et al., 2018]. We first calculated the final protein concentration in the batch reaction taking advantage of the YFP present in the chimera protein. We calculated the concentration based on the extinction coefficient of the YFP protein; approximately 1 μ M protein was obtained in the batch reaction. We decided to use 0.2 μ M in a self-organization assay, minimal concentration required for FtsZ to self-organized into dynamic rings [Ramirez-diaz et al., 2018]. After addition of the synthesized protein, 4 mM GTP and 5 mM Mg²⁺; the protein organised into Z-rings that were dynamic along time (**Figure 6.1C, yellow arrows, left panel**). We also tested self-organisation without the addition of GTP and Mg²⁺ and observed the formation of long curved filaments as well as less defined rings (**Figure 6.1, right panel**). In the second scenario, it might be that the amount of free Mg²⁺ is high, promoting bundling between the filaments that ultimately led to the formation of long and curved filaments [Ramirez-diaz et al., 2018].

We concluded that the synthesized FtsZ-YFP-mts in a PURExpress reaction was fully functional and capable to self-organize into dynamic rings. After 2 hours of incubation, and when the system has reached its limit of expression, it seems that the amount of free Mg²⁺ is > 5 mM, leading to the formation of long and curved filaments. In order to reach the \approx 1 mM free Mg²⁺ that leads to the formation of rings further addition of GTP and Mg²⁺ was required.

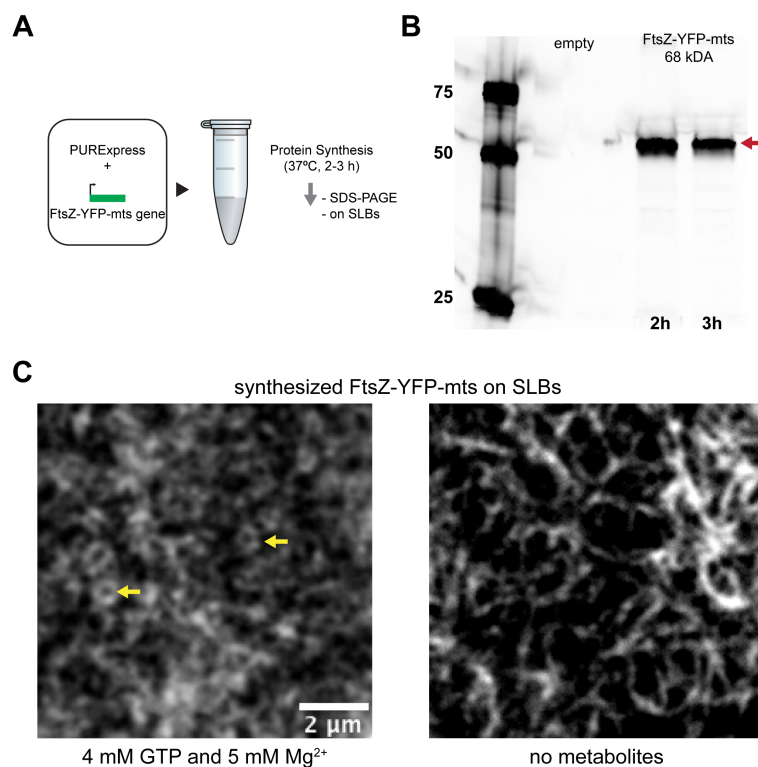


Figure 6.1: A) Schematic representation of the reaction and the following analysis. FtsZ-YFP-mts was synthesized in batch using a PURExpress reaction. 170 ng/ μ l were added in a standard 25 μ l reaction supplemented with GreenLys dye for further protein visualization on an acrylamide gel. The reaction was incubated for 2 or 3 hours at 37°C. B) 10 μ l reaction was loaded in a 4-20% acrylamide gel and run for 1 hour at 200 V. Apparent higher protein concentration was visualized after 2 hours of incubation. C) Representative snapshots of the synthesized FtsZ-YFP-mts capable to self-organize on SLB *E. coli* membranes. After 2-hour incubation, FtsZ-YFP-mts was quantified and an equivalent of 0.2 μ M protein was added on a flat supported membrane. Protein is capable to self-organize upon the addition of 4 mM GTP and 5 mM Mg²⁺ (right panel) and without the addition of further metabolites (left panel). In both cases, dynamic Z-rings are observed on the membrane after a couple of minutes of addition.

6.1.2 FtsZ-YFP-mts encapsulation in giant unilamellar vesicles: purified and synthesized protein showed different organization behaviour

After testing the functionality of the synthesized protein on planar membranes. We decided first to test the self-organization of purified FtsZ-YFP-mts in vesicles. We used an emulsion transfer method with some modifications to generate vesicles with a minimal lipid composition capable to sustain Z-ring formation (**Figure C.1**). First we encapsulated the purified protein in a buffer with a final concentration of free-Mg²⁺ of \approx 5 mM, mimicking the possible scenario after 2 hours of incubation. We observed the formation

6.1 RESULTS

of filaments in the luminal part of the vesicle as well as membrane binding (**Figure 6.2, left panel**). As a comparison and to prove that the PURExpress systems is capable to promote self-organization, we encapsulated purified FtsZ-YFP-mts in the presence of PURExpress reaction without any DNA. In this scenario, most of the protein was bound to the membrane and well-defined Z-rings were also observed along the surface (**Figure 6.2, middle panel**). Finally, in order to compare the final state of the reaction, we repeated the encapsulation of purified FtsZ-YFP-mts in PURExpress reaction and incubate 2 hours at 37°C. In this scenario, we were able to observed protein bound to the membrane and the formation of clusters, some curved filaments were also observed (**Figure 6.2, right panel**).

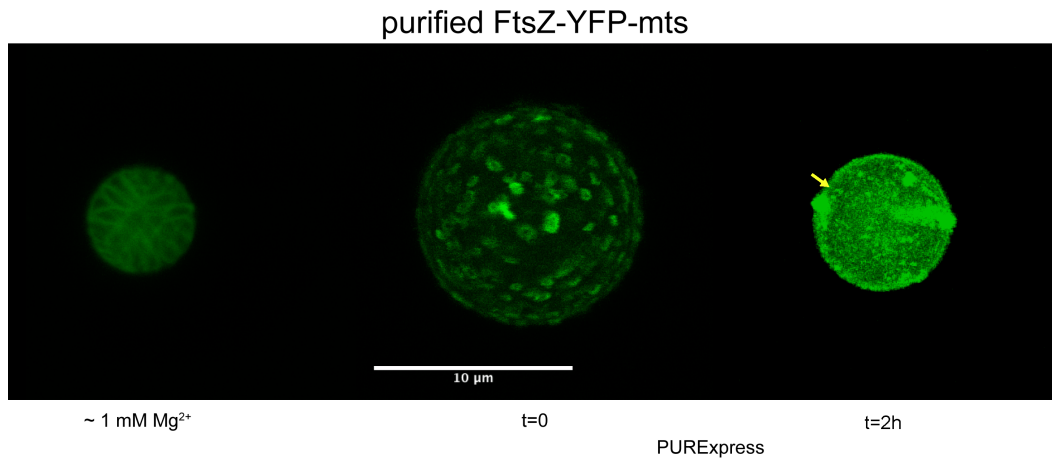


Figure 6.2: Purified FtsZ-YFP-mts (in green) can bind to the membrane and self-organised inside giant unilamellar vesicles EggPG:DOPC, 80:20 mol%. Either in the presence of buffer supplemented with GTP and Mg²⁺ (left panel) or with PURExpress reaction as a buffer (middle and right panel), the protein can bind to the membrane. However, when the purified protein is encapsulated with the PURExpress reaction as buffer and incubated for 2 h at 37°C only a couple of curved filaments were observed (yellow arrow) and protein clusters were formed along the membrane.

These steps helped us to define what to expect from a synthesized FtsZ chimera protein inside giant vesicles. In principle, after the two hours of incubation, protein clusters and a couple of curved filaments must be observed along the membrane. With this in mind, we decided to encapsulate the PURExpress reaction supplemented with 170 ng/ μ l of FtsZ-YFP-mts plasmid in giant unilamellar vesicles. After encapsulation and incubation of approximately 2 hours at 37°C, we imaged a couple of vesicles where FtsZ-YFP-mts was successfully expressed. We observed some localized points along the membrane and the formation of some sort of filaments (**Figure 6.3**). However, the protein density was less than in the case when purified protein is used.

Such filaments did not further organise into well-defined rings, as seen when purified FtsZ-YFP-mts was encapsulated and imaged after 2 hours of incubation (**Figure 6.2, right panel**). What is more, most of the expressed protein seemed to be in the luminal space rather than along the membrane, a possible explanation might be that the protein

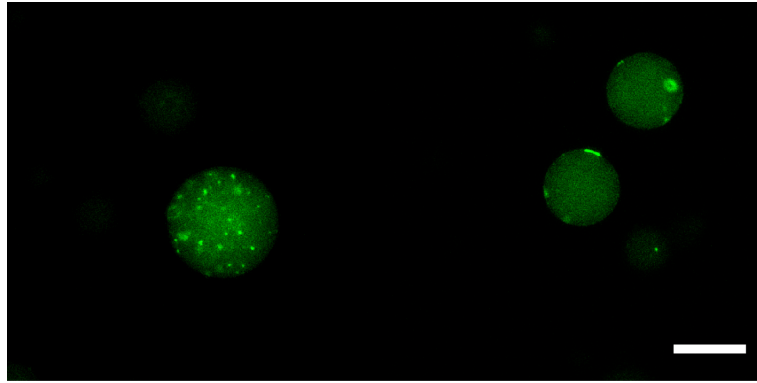


Figure 6.3: FtsZ-YFP-mts (in green) expression inside giant unilamellar vesicles EggPG:DOPC, 80:20 mol%. Cell-free expression reaction was successfully encapsulated, after a 2 hours incubation at 37°C, vesicles were imaged. However, no further organisation was observed. Most of the expressed protein seemed to be in the luminal space rather than along the membrane, a possible explanation might be that the protein is in a GDP-form due to the absence of enough GTP to further polymerise [Jiménez et al., 2011]. Also the amount of free Mg^{2+} plays an important role. Scale bar 20 μm .

is in a GDP-form due to the absence of enough GTP to further polymerise [Jiménez et al., 2011, Cabré et al., 2013]. We concluded that it might be necessary to provide external metabolites at the end of the reaction to trigger FtsZ self-organization.

6.1.3 Microfluidics traps to capture and deform spherical droplets into a cell-like shape

We decided to use microfluidics traps for two main reasons: capture and deformation of GUVs. We were first interested to immobilise vesicles in a certain position and in this way study them under different buffer conditions, in the presence of different proteins or metabolites. We decided to test the feasibility of our traps to trigger polymerization of synthesized FtsZ inside the vesicles. For this, we required the integration of pores along the membrane to ease the influx of GTP and Mg^{2+} , we decided to use α -hemolysin to generate membrane pores [Chalmeau et al., 2011, Song et al., 1996]. First we tested if the protein pore was able to bind to our lipid mixture in vesicles only containing buffer, we observed protein binding along the outer membrane that was persistent along time with a constant flow rate of 5 $\mu l/h$ (**Figure 6.4A**).

Later, we tested if there was an influx of flow inside the vesicles. We used a buffer that contained a soluble Alexa-647 dye in order to follow the intake of outer buffer along the time. We were able to measure an increase of intensity in the luminal part of the vesicle that can be translated as an intake of outer buffer due to the presence of α -hemolysin pores (**Figure 6.4B**). Our final test aimed to check the stability to such buffer exchanges in vesicles with synthesized FtsZ by the PURExpress reaction. Here, we provided α -hemolysin together with the soluble dye and some GTP and Mg^{2+} in the buffer and tracked the intake

6.1 RESULTS

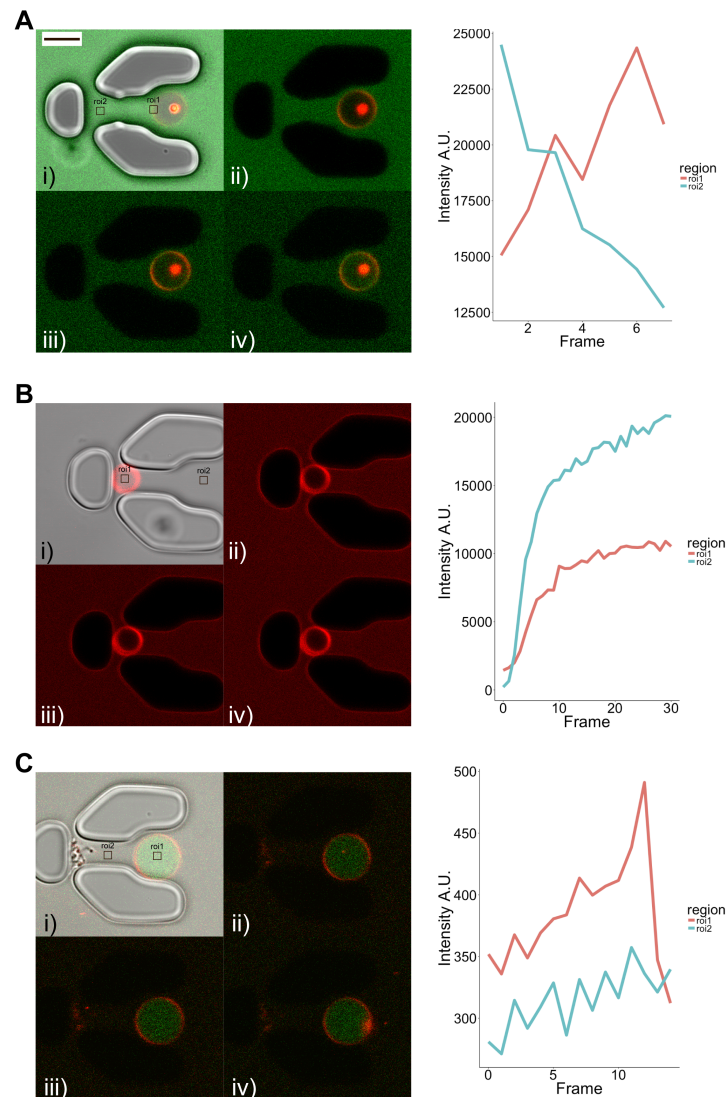


Figure 6.4: Representative snapshots of trapped vesicles under different buffer conditions. A) Buffer containing α -hemolysin-GFP. Linear plot shows the intensity measured in two different locations: roi1, along the membrane and roi2 outside the vesicle. While the amount of signal increased along the membrane, outside of the vesicle it decreased, meaning that the pore forming protein is able to bind to the membrane vesicle and stay there under a constant flux of buffer. B) Buffer containing α -hemolysin and a soluble dye Alexa-647. Linear plot shows the intake of buffer with soluble dye in the luminal part of the vesicle (roi1) C) Buffer containing α -hemolysin, soluble dye Alexa-647, GTP and Mg^{2+} tested in vesicles with synthesized FtsZ using the PURExpress reaction. Linear plot shows the intake of outer buffer as an increase in intensity in the luminal part of the vesicle. Scale bar $10 \mu\text{m}$.

to the luminal part of the vesicle, we observed an increased intensity along time, which correlates with an intake also of GTP and Mg^{2+} . Such preliminary experiment showed the feasibility to provide with metabolites to trigger synthesized FtsZ polymerization, however

6.1 RESULTS

further tests are required to find the right conditions that will lead to the formation of curved FtsZ bundles or rings, or to avoid vesicle bursting due to a abrupt change in osmolality.

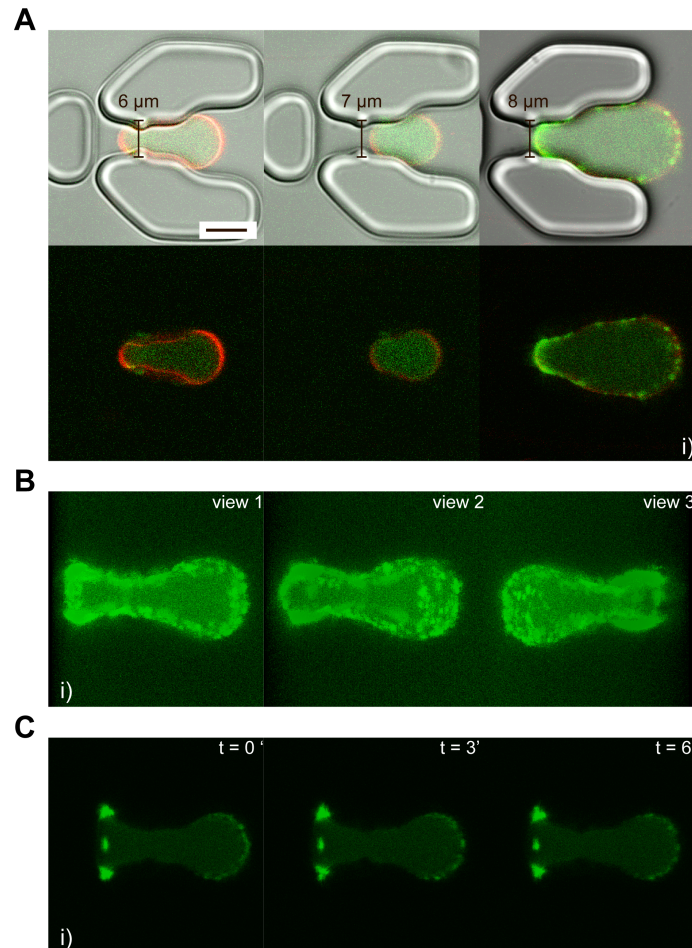


Figure 6.5: Representative snapshots of deformed vesicles using low flow rates. A) Different vesicle sizes can be trapped and deformed. B) From (A), 3D reconstitution of a vesicle deformed, purified FtsZ filaments are visible and they seem to organise in specific parts along the membrane. C) A closer look shows that FtsZ-YFP-mts polymers seem to organise along the narrowest membrane constrictions, and that such organisation is constant along time. Scale bar 10 μm .

Finally, we were interested to test vesicle deformation. For this, we decided to encapsulate purified FtsZ in buffer with ≈ 1 mM free Mg^{2+} . The design contained different deformation sizes that will deform vesicles into several elongation lengths. We observed that low flow rates (5-10 $\mu\text{l/h}$) were enough to push vesicles into an elongated shape and that the vesicles were able to stay deformed for long periods of time without collapsing or busting (**Figure 6.5A**).

Depending on the vesicle size, we were able to image purified FtsZ for different membrane shapes (**Figure 6.5B**). Strikingly, in several vesicles we captured the positioning of

FtsZ in the narrowest regions generated in our traps (**Figure 6.5C**), recapturing previous observations by Erickson et al. 2010 [Erickson et al., 2010].

The set of experiments have shown that microfluidics traps represent an attractive technology to study vesicles, allowing the exchange of different buffer conditions and deformation of vesicles into pre-defined shapes.

6.2 DISCUSSION AND OUTLOOK

We have shown the first steps to implement a cell-free approach to reconstruct cell division proteins (or any other protein) in our lab in more cell-like environments when compared to planar membranes or vesicles. Our protein of interest, FtsZ-YFP-mts was successfully synthesized using the PURExpress reaction, both in batch and when encapsulated in liposomes. Expression in batch gave a yield of $\approx 1 \mu\text{M}$ protein, fully functional and capable to self-organise into dynamic rings upon addition of GTP and Mg^{2+} , when no metabolites were supplemented the reaction by itself was still a suitable environment for the formation of long filaments on a supported membrane (**Figure 6.1**). In the encapsulation experiments we managed to encapsulate the reaction inside liposome with charged lipids, and also to get detectable expression.

A cell free expression approach has been shown to be a valuable tool that enables the expression of different proteins, overcoming the need to purify them, it represents a valuable tool for the easy characterisation of not only single proteins [Maeda et al., 2012], but also a set of proteins [Furusato et al., 2018], with the further promise to go for cellular machineries and maybe minimal cells. Here, our main objective was to reconstitute the FtsZ-ring inside vesicles. We decided to use the synthetic system (FtsZ-YFP-mts) since it reduces the number of components required to be expressed, lately, we also implemented a microfluidics set-up to trap and deform GUVs and we showed its simplicity and usability (**Figure 6.6**).

With the idea to go further in the reconstitution of a cell-division machinery, like for instance providing a regulation for the correct positioning of FtsZ filaments such as the Min system, we still have several hurdles to overcome. It seems that expression in batch does not seem to be a major problem, since we managed to produce enough protein material, fully functional in our reconstitution systems (**Figure 6.1**). However, when the reaction is encapsulated there are three aspects to take into account: 1) the final number of vesicles is low, compared when non-charged lipids are used (personal experience); 2) encapsulation is not homogeneous and only a small percentage of the vesicles will achieve a protein concentration detectable by confocal microscopy; 3) even if expression is achieved, self-organization is not guaranteed (**Figure 6.3**). To overcome vesicle yield, we could employ a different emulsion technique, for instance cDICE (continuous droplet interface crossing encapsulation), that has proved to be a powerful technology for vesicle generation [Abkarian et al., 2011]. In the case of non-homogeneous encapsulation and low expression of protein we could also try to go for expression systems with higher protein yield, like PURE 2.0 [Furusato et al., 2018] or cell-extracts [Maeda et al., 2012], with this, we will

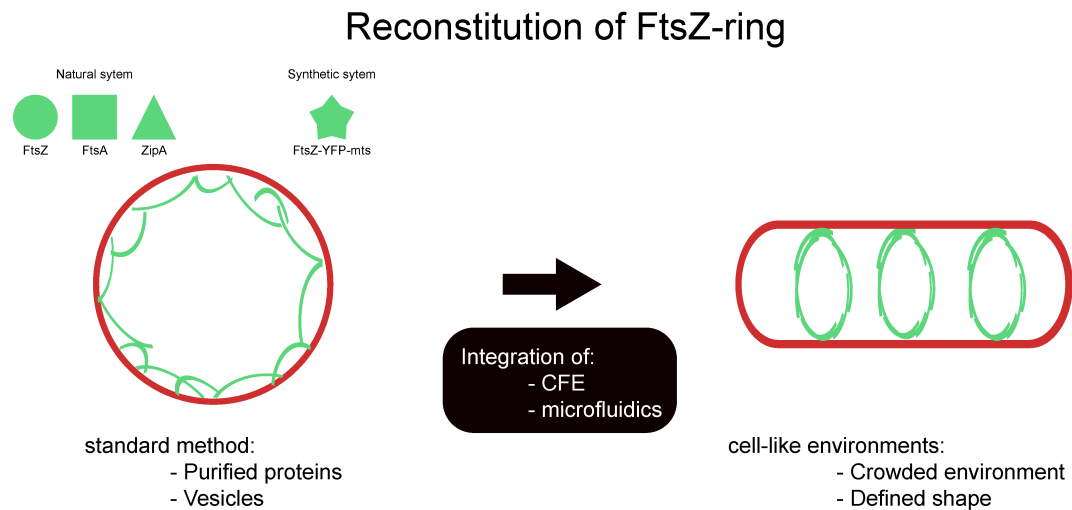


Figure 6.6: With the ultimate goal to generate a minimal cell, we need to reconstitute cellular modules one at a time. In the case of cell-division, the Z-ring can be reconstituted in *in vitro* systems using two different approaches: 1) the natural system, that requires three different proteins FtsZ, FtsA and ZipA; 2) or the synthetic system, that requires a single component FtsZ-YFP-mts. Once encapsulated and provided with the right amount of metabolites, FtsZ will polymerise into curved filaments. In a spherical container they will align along the membrane, however when a break in symmetry is provided, such filaments would tend to align along the long axis [Osawa et al., 2008]. If the proper cues are provided i.e. Min proteins, FtsZ will be localized in a specific location of the vesicle and in this way mimic what happens inside the cell

expect the number of vesicles expressing the desire protein to increase in a considerable way. Finally, while dealing with trigger of reactions inside the vesicles, in our system we came to realise that formation of filaments did not happen due to the lack of metabolites inside the vesicles. We already did some exploratory experiments that showed the feasibility to provide external metabolites, however, more tests are needed to find the right concentration of metabolites that will trigger FtsZ polymerization inside the liposomes without bursting the vesicles.

We want to highlight the importance of our microfluidic devices. In this work, we briefly showed preliminary results to trap and deform vesicles (**Figure 6.4, 6.5**). There are other options, like micropipettes or optical tweezers [Lee and Liu, 2014, Lim et al.,], however our microfluidics set-up represents a way to take this type of studies into a more high-throughput fashion. Here we can have the possibility to image more than one vesicle at a time under different conditions and shapes, in contrast when one does imaging of vesicles in an open surface where changes in buffer conditions are almost impossible as well as changes in shape. We believe that this technology will contribute to improve reproducibility in vesicle experiments and in our case, improve our studies in division proteins e.g. Min proteins or Z-ring proteins.

Microfluidics will not only be useful in a trapping and deformation step, but also in the early step of encapsulation. For example, it could be useful to encapsulate the reaction in

6.2 DISCUSSION AND OUTLOOK

a more controlled manner, or even to increase the final yield of protein inside the vesicles [Monterroso et al., 2016]. It could also be needed to screen the components in the reaction to achieve the best performance possible, here microfluidics could represent a valuable tool to implement [Genot et al., 2016, Baccouche et al., 2017].

Chapter 7

Rapid characterization of FtsZ in a droplet barcoding microfluidics system

There are many aspects in biochemical reactions that have to be considered to achieve a desired outcome. In the previous chapter, we dealt with the encapsulation of FtsZ inside GUVs either purified or synthesized. We wondered why there is such a difference, if in principle the synthesized FtsZ protein seem to be functional when produced in batch. We believe that here we are facing an optimization problem. In this chapter, we aim to implement a droplet-based prototyping for the rapid characterization of metabolites in different biochemical systems. With the use of barcoding dyes, fluorescent intensity values can be easily translated to concentrations that later can be used to understand biochemical reactions and in our case lead the way to obtain a synthesized FtsZ capable to self-organize into long and curved filaments inside cell-like vesicles.

7.1 RESULTS

7.1.1 Implementation and troubleshooting of a droplet barcoding microfluidics set-up

With the aim to rapidly characterize biochemical systems e.g. purified proteins, cell-free expression systems; we decided to implement an automated platform based on a microfluidics set-up published by Baccouche et al. 2017 (**Figure 7.1A**).

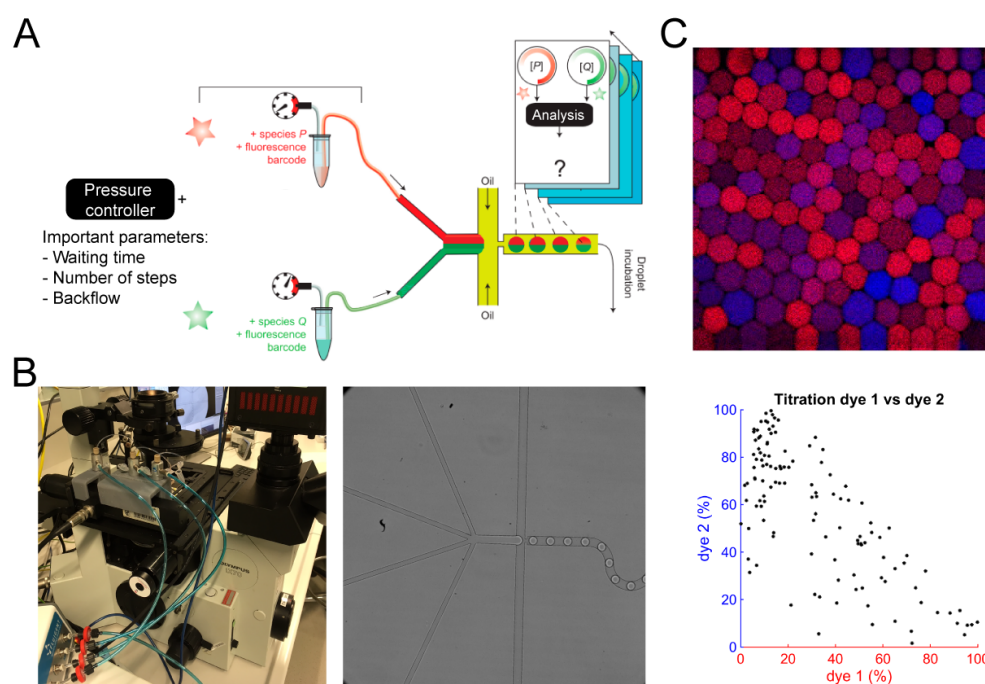


Figure 7.1: A) Schematic representation of the implemented microfluidics set-up adapted from Baccouche et al. 2017 [Baccouche et al., 2017]. The pressure control pump that dictates the titration experiment is controlled automatically with a script where user define parameters were vary the concentration of each component. The parameters that influence the most the titration performance are: waiting time between the change of pressure in each inlet, level of invasion that is translated as a backflow between the inlets, and the number of steps in the titration. B) Experimental set-up (left) and screen-shot of droplet production (right). C) Droplet barcoding experiment with default parameters. Representative snapshot of a 1D titration system with 2 dyes in blue, cascade-Blue; in red, Alexa-647. Scatter plot shows the titration of both dyes, in an ideal scenario, the scatter plot should return a linear relationship between the dyes

The set-up consists of inlets synthesized by a pressure pump. Automation is achieved through a script that will change the amount of pressure along time, titrating the different components in the reaction. Once the data has been collected, a script analysis will translate fluorescence intensity values to concentrations, taking biochemical reactions into

7.1 RESULTS

the high-throughput era, allowing to perform automatic screenings, cover a vast amount of the search space of optimal parameters in a single experiment [Baccouche et al., 2017].

We decided to first implement a 2D titration system, using two different dyes as barcodes to track the titration along time of the two inlet channels. In a first approach, we tested the pre-defined settings used by Baccouche et al. 2017 [Baccouche et al., 2017]. After analysis, a scatter plot gave us information about how reliable the translation from barcoding dyes to concentrations of metabolites of interest is. When the pressure pump script was applied, the analysis retrieved a plot where one can observe the titration of both dyes, with a negative correlation between them **Figure 7.1B**.

However, since the linear relationship between both dyes is not as linear as expected [Baccouche et al., 2017], we decided to systematically change different parameters that seemed meaningful in order to have a better titration in our system. The main parameters that we considered were: waiting time between the change of pressure in each inlet, number of steps in the titration experiment, level of backflow between channels and finally imaging laser set-up for data collection.

Regarding the waiting time, this parameter defines how much time the system will wait for the next pressure value to be applied. In principle, this parameter will lead the system to stabilise and reach the desire titration, if the waiting time is too short, it is quite likely that the titration will have some off values. The default waiting time given in the script was 1 ms, we decided to test 1 s of waiting time, and in this sense, allow the system to get more time to stabilise the change in pressure at each step. To have a better read-out of our analysis, we calculated the correlation coefficient of the data as a representation of the linear dependence of the two dyes in our experiments. Since we faced an scenario with a negative correlation coefficient i.e. a positive increase on one dye will give a negative decrease of a fixed point in the other, the closer to -1 the stronger the negative correlation. We found that a waiting time of 1 s gave a higher negative correlation coefficient in our experiments than the one obtained with 1 ms waiting time, proving that longer waiting times allow the system to reach to stable states (**Figure 7.2A**).

With a fixed waiting time of 1 s, we investigated the effect on the number of steps given in the titration experiments, in other words the number of times the system will change the pressure. We reasoned that the heavy clouds of dots around the 100% pressure of each dye (0 values), is a consequence of the number of steps given in the system. Two different scenarios were explored: 20 steps and 50 steps. In the scenario with 20 iteration steps, there are thicker clouds with a considerably high amount of points close to 0 for dye 1 and dye 2 and with a negative correlation coefficient of -0.87. When 50 iteration steps were used in the script, we still observed some clouds in the extremes, and some points that fall far from the diagonal that lead to a negative correlation coefficient of -0.81. Since the clouds around the 0 values did not really vary greatly between the two scenarios, we decided to stick to 20 steps for the titration, since it gave the lowest correlation coefficient. (**Figure 7.2B**).

Still concerned about the heavy clouds around the zero values, we wondered if this might be a problem with the backflow between the channels. So far, we have been working with a total pressure of 575 mbar out of the 600 mbar that the sum of the inlets can

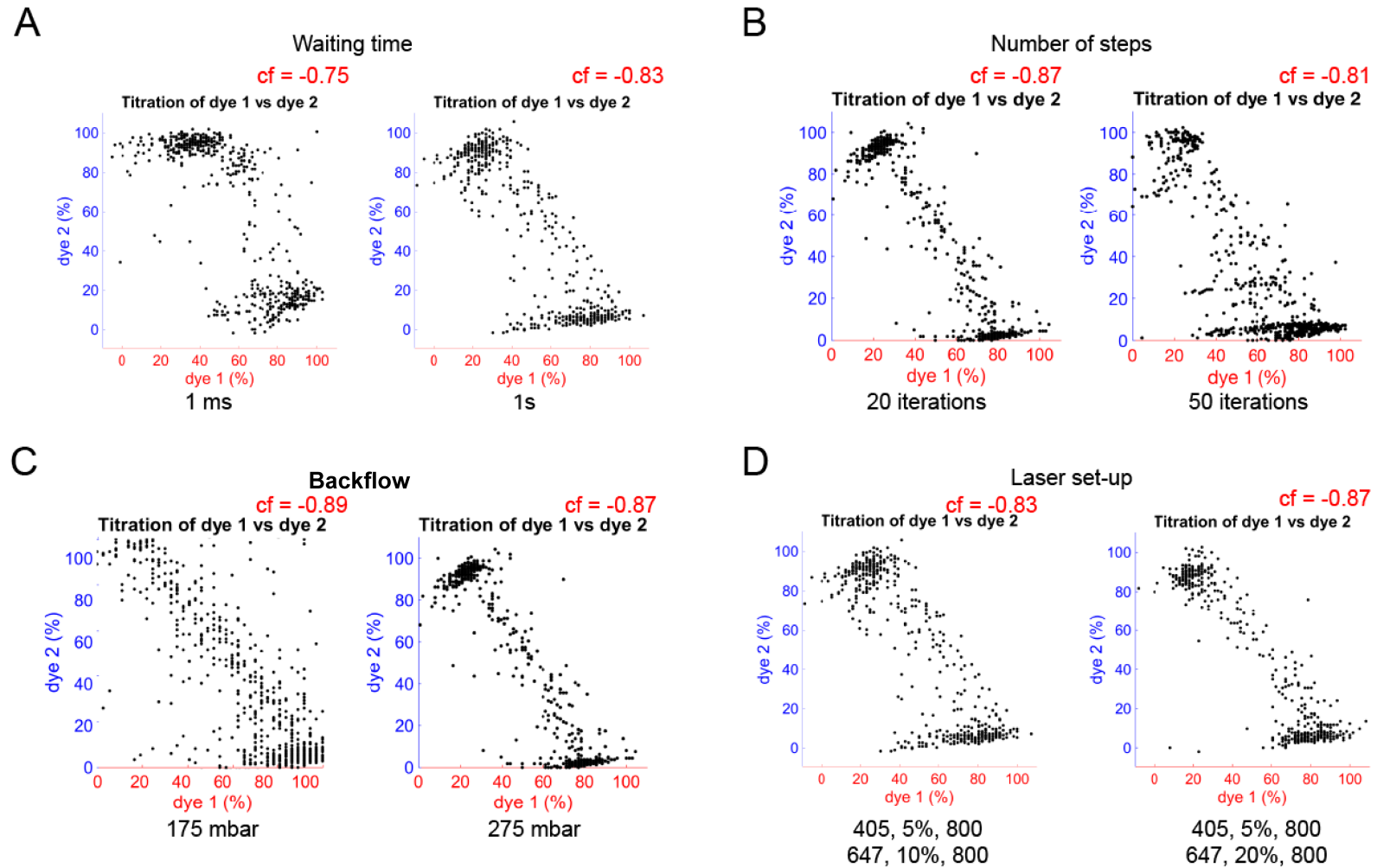


Figure 7.2: Systematic analysis of different parameters that affect the level of titration between two different dyes. A) Waiting time between the change of pressure in each inlet, B) number of steps in the titration, C) level of backflow allowed and D) imaging laser set-up for data collection.

achieve, it might be that the pressure is not stable enough and when one of the channels is 25 mbar and the other 575 mbar, the backflow does not give a reliable read-out around the 0 values. To test this hypothesis, we reduced the level maximum for a channel to 475 (**Figure 7.2C**). It seems that a pressure away from the 600 mbar maximum reduces the amount of points close to zero for each dye, decreasing also the correlation coefficient to -0.89. It could be that indeed when one of the inlets have a pressure less than 100 mbar, the backflow generated by the other inlets affect the way the dyes are mixed, and as a result, the whole titration process.

Later, we decided to analyse the effect on the linear correlation between the dyes dictated by the data acquisition. Imaging Cascade-Blue did not seem to be a problem, since low percentage of laser power was enough to detect the dye. On the other hand, the Alexa-647 dye seemed to require high laser power. We compared two different settings around the ones suggested in Baccouche et al. 2017 (**Figure 7.2D**). We concluded that the higher the laser power on the red channel, the better the image acquisition, that leads to a better read-out and a negative correlation coefficient of -0.87.

Here, we have shown a detailed troubleshooting to implement a droplet barcoding microfluidic set-up with the optimal parameters to try in the upcoming proof-of concept experiments: 1 s of waiting time, a titration with 20 steps and a maximum value of 475 mbar for an inlet. Also, the imaging conditions will be set as a starting point as 405, 5% and 647, 20% but we think these conditions might vary depending on the experiment.

7.1.2 Titration of Mg^{2+} and Ficoll for FtsZ-YFP-mts polymerization inside surfactant droplets

We first decided to test the microfluidics platform using our purified chimera protein FtsZ to promote polymerization inside surfactant droplets in the absence of any membrane. Here we set different titrations that have been tested in batch before: Mg^{2+} titration, crowding effect with a Ficoll titration and finally a mixture of both .

We used the same experimental conditions as for the vesicle experiment, using a 50 mM Tris-HCl, pH 7.5, 150 mM KCl buffer supplemented with 1.5 mM GTP and 1.5 μ M FtsZ-YFP-mts. Our first titration experiment tested the optimal Mg^{2+} concentration to generate filaments inside the droplets. Here, a range from 0 mM - 10 mM Mg^{2+} was set, with the optimal concentration > 5 mM to see any kind of filaments (as shown in our experiments on flat membranes and vesicles). However, given that in this system we do not have any membrane, polymerization does not seem to happen under the same conditions as inside vesicles (**Figure D.1**).

It is known that crowding agents can promote FtsZ polymerization in the absence of membrane recruitment [Rivas et al., 2013], with this in mind, we decided to repeat the Mg^{2+} titration using 100 g/L of Ficoll in our buffer as our crowding agent. In this set-up, we observed many droplets with FtsZ filaments in the luminal part of the droplets. We were also able to see a trend between the presence of long filaments and the Mg^{2+} , however when this trend was reported as the fluorescent intensity of FtsZ inside the droplets, the

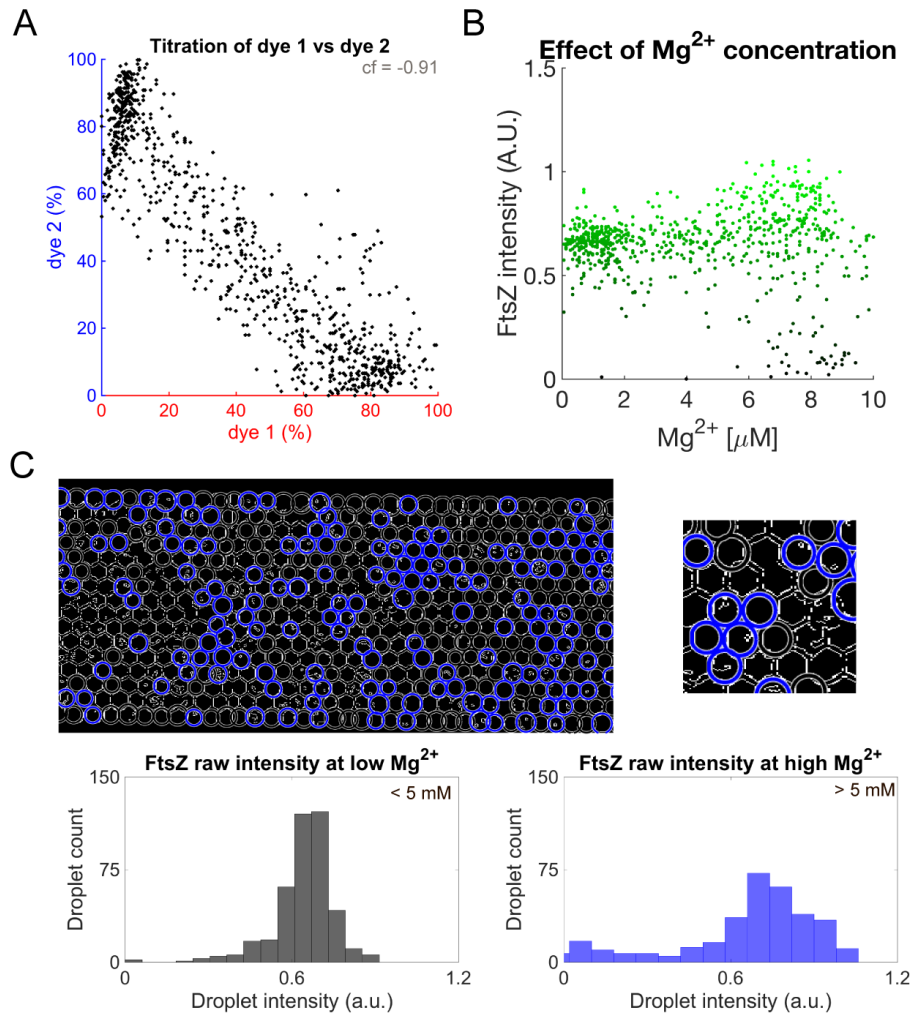


Figure 7.3: Representative experiment of FtsZ polymerization upon a Mg^{2+} titration in buffer with a total concentration of 100 g/L of Ficoll. A) Titration among the two barcode dyes with a linear correlation of -0.91. B) Titration of Mg^{2+} with different intensities of FtsZ. C) Mapping of low Mg^{2+} (black circle) and high (blue circle) concentration. There is a tendency to observe FtsZ filaments in the luminal part of the droplets with high Mg^{2+} content. Histograms show a tendency of higher intensity values for droplets where high Mg^{2+} is present.

mean value was quite similar in the presence of low (< 5 mM) or high (> 5 mM) Mg^{2+} concentration (**Figure 7.3**).

We also observed that the droplets with high Mg^{2+} were also the ones with higher intensity values (**Figure 7.3B**), however the presence of droplets with low intensity values reduced the overall mean intensity (**Figure 7.3C, right histogram**).

In a further attempt to improve the formation of FtsZ filaments inside the droplets, we carried out a Ficoll titration experiment. We decided to titrate over a range of Ficoll from 0-200 g/L keeping the Mg^{2+} concentration constant (10 mM). In this case, it was not as

7.1 RESULTS

easy to correlate the Ficoll concentration with the absence of presence of FtsZ filaments, however there is a tendency to see more filaments when the concentration of Ficoll is low (**Figure 7.4C**).

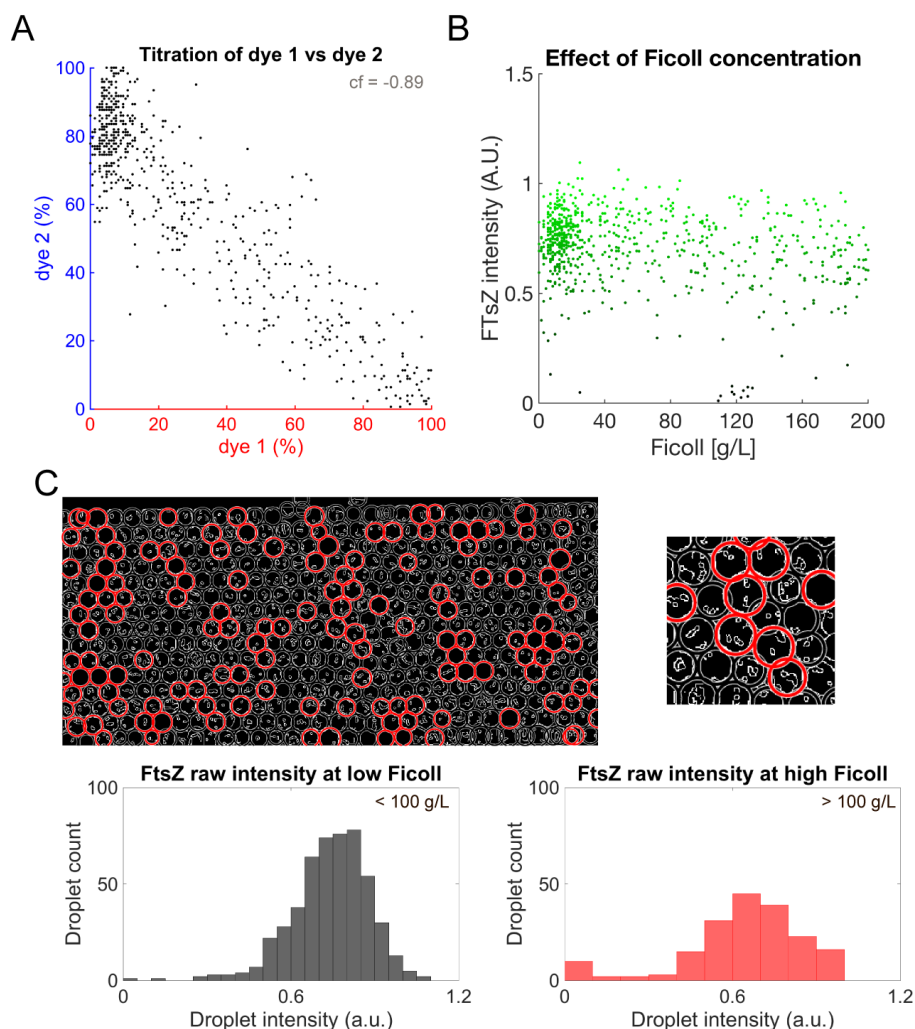


Figure 7.4: Representative experiment of FtsZ polymerization upon a Ficoll titration in buffer with a total concentration of 10 mM Mg^{2+} . A) Titration between the two barcode dyes with a linear correlation of -0.89. B) Titration of Ficoll with different intensities of FtsZ, intensity values seem to be distributed along the different Ficoll concentrations C) Mapping of Ficoll low (black circle) and high (red circle) concentration. There is no tendency to observe FtsZ filaments in the luminal part of the droplets upon Ficoll presence. Histograms show a tendency of similar intensity values for both cases, with the only difference in the number of droplet counts, but this could be an effect of less droplets with high content of Ficoll identify.

It was difficult to correlate the formation of filaments under the conditions set for the experiments.

We realised that the main reason was that polymers were not stable along time, disso-

7.1 RESULTS

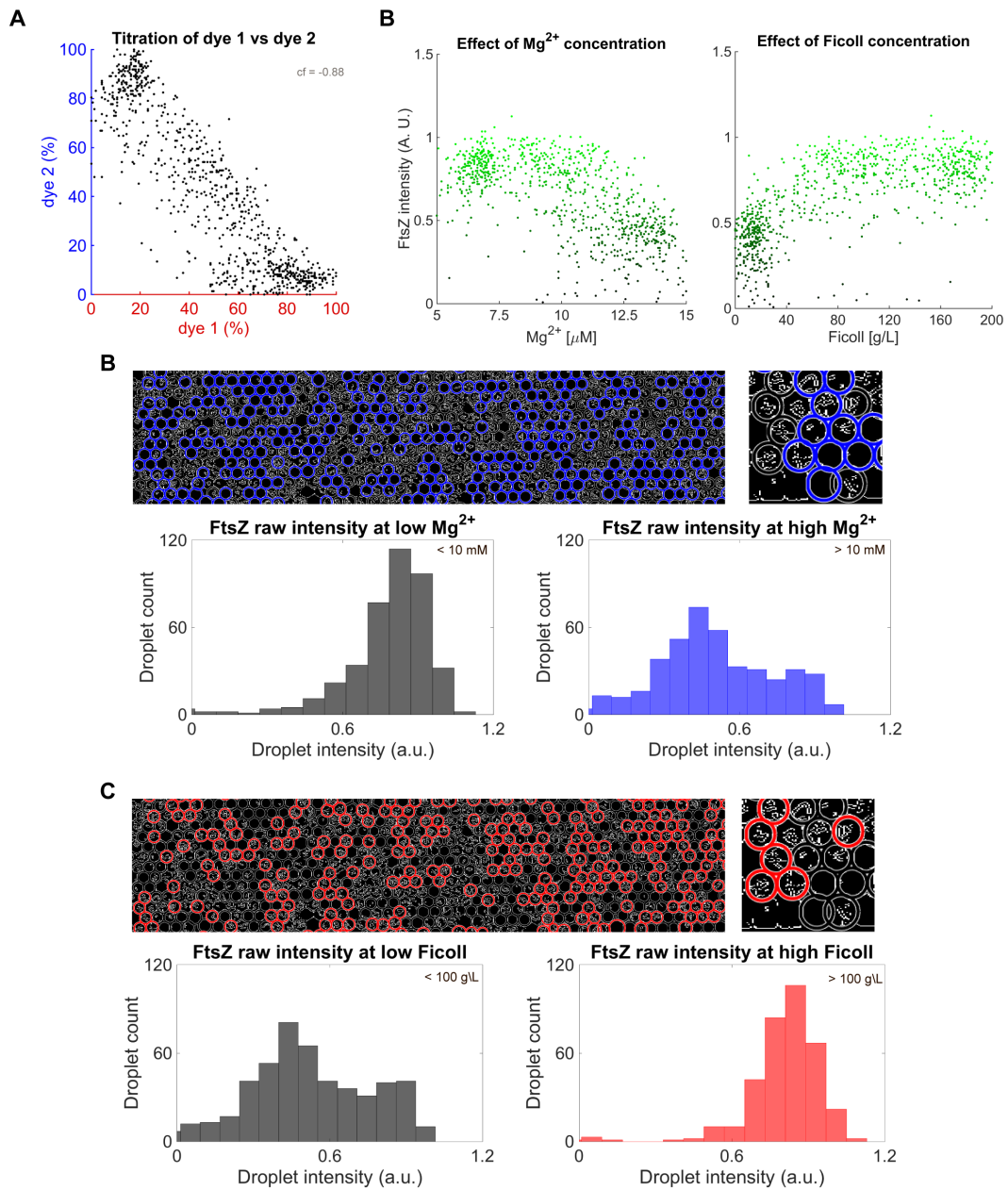


Figure 7.5: Representative experiment of FtsZ polymerization upon a Mg^{2+} and Ficoll titration . A) Titration among the two barcode dyes with a linear correlation between them. B) (left) Titration of Mg^{2+} and (right) titration of Ficoll with different intensities of FtsZ. The scatter plots already show a tendency to observed more filaments when Mg^{2+} concentration is between 5-10 mM and at the same time the Ficoll concentration is high, between 100-200 g/L C) Mapping of Mg^{2+} or Ficoll concentration: low (black circle) and high (blue or red circles respectively) concentration. There is a tendency to observe FtsZ filaments in the luminal part of the droplets with low Mg^{2+} content and high Ficoll content.

7.1 RESULTS

ciating after some time, and the higher the presence of Ficoll the less filaments observed inside the droplets (**Figure D.2**). One possible explanation is that the presence of crowding agents tends to accelerate biochemical reactions and in our case it accelerates FtsZ polymerization, depleting the amount of GTP faster. As a consequence only GDP will be available, promoting a monomeric state of FtsZ [Rivas and Minton, 2016].

We decided then to test a 2D titration to explore at which concentrations of Ficoll and Mg^{2+} we see stable filaments along the time. In this final titration experiment we explore Mg^{2+} concentration from 5-15 mM and Ficoll concentrations from 0-200 g/L (**Figure 7.4**).

It was interesting to see, that high concentration of Ficoll lead immediately to FtsZ polymers in the presence of 5 - 10 mM Mg^{2+} and a high concentration of Ficoll. On the other hand, we corroborate that high concentration of Mg^{2+} (10 - 15 mM) does not lead to filament formation when the concentration of Ficoll is less than 100 g/L. Matching quite nicely some in batch experiments (data not shown). It will be interesting to include energy regeneration systems to prolong FtsZ filaments lifetime, explore another metabolites to trigger FtsZ polymerization and also to use lipid droplets instead of surfactant droplets.

7.1.3 Titration of Mg^{2+} for optimal cell-free expression of GFP

We decided to use a more complex biochemical reaction: a cell-free expression reaction. Here, our final goal was to optimize FtsZ synthesis, using as a read-out not only FtsZ expression, but also, filament formation. Since it is well known that Mg^{2+} plays an important role in the final protein production in a CFE reaction [Jia et al., 2017], we set to titrate Mg^{2+} using as a read-out GFP expression inside surfactant droplets. In one of the inlets we supplemented the reaction with 50 mM Mg^{2+} , that after titration will give values between 0-50 mM of Mg^{2+} in the droplets.

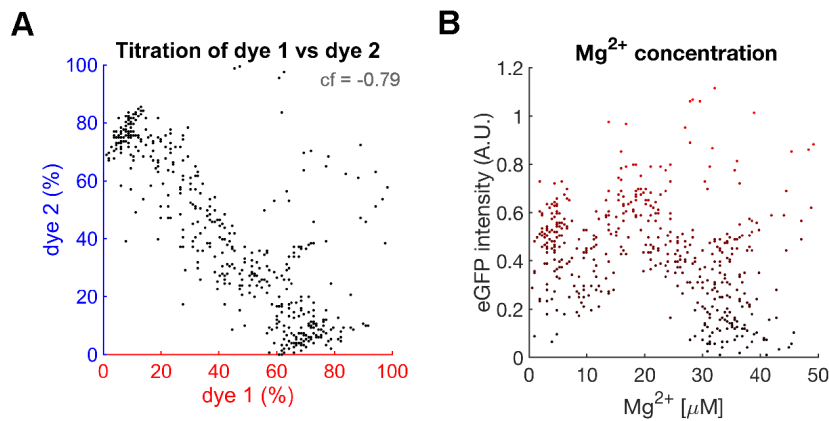


Figure 7.6: Effect of titration of Mg^{2+} in a cell-free expression reaction. Homogeneous droplets were obtained. Further analysis reveal that the concentration of each barcoding dye behaves linearly with a correlation coefficient of -0.79. Such titration can later be translated to Mg^{2+} (right scatter plot) and its direct GFP expression (right scatter plot).

We barcode each inlet again with the dyes cascade-Blue and Alexa-647. The two

7.1 RESULTS

different scatter plots showed the outcome of the titration: i) linear relationship between the two dyes with a worse negative correlation coefficient than in our experiments with FtsZ and also with more outliers and ii) the effect of Mg^{2+} titration on the level GFP expression (Figure 7.6).

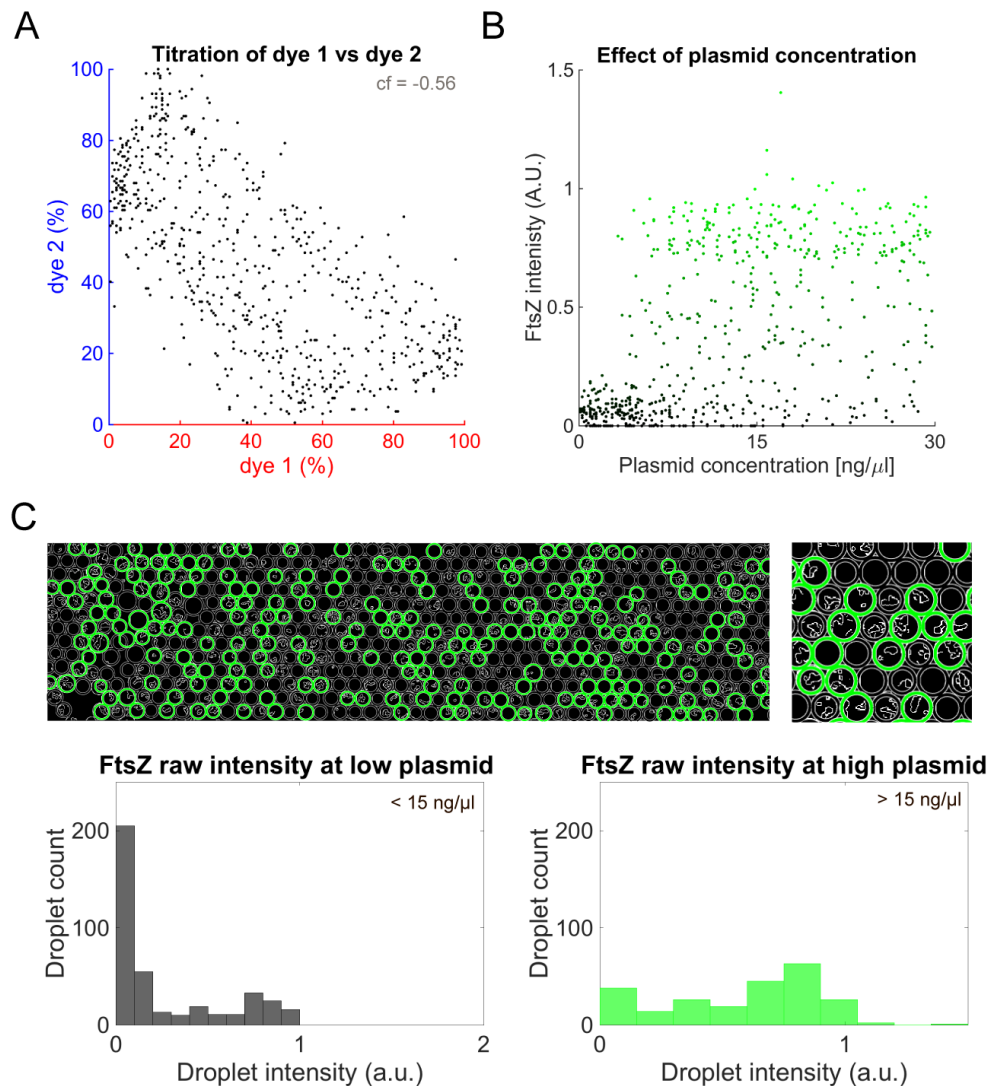


Figure 7.7: A) Effect of titration of plasmid pet11b-FtsZ-YFP-mts in a cell-free expression reaction. Homogeneous droplets were obtained. Further analysis reveal that the concentration of each barcoding dye behaves linearly with a correlation coefficient of -0.56. Such titration can later be translated to its effect on FtsZ-YFP-mts expression (B). C) Shows a trend in the amount of plasmid present in the reaction and the presence or absence of FtsZ filaments in the surfactant droplets.

The implemented experimental set-up managed to predict the optimal Mg^{2+} concentration to achieve the highest GFP-expression ($\approx 20\text{-}25 \mu M$) that correlates with batch experiments (data not shown). Based on this data, finally, we set to perform a plas-

mid titration (pet11b-FtsZ-YFP-mts) to synthesized FtsZ-YFP-mts inside the surfactant droplets, and in the based scenario, such protein should be able to polymerize. We set a plasmid titration of 0-30 ng/ μ l. Our analysis showed that titration did not follow a completely lineal relationship (as observed before in this complex biochemical mixture) (**Figure 7.7A**), however we managed to synthesize FtsZ protein able to polymerize inside the surfactant droplets.

We saw a trend between low (< 15 ng/ μ l) and high (> 15 ng/ μ l) plasmid concentration where the higher the plasmid concentration the more likely to see FtsZ filaments (**Figure 7.7B**). Since the linear correlation between the dyes was quite far from -1, the read-out of dye 1 (Dextran Alexa-647) has a lot of noise, retrieving droplets that do not match the trend i.e. low plasmid concentration, high FtsZ intensity.

We still need to improve the titration experiment, since with this complex mixture of proteins, the linear correlation is not as good as in the case where a simple mixture is used (FtsZ, Mg²⁺ or Ficoll titration). Possibly further analysis, like removal of points far away from the diagonal might improve the outcome and correlate better with experiments in batch.

7.2 DISCUSSION AND OUTLOOK

In this chapter, we have showed the first steps for the implementation of massive parallel titrations using microfluidics and barcoding dyes inside droplets. The array of possibilities is diverse as shown by our proof of concept experiments, from easy generation of phase diagrams using purified proteins and metabolites such as GTP or Mg²⁺ or optimization of cell-free expression reaction for specific proteins and systems.

In the case of purified proteins, we envision the generation of high-throughput biochemical assays and if combined with lipid-oil droplets [Monterroso et al., 2016] further reactions could be analysed. Our experiments showed the big advantage of massive experiments. We saw that 1D titration experiments did not correlate well with in batch experiments i.e. high Mg²⁺ and Ficoll concentrations are expected to generate dense FtsZ polymers. However, here, the main issue was the time between droplet generation and imaging. We know that FtsZ polymers tend to dissociate after some time, therefore a proper improvement in the experiment will be to include energy regeneration systems to keep FtsZ polymers for longer time.

There are other experiments in mind with systems that use purified proteins. For instance, it is known that Min oscillations greatly depend on the protein concentration between MinD and MinE [Loose et al., 2011], using a barcoding approach one could easily titrate over different ranges of concentrations and determine which ones lead to oscillations.

In the context of CFE reactions, there is an array of components that could be titrated to achieve maximum expression of a desired protein. As said in the previous chapter, it might be that the synthesized FtsZ does not achieve concentrations that will lead to polymerization. One could set a titration experiment against plasmid concentration that will tell us which is the range of concentrations to get the highest FtsZ concentration.

7.2 DISCUSSION AND OUTLOOK

One could also think on the use of transcription/translation activators or repressors, for instance to reconstitute a system with multiple proteins i.e. the main components of the Z-ring: FtsZ, FtsA and ZipA. It has been reported in reconstitution experiments that concentrations might matter [Loose and Mitchison, 2014], therefore by regulating protein production one might achieved the desire protein concentration. This again represents a titration experiment over a large array of concentrations.

We believe that this technology might have several applications in the upcoming future, that will ease the study of biochemical reactions in a massive fashion. It is important to notice the two major drawbacks of this set-up: 1) time between droplet generation (start of reaction) and imaging, 2) proper read-out in the experiment. However, depending the type of biochemical reaction of interest, one can find way to overcome such hurdles and exploit this technology.

Bibliography

- [Abate et al., 2010] Abate, A. R., Hung, T., Mary, P., Agresti, J. J., and Weitz, D. A. (2010). High-throughput injection with microfluidics using picoinjectors. *Proceedings of the National Academy of Sciences of the United States of America*, 107(45):19163–6.
- [Abkarian et al., 2011] Abkarian, M., Loiseau, E., and Massiera, G. (2011). Continuous droplet interface crossing encapsulation (cDICE) for high throughput monodisperse vesicle design. *Soft Matter*, 7(10):4610.
- [Anderson et al., 2004] Anderson, D. E., Gueiros-Filho, F. J., and Erickson, H. P. (2004). Assembly dynamics of FtsZ rings in *Bacillus subtilis* and *Escherichia coli* and effects of FtsZ-regulating proteins. *Journal of bacteriology*, 186(17):5775–5781.
- [Arumugam et al., 2012] Arumugam, S., Chwastek, G., Fischer-Friedrich, E., Ehrig, C., Mönch, I., and Schwille, P. (2012). Surface topology engineering of membranes for the mechanical investigation of the tubulin homologue FtsZ. *Angewandte Chemie - International Edition*, 51(47):11858–11862.
- [Arumugam et al., 2014] Arumugam, S., Petrášek, Z., and Schwille, P. (2014). MinCDE exploits the dynamic nature of FtsZ filaments for its spatial regulation. *Proceedings of the National Academy of Sciences of the United States of America*, 111(13):E1192—200.
- [Baccouche et al., 2017] Baccouche, A., Okumura, S., Sieskind, R., Henry, E., Aubert-Kato, N. e. l., Bredeche, N., Bartolo, J.-F., Taly, V., Rondelez, Y., Fujii, T., and Genot, A. J. (2017). Massively parallel and multiparameter titration of biochemical assays with droplet microfluidics. *Nature Protocols*, 12(9):1912–1932.
- [Bisson-Filho et al., 2017] Bisson-Filho, A. W., Hsu, Y.-P., Squyres, G. R., Kuru, E., Wu, F., Jukes, C., Sun, Y., Dekker, C., Holden, S., VanNieuwenhze, M. S., Brun, Y. V., and Garner, E. C. (2017). Treadmilling by FtsZ filaments drives peptidoglycan synthesis and bacterial cell division. *Science*, 355(6326):739–743.
- [Buske and Levin, 2013] Buske, P. J. and Levin, P. A. (2013). A flexible C-terminal linker is required for proper FtsZ assembly in vitro and cytokinetic ring formation in vivo. *Molecular Microbiology*.

BIBLIOGRAPHY

- [Cabr e et al., 2013] Cabr e, E. J., S anchez-Gorostiaga, A., Carrara, P., Ropero, N., Casanova, M., Palacios, P., Stano, P., Jim enez, M., Rivas, G., and Vicente, M. (2013). Bacterial division proteins FtsZ and ZipA induce vesicle shrinkage and cell membrane invagination. *Journal of Biological Chemistry*, 288(37):26625–26634.
- [Carlson et al., 2012] Carlson, E. D., Gan, R., Hodgman, C. E., and Jewett, M. C. (2012). Cell-free protein synthesis: Applications come of age. *Biotechnology Advances*, 30(5):1185–1194.
- [Chalmeau et al., 2011] Chalmeau, J., Monina, N., Shin, J., Vieu, C., and Noireaux, V. (2011). α -Hemolysin pore formation into a supported phospholipid bilayer using cell-free expression. *BBA - Biomembranes*, 1808:271–278.
- [Chen and Erickson, 2005] Chen, Y. and Erickson, H. P. (2005). Rapid *in vitro* assembly dynamics and subunit turnover of FtsZ demonstrated by fluorescence resonance energy transfer. *Journal of Biological Chemistry*, 280(23):22549–22554.
- [Chiaruttini and Roux, 2017] Chiaruttini, N. and Roux, A. (2017). Dynamic and elastic shape transitions in curved ESCRT-III filaments. *Current Opinion in Cell Biology*, 47:126–135.
- [Cho et al., 2010] Cho, N.-J., Frank, C. W., Kasemo, B., and H o k, F. (2010). Quartz crystal microbalance with dissipation monitoring of supported lipid bilayers on various substrates. *Nature Protocols*, 5(6):1096–1106.
- [den Blaauwen et al., 2017] den Blaauwen, T., Hamoen, L. W., and Levin, P. A. (2017). The divisome at 25: the road ahead. *Current opinion in microbiology*, 36:85–94.
- [Denk et al., 2016] Denk, J., Huber, L., Reithmann, E., and Frey, E. (2016). Active curved polymers form vortex patterns on membranes. *Physical Review Letters*, 116(17):178301.
- [Dewachter et al., 2018] Dewachter, L., Verstraeten, N., Fauvart, M., and Michiels, J. (2018). An integrative view of cell cycle control in *Escherichia coli*.
- [Dittrich et al., 2005] Dittrich, P. S., Jahnz, M., and Schwille, P. (2005). A new embedded process for compartmentalized cell-free protein expression and on-line detection in microfluidic devices. *ChemBiochem : a European journal of chemical biology*, 6(5):811–814.
- [Encinar et al., 2013] Encinar, M., Kralicek, A. V., Martos, A., Krupka, M., Cid, S., Alonso, A., Rico, A. I., Jim enez, M., and V elez, M. (2013). Polymorphism of FtsZ Filaments on Lipid Surfaces: Role of Monomer Orientation. *Langmuir*, 29(30):9436–9446.
- [Erickson et al., 2010] Erickson, H. P., Anderson, D. E., and Osawa, M. (2010). FtsZ in Bacterial Cytokinesis: Cytoskeleton and Force Generator All in One. *Microbiology and Molecular Biology Reviews*, 74(4):504–528.

BIBLIOGRAPHY

- [Forster and Church, 2006] Forster, A. C. and Church, G. M. (2006). Towards synthesis of a minimal cell.
- [Fu et al., 2010] Fu, G., Huang, T., Buss, J., Coltharp, C., Hensel, Z., and Xiao, J. (2010). In vivo structure of the *E. coli* FtsZ-ring revealed by photoactivated localization microscopy (PALM). *PLoS ONE*, 5(9):e12680—16.
- [Furusato et al., 2018] Furusato, T., Horie, F., Matsubayashi, H. T., Amikura, K., Kuruma, Y., and Ueda, T. (2018). *De Novo* Synthesis of Basal Bacterial Cell Division Proteins FtsZ, FtsA, and ZipA Inside Giant Vesicles. *ACS Synthetic Biology*, page acssynbio.7b00350.
- [Genot et al., 2016] Genot, A. J., Baccouche, A., Sieskind, R., Aubert-Kato, N., Bredeche, N., Bartolo, J. F., Taly, V., Fujii, T., and Rondelez, Y. (2016). High-resolution mapping of bifurcations in nonlinear biochemical circuits. *Nature Chemistry*, 8(8):760–767.
- [González et al., 2003] González, J. M., Jiménez, M., Vélez, M., Mingorance, J., Andreu, J. M., Vicente, M., and Rivas, G. (2003). Essential cell division protein FtsZ assembles into one monomer-thick ribbons under conditions resembling the crowded intracellular environment. *Journal of Biological Chemistry*, 278(39):37664–37671.
- [González de Prado Salas et al., 2014] González de Prado Salas, P., Hörger, I., Martín-García, F., Mendieta, J., Alonso, Á., Encinar, M., Gómez-Puertas, P., Vélez, M., and Tarazona, P. (2014). Torsion and curvature of FtsZ filaments. *Soft Matter*, 10(12):1977.
- [Haeusser and Margolin, 2016] Haeusser, D. P. and Margolin, W. (2016). Splitsville: Structural and functional insights into the dynamic bacterial Z ring. *Nature Reviews Microbiology*, 14(5):305–319.
- [Holden, 2018] Holden, S. (2018). Probing the mechanistic principles of bacterial cell division with super-resolution microscopy. *Current opinion in microbiology*, 43:84–91.
- [Holden et al., 2014] Holden, S. J., Pengo, T., Meibom, K. L., Fernandez Fernandez, C., Collier, J., and Manley, S. (2014). High throughput 3D super-resolution microscopy reveals *Caulobacter crescentus* in vivo Z-ring organization. *Proceedings of the National Academy of Sciences*, 111(12):4566–4571.
- [Huang et al., 2013] Huang, K. H., Durand-Heredia, J., and Janakiraman, A. (2013). FtsZ ring stability: Of bundles, tubules, crosslinks, and curves. *Journal of Bacteriology*, 195(9):1859–1868.
- [Huecas and Andreu, 2004] Huecas, S. and Andreu, J. M. (2004). Polymerization of nucleotide-free, GDP- and GTP-bound cell division protein FtsZ: GDP makes the difference. *FEBS Letters*, 569(1-3):43–48.

BIBLIOGRAPHY

- [Jia et al., 2017] Jia, H., Heymann, M., Bernhard, F., Schwille, P., and Kai, L. (2017). Cell-free protein synthesis in micro compartments: building a minimal cell from biobricks. *New Biotechnology*, 39:199–205.
- [Jiménez et al., 2011] Jiménez, M., Martos, A., Vicente, M., and Rivas, G. (2011). Reconstitution and organization of Escherichia coli proto-ring elements (FtsZ and FtsA) inside giant unilamellar vesicles obtained from bacterial inner membranes. *Journal of Biological Chemistry*, 286(13):11236–11241.
- [Keller et al., 2013] Keller, H., Worch, R., and Schwille, P. (2013). Model Membrane Systems. pages 417–438. Humana Press, Totowa, NJ.
- [Kretschmer and Schwille, 2016] Kretschmer, S. and Schwille, P. (2016). Pattern formation on membranes and its role in bacterial cell division.
- [Krupka et al., 2018] Krupka, M., Sobrinos-Sanguino, M., Jiménez, M., Rivas, G., and Margolin, W. (2018). Escherichia coli ZipA Organizes FtsZ Polymers into Dynamic Ring-Like Protofilament Structures. *mBio*, 9(3):e01008–18.
- [Lee and Liu, 2014] Lee, L. M. and Liu, A. P. (2014). The Application of Micropipette Aspiration in Molecular Mechanics of Single Cells.
- [Li et al., 2017] Li, J., Haas, W., Jackson, K., Kuru, E., Jewett, M. C., Fan, Z. H., Gygi, S., and Church, G. M. (2017). Cogenerating Synthetic Parts toward a Self-Replicating System. *ACS Synthetic Biology*, 6(7):1327–1336.
- [Lim et al.,] Lim, C. T., Dao, M., Suresh, S., Sow, C. H., and Chew, K. T. Large deformation of living cells using laser traps.
- [Lindas et al., 2008] Lindas, A.-C., Karlsson, E. A., Lindgren, M. T., Etema, T. J. G., and Bernander, R. (2008). A unique cell division machinery in the Archaea. *Proceedings of the National Academy of Sciences*.
- [Loose et al., 2011] Loose, M., Fischer-Friedrich, E., Herold, C., Kruse, K., and Schwille, P. (2011). Min protein patterns emerge from rapid rebinding and membrane interaction of MinE. *Nature Structural & Molecular Biology*, 18(5):577–583.
- [Loose and Mitchison, 2014] Loose, M. and Mitchison, T. J. (2014). The bacterial cell division proteins FtsA and FtsZ self-organize into dynamic cytoskeletal patterns. *Nature cell biology*, 16(1):38–46.
- [Loose and Schwille, 2009] Loose, M. and Schwille, P. (2009). Biomimetic membrane systems to study cellular organization. *Journal of Structural Biology*.
- [Lu et al., 2000] Lu, C., Reedy, M., and Erickson, H. P. (2000). Straight and curved conformations of FtsZ are regulated by GTP hydrolysis. *Journal of bacteriology*, 182(1):164–170.

BIBLIOGRAPHY

- [Lutkenhaus et al., 2012] Lutkenhaus, J., Pichoff, S., and Du, S. (2012). Bacterial cytokinesis: From Z ring to divisome.
- [Maeda et al., 2012] Maeda, Y. T., Nakadai, T., Shin, J., Uryu, K., Noireaux, V., and Libchaber, A. (2012). Assembly of MreB filaments on liposome membranes: A synthetic biology approach. *ACS Synthetic Biology*, 1(2):53–59.
- [Margolin, 2005] Margolin, W. (2005). FtsZ and the division of prokaryotic cells and organelles.
- [Martos et al., 2015] Martos, A., Raso, A., Jiménez, M., Petrášek, Z., Rivas, G., and Schwille, P. (2015). FtsZ Polymers Tethered to the Membrane by ZipA Are Susceptible to Spatial Regulation by Min Waves. *Biophysical Journal*, 108(9):2371–2383.
- [Mateos-Gil et al., 2012a] Mateos-Gil, P., Márquez, I., López-Navajas, P., Jiménez, M., Vicente, M., Mingorance, J., Rivas, G., and Vélez, M. (2012a). FtsZ polymers bound to lipid bilayers through ZipA form dynamic two dimensional networks. *Biochimica et Biophysica Acta - Biomembranes*, 1818(3):806–813.
- [Mateos-Gil et al., 2012b] Mateos-Gil, P., Paez, A., Hörger, I., Rivas, G., Vicente, M., Tarazona, P., and Vélez, M. (2012b). Depolymerization dynamics of individual filaments of bacterial cytoskeletal protein FtsZ. *Proceedings of the National Academy of Sciences of the United States of America*, 109(21):8133–8138.
- [Maupin-Furlow et al., 2015] Maupin-Furlow, J. A., Dajkovic, A., Erickson, H., De Boer, P. A., Männik, J., and Bailey, M. W. (2015). Spatial coordination between chromosomes and cell division proteins in *Escherichia coli*.
- [Meier and Goley, 2014] Meier, E. L. and Goley, E. D. (2014). Form and function of the bacterial cytokinetic ring.
- [Menéndez et al., 1998] Menéndez, M., Rivas, G., Diaz, J. F., and Andreu, J. M. (1998). Control of the structural stability of the tubulin dimer by one high affinity bound magnesium ion at nucleotide N-site. *Journal of Biological Chemistry*, 273(1):167–176.
- [Mingorance et al., 2010] Mingorance, J., Rivas, G., Vélez, M., Gómez-Puertas, P., and Vicente, M. (2010). Strong FtsZ is with the force: mechanisms to constrict bacteria. *Trends in microbiology*, 18(8):348–356.
- [Mingorance et al., 2005] Mingorance, J., Tadros, M., Vicente, M., González, J. M., Rivas, G., and Vélez, M. (2005). Visualization of single *Escherichia coli* FtsZ filament dynamics with atomic force microscopy. *Journal of Biological Chemistry*, 280(21):20909–20914.
- [Monteiro et al., 2018] Monteiro, J. M., Pereira, A. R., Reichmann, N. T., Saraiva, B. M., Fernandes, P. B., Veiga, H., Tavares, A. C., Santos, M., Ferreira, M. T., Macário, V.,

BIBLIOGRAPHY

- VanNieuwenhze, M. S., Filipe, S. R., and Pinho, M. G. (2018). Peptidoglycan synthesis drives an FtsZ-treadmilling-independent step of cytokinesis. *Nature*.
- [Monterroso et al., 2013] Monterroso, B., Alfonso, C., Zorrilla, S., and Rivas, G. (2013). Combined analytical ultracentrifugation, light scattering and fluorescence spectroscopy studies on the functional associations of the bacterial division FtsZ protein. *Methods*, 59(3):349–362.
- [Monterroso et al., 2016] Monterroso, B., Zorrilla, S., Sobrinos-Sanguino, M., Keating, C. D., and Rivas, G. (2016). Microenvironments created by liquid-liquid phase transition control the dynamic distribution of bacterial division FtsZ protein. *Scientific Reports*, pages 1–13.
- [Mukherjee and Lutkenhaus, 1994] Mukherjee, A. and Lutkenhaus, J. (1994). Guanine nucleotide-dependent assembly of FtsZ into filaments. *Journal of bacteriology*, 176(9):2754–2758.
- [Niu and Yu, 2008] Niu, L. and Yu, J. (2008). Investigating intracellular dynamics of FtsZ cytoskeleton with photoactivation single-molecule tracking. *Biophysical Journal*, 95(4):2009–2016.
- [Ohashi et al., 2002] Ohashi, T., Hale, C. A., de Boer, P. A. J., and Erickson, H. P. (2002). Structural evidence that the P/Q domain of ZipA is an unstructured, flexible tether between the membrane and the C-terminal FtsZ-binding domain. *Journal of bacteriology*, 184(15):4313–4315.
- [Osawa et al., 2008] Osawa, M., Anderson, D. E., and Erickson, H. P. (2008). Reconstitution of contractile FtsZ rings in liposomes. *Science*, 320(5877):792–4.
- [Osawa et al., 2009] Osawa, M., Anderson, D. E., and Erickson, H. P. (2009). Curved FtsZ protofilaments generate bending forces on liposome membranes. *The EMBO Journal*, 28(22):3476–3484.
- [Pautot et al., 2003] Pautot, S., Frisken, B. J., and Weitz, D. A. (2003). Production of Unilamellar Vesicles Using an Inverted Emulsion.
- [Pichoff and Lutkenhaus, 2005] Pichoff, S. and Lutkenhaus, J. (2005). Tethering the Z ring to the membrane through a conserved membrane targeting sequence in FtsA. *Molecular microbiology*, 55(6):1722–1734.
- [Pontani et al., 2009] Pontani, L. L., Van Der Gucht, J., Salbreux, G., Heuvingh, J., Joanny, J. F., and Sykes, C. (2009). Reconstitution of an actin cortex inside a liposome. *Biophysical Journal*.
- [Ramirez-diaz et al., 2018] Ramirez-diaz, D. A., Garcia-Soriano, D. A., Raso, A., Mücksch, J., Feingold, M., Rivas, G., and Schwille, P. (2018). Treadmilling analysis reveals new insights into dynamic FtsZ ring architecture. *PLoS Biology*.

BIBLIOGRAPHY

- [Renner and Weibel, 2012] Renner, L. D. and Weibel, D. B. (2012). MinD and MinE interact with anionic phospholipids and regulate division plane formation in *Escherichia coli*. *Journal of Biological Chemistry*, 287(46):38835–38844.
- [Rico et al., 2013] Rico, A. I., Krupka, M., and Vicente, M. (2013). In the beginning, *Escherichia coli* assembled the proto-ring: An initial phase of division. *Journal of Biological Chemistry*, 288(29):20830–20836.
- [Rivas et al., 2013] Rivas, G., Alfonso, C., Jiménez, M., Monterroso, B., and Zorrilla, S. (2013). Macromolecular interactions of the bacterial division FtsZ protein: from quantitative biochemistry and crowding to reconstructing minimal divisomes in the test tube. *Biophysical Reviews*, 5(2):63–77.
- [Rivas and Minton, 2016] Rivas, G. and Minton, A. P. (2016). Macromolecular Crowding In Vitro, In Vivo, and In Between. *Trends in Biochemical Sciences*, 41:970–981.
- [Robinson et al., 2013] Robinson, T., Kuhn, P., Eyer, K., and Dittrich, P. S. (2013). Microfluidic trapping of giant unilamellar vesicles to study transport through a membrane pore. *Citation: Biomicrofluidics*, 7:44105.
- [Robinson et al., 2014] Robinson, T., Verboket, P. E., Eyer, K., and Dittrich, P. S. (2014). Controllable electrofusion of lipid vesicles: initiation and analysis of reactions within biomimetic containers. *Lab on a Chip*, 14(15):2852.
- [Romberg and Levin, 2003] Romberg, L. and Levin, P. A. (2003). Assembly Dynamics of the Bacterial Cell Division Protein FtsZ: Poised at the Edge of Stability. *Annual Review of Microbiology*.
- [Samson et al., 2008] Samson, R. Y., Obita, T., Freund, S. M., Williams, R. L., and Bell, S. D. (2008). A role for the ESCRT system in cell division in archaea. *Science*.
- [Shimizu and Ueda, 2010] Shimizu, Y. and Ueda, T. (2010). PURE Technology. pages 11–21. Humana Press.
- [Söderström et al., 2016] Söderström, B., Mirzadeh, K., Toddo, S., von Heijne, G., Skoglund, U., and Daley, D. O. (2016). Coordinated disassembly of the divisome complex in *Escherichia coli*. *Molecular microbiology*, 101(3):425–438.
- [Söderström et al., 2014] Söderström, B., Skoog, K., Blom, H., Weiss, D. S., von Heijne, G., and Daley, D. O. (2014). Disassembly of the divisome in *Escherichia coli*: Evidence that FtsZ dissociates before compartmentalization. *Molecular Microbiology*.
- [Song et al., 1996] Song, L., Hobaugh, M. R., Shustak, C., Cheley, S., Bayley, H., and Gouaux, J. E. (1996). Structure of staphylococcal α -hemolysin, a heptameric transmembrane pore. *Science*, 274(5294):1859–1865.

BIBLIOGRAPHY

- [Stricker and Erickson, 2003] Stricker, J. and Erickson, H. P. (2003). In vivo characterization of *Escherichia coli* *ftsZ* mutants: effects on Z-ring structure and function. *Journal of bacteriology*, 185(16):4796–4805.
- [Sundararajan et al., 2015] Sundararajan, K., Miguel, A., Desmarais, S. M., Meier, E. L., Huang, K. C., and Goley, E. D. (2015). The bacterial tubulin FtsZ requires its intrinsically disordered linker to direct robust cell wall construction. *Nature Communications*, pages 1–14.
- [Sundararajan et al., 2018] Sundararajan, K., Vecchiarelli, A. G., Mizuuchi, K., and Goley, E. (2018). Species- and C-terminal linker-dependent variations in the dynamic behavior of FtsZ on membranes in vitro. *bioRxiv*, pages 1–39.
- [Szeto et al., 2002] Szeto, T. H., Rowland, S. L., Rothfield, L. I., and King, G. F. (2002). Membrane localization of MinD is mediated by a C-terminal motif that is conserved across eubacteria, archaea, and chloroplasts. *Proceedings of the National Academy of Sciences of the United States of America*, 99(24):15693–15698.
- [Teh et al., 2008] Teh, S.-Y., Lin, R., Hung, L.-H., and Lee, A. P. (2008). Droplet microfluidics. *Lab on a Chip*.
- [Thanedar and Margolin, 2004] Thanedar, S. and Margolin, W. (2004). FtsZ exhibits rapid movement and oscillation waves in Helix-like patterns in *Escherichia coli*. *Current Biology*.
- [Theberge et al., 2010] Theberge, A. B., Courtois, F., Schaerli, Y., Fischlechner, M., Abell, C., Hollfelder, F., and Huck, W. T. (2010). Microdroplets in microfluidics: An evolving platform for discoveries in chemistry and biology. *Angewandte Chemie - International Edition*, 49(34):5846–5868.
- [Vyawahare et al., 2010] Vyawahare, S., Griffiths, A. D., and Merten, C. A. (2010). Miniaturization and Parallelization of Biological and Chemical Assays in Microfluidic Devices. *Chemistry & Biology*, 17(10):1052–1065.
- [Wagstaff et al., 2017] Wagstaff, J. M., Tsim, M., Oliva, M. A., García-Sánchez, A., Kureisaite-Ciziene, D., Andreu, J. M., and Löwe, J. (2017). A polymerization-associated structural switch in *ftsZ* that enables treadmilling of model filaments. *mBio*, 8(3):1–16.
- [Weimann et al., 2013] Weimann, L., Ganzinger, K. A., McColl, J., Irvine, K. L., Davis, S. J., Gay, N. J., Bryant, C. E., and Klenerman, D. (2013). A quantitative comparison of single-dye tracking analysis tools using Monte Carlo simulations. *PLoS ONE*, 8(5):e64287—.
- [Weiss, 2004] Weiss, D. S. (2004). Bacterial cell division and the septal ring. *Molecular Microbiology*, 54(3):588–597.

BIBLIOGRAPHY

- [Williams, 2013] Williams, M. A. (2013). Protein–Ligand Interactions: Fundamentals. pages 3–34.
- [Yang et al., 2017] Yang, X., Lyu, Z., Miguel, A., McQuillen, R., Huang, K. C., and Xiao, J. (2017). GTPase activity-coupled treadmilling of the bacterial tubulin FtsZ organizes septal cell wall synthesis. *Science*, 355(6326):744–747.
- [Zemella et al., 2015] Zemella, A., Thoring, L., Hoffmeister, C., and Kubick, S. (2015). Cell-Free Protein Synthesis: Pros and Cons of Prokaryotic and Eukaryotic Systems. *Chembiochem : a European journal of chemical biology*, pages n/a—n/a.

Appendix A

Appendix to chapter IV

A.1 Figures

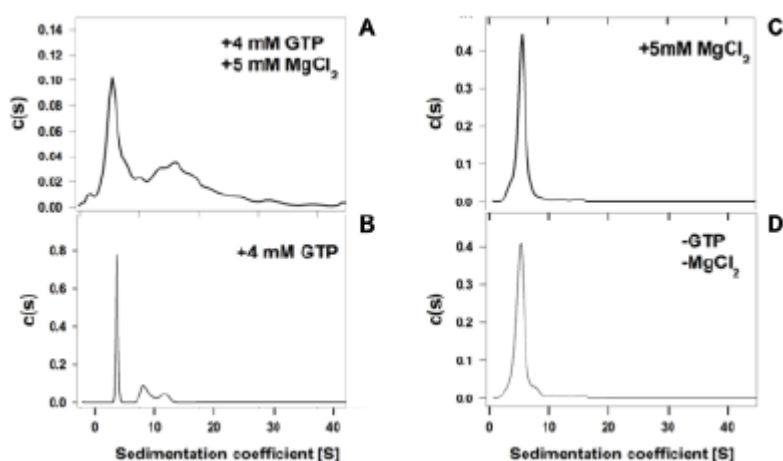


Figure A.1: $c(S)$ sedimentation coefficient distributions obtained for the chimeric FtsZ variant ($7 \mu\text{M}$) obtained from experiments conducting in working buffer. These experiments show that FtsZ-YFP-mts is a well-behaved self-associating protein: In the absence of GTP and/or Mg^{2+} (B-D) the protein exists mainly as a slowly sedimenting species with s-value of around 6S (C-D), compatible with the heterodimeric FtsZ-YFG form. In the presence of both GTP and Mg^{2+} (A) most of the protein (70%) sediments as a polydisperse mixture of higher orders species with an average s-value of 20 ± 5 S. These results are important because they allowed to control the association state of the membrane-targeted FtsZ variant by GTP and Mg^{2+} , which was crucial to obtain the reproducible dynamic ring-like structures on the bilayers shown in this work (see main text). The broad distribution of higher order species shown in (A) contrast to the sharp s-values observed in previous studies from the Rivas lab under specific experimental conditions of protein and buffer composition [Rivas et al., 2013].

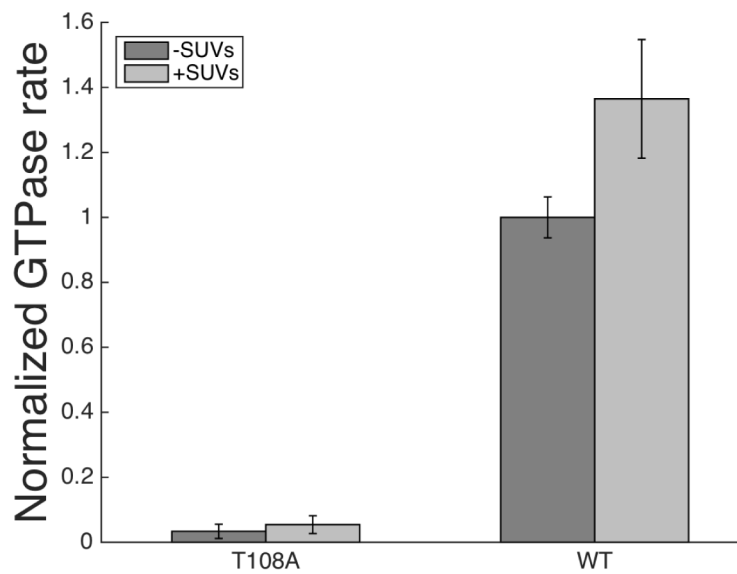


Figure A.2: GTPase activity of FtsZ-YFP-mts ($5 \mu\text{M}$) or FtsZ*[T108A]-YFP-mts ($5 \mu\text{M}$) in the absence or presence of phospholipids (4 mg/ml). The corresponding rates were normalized to the GTP activity of FtsZ-YFP-mts in the absence of phospholipids. We observed that the GTPase activity of FtsZ*[T108A]-YFP-mts was almost zero. GTPase activities were determined using the BIOMOL GRENN assay (Enzo). Error bars correspond to s.d. from three different experiments

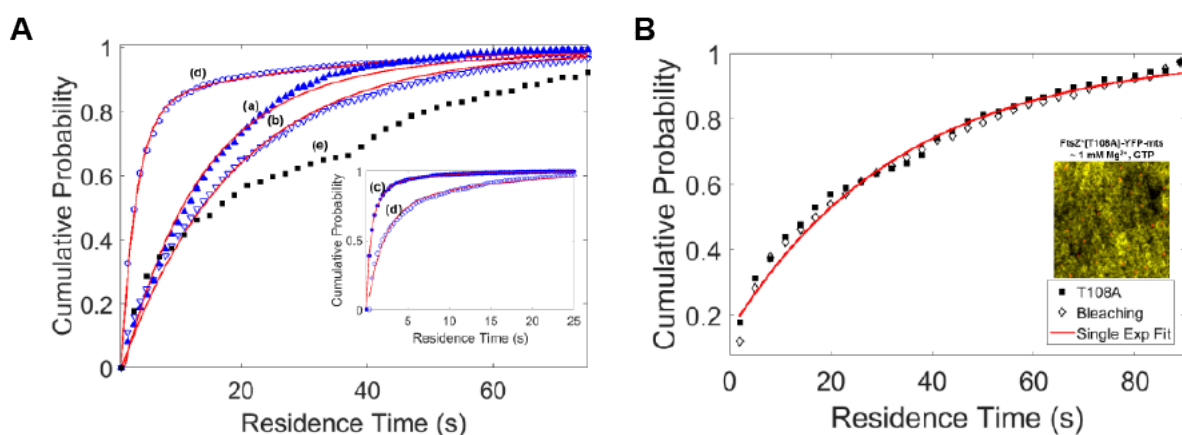


Figure A.3: (A) Cumulative probability of the residence time distributions for (a) 4 mM GTP 1mM free Mg^{2+} and (b) 0.04 mM GTP 1 mM free Mg^{2+} having an acquisition rate (1fps). Inset: Cumulative residence time distribution for GDP forms with a faster acquisition rate (3fps) at (c) 1 mM free Mg^{2+} and (d) 5 mM free Mg^{2+} . Note that the residence time distributions for GDP - 5 mM Mg^{2+} (blue circles) are equivalent at 1fps or 3fps. (e) Represents photobleaching decay. Curves were fitted to a double exponential function to calculate the mean residence time having a constant photo-bleaching contribution. Further details are under “Materials and Methods”. (B) Cumulative probability of the residence time distribution for FtsZ*[T108A]-YFP-mts (closed squares). In the same plot the photobleaching timescale of fixed nanobodies is shown (empty inverted triangles).

A.2 Scripts

```
1 function [] = Kymo_scriptX_Fourier(tseries , z_proj)
2 % Script written by Diego Ramirez in collaboration with Daniela
   Garcia
3 % MPI Martisried , 2015
4
5 %proj_stack , z-projection of stack , 10 with average intensity is
   more than
6 %enough
7 %stack , acquisition treated with filter mean = 2 pixels
8
9
10 %DistancePix=37.940;
11 %TIRF-corefacility , 1/14.779
12 %Confocal , 1/37.940 Zoom10X
13 %Confocal , 1/22.764 Zoom6X
14
15 %Check number and filenames!!!
16 %pixel_size=1/DistancePix;
17 pixel_size=0.0423; % micrometers
18 time=3; %seconds
19 doBackSubtraction = true;
20
21 %declaration of length of outcome size vector from analysis slope
22 k_len=50;
23
24 stack = tseries;
25 proj_stack = z_proj;
26
27 prompt = {'Pixel size (microns):', 'Time interval (s):'};
28 dlg_title = 'Input parameters';
29 num_lines = 1;
30 defaultans = {num2str(pixel_size), num2str(time)};
31 answer = inputdlg(prompt, dlg_title , num_lines , defaultans);
32 pixel_size = str2num(answer{1});
33 time = str2num(answer{2});
34
35 choice = questdlg('Subtract average profile from final kymograph?
   ', ...
36     'Background subtraction', ...
37     'Yes', 'No', 'Yes');
```

A.2 Scripts

```
38 % Handle response
39 switch choice
40     case 'Yes'
41         doBackSubtraction = true;
42     case 'No'
43         doBackSubtraction = false;
44 end
45
46
47 % general settings
48 doInterpolation = true;
49 interpMeth = 'linear';
50 sampl = 1.5; %oversampling factor of kymograph (pixels)
51 off=1;
52
53 tsStack = tiffread(stack);
54 Im=imread(proj_stack);
55
56 %Open figure to select ring/points
57 figure
58 imshow(Im);
59 [y0,x0,p0] = impixel();
60 close;
61
62 for j=1:1:length(x0)/2
63     %Read the averaged image
64     I=imread(proj_stack);
65     %Get the radius of the selected ring
66     r=round(sqrt((x0(2*j-1)-x0(2*j))^2+(y0(2*j-1)-y0(2*j))^2)+2);
67
68
69     try
70     B=I(x0(2*j-1)-r:x0(2*j-1)+r, y0(2*j-1)-r:y0(2*j-1)+r);
71     Borig = B;
72     catch exception
73     continue
74 end
75 %B=Im(x0(2*j-1)-(r+offset):x0(2*j-1)+(r+offset), y0(2*j-1)-(r+
76     offset):y0(2*j-1)+(r+offset));
77
78 %GCA: Mask corners of cropped image
79 [height, width] = size(B);
80 centerW = width/2;
```



```
80 centerH = height/2;
81 radius = (centerW+centerH)/2;
82 [W,H] = meshgrid(1:width,1:height);
83 Bback = (mean2(B)+min(min((B))))/2;
84 %B(((W-centerW).^2 + (H-centerH).^2) > (radius*radius)) = Bback;
85 hanning2d=0.5*(1-cos(2*pi*(0:width-1)/(width-1)))*0.5*(1-cos(2*
      pi*(0:width-1)/(width-1)));
86 B = uint16((single(B-Bback).*hanning2d) + single(Bback));
87
88 %Threshold value, highest intensity
89 thresh = multithresh(B);
90
91 %imshow(B);
92 tam=size(B);
93
94 out=real(LMA(xy_fit,initial));
95
96 th = 0:delta:2*pi;
97
98 if( ~doInterpolation)
99 xunit_1 = round((out(3)) * cos(th) + out(1));
100 yunit_1 = round((out(3)) * sin(th) + out(2));
101 xunit_2 = round((out(3)-off) * cos(th) + out(1));
102 yunit_2 = round((out(3)-off) * sin(th) + out(2));
103 xunit_3 = round((out(3)-2*off) * cos(th) + out(1));
104 yunit_3 = round((out(3)-2*off) * sin(th) + out(2));
105
106 else
107 xunit_1 = (out(3)) * cos(th) + out(1);
108 yunit_1 = (out(3)) * sin(th) + out(2);
109 xunit_2 = (out(3)-off) * cos(th) + out(1);
110 yunit_2 = (out(3)-off) * sin(th) + out(2);
111 xunit_3 = (out(3)-2*off) * cos(th) + out(1);
112 yunit_3 = (out(3)-2*off) * sin(th) + out(2);
113 end
114
115 %Plot in the original image. It corresponds to the circle in _1
116 xunit_4 = round((r) * cos(th)) + y0(2*j-1);
117 yunit_4 = round((r) * sin(th)) + x0(2*j-1);
118
119 %Area selected plot
120 figure
121 subplot(1,2,1),
```

A.2 Scripts

```
122 imshow(Borig);
123
124 hold on
125 plot(xunit_1 , yunit_1 , xunit_2 , yunit_2 , xunit_3 , yunit_3 , '-');
126 hold off
127
128 subplot(1,2,2)
129 imshow(I);
130
131 hold on
132 plot(xunit_4 , yunit_4 , '-');
133 hold off
134
135 %Save plot
136 s=num2str(j);
137 print(s, '-dpng');
138 close;
139
140 %Same size as unit_1 since xunit_1 and yunit_1 are being printed
141 diameter_dfs=zeros(1,length(xunit_1));
142 kymograp = zeros(size(tsStack,3),length(xunit_1));
143 kymograp2 = zeros(size(tsStack,3),length(xunit_2));
144 kymograp3 = zeros(size(tsStack,3),length(xunit_3));
145
146 kymograp_mean = zeros(size(tsStack,3),length(xunit_1));
147
148 kymograp_zero1 = zeros(size(tsStack,3),length(xunit_1));
149 kymograp_zero2 = zeros(size(tsStack,3),length(xunit_2));
150 kymograp_zero3 = zeros(size(tsStack,3),length(xunit_3));
151
152 C=tsStack(1).data;
153
154 Im_ref=C(x0(2*j-1)-r:x0(2*j-1)+r , y0(2*j-1)-r:y0(2*j-1)+r);
155
156
157 for i = 1:size(tsStack,2)
158
159
160
161 A=tsStack(i).data;
162
163 Im=A(x0(2*j-1)-r:x0(2*j-1)+r , y0(2*j-1)-r:y0(2*j-1)+r);
164 if( ~doInterpolation)
```

```
165         lin_ind = sub2ind(size(Im),yunit_1,xunit_1);
166         kymograp(i,:)= Im(lin_ind);
167     else
168     %GCA: interpolate values
169         kymograp(i,:) = interp2(im2double(Im),xunit_1,yunit_1,
170             interpMeth);
171     end
172     if( ~doInterpolation)
173         kymograp_zero1(i,:)=Im_ref(lin_ind);
174     else
175     %GCA: interpolate values
176         kymograp_zero1(i,:) = interp2(im2double(Im_ref),xunit_1,
177             yunit_1,interpMeth);
178     end
179     if( ~doInterpolation)
180         lin_ind = sub2ind(size(Im),yunit_2,xunit_2);
181         kymograp2(i,:)= Im(lin_ind);
182     else
183         kymograp2(i,:) = interp2(im2double(Im),xunit_2,yunit_2,
184             interpMeth);
185     end
186     if( ~doInterpolation)
187         kymograp_zero2(i,:)=Im_ref(lin_ind);
188     else
189         kymograp_zero2(i,:) = interp2(im2double(Im_ref),xunit_2,
190             yunit_2,interpMeth);
191     end
192     if( ~doInterpolation)
193         lin_ind = sub2ind(size(Im),yunit_3,xunit_3);
194         kymograp3(i,:)= Im(lin_ind);
195     else
196         kymograp3(i,:) = interp2(im2double(Im),xunit_3,yunit_3,
197             interpMeth);
198     end
199     if( ~doInterpolation)
200         kymograp_zero3(i,:)=Im_ref(lin_ind);
201     else
202         kymograp_zero3(i,:) = interp2(im2double(Im_ref),xunit_3,
203             yunit_3,interpMeth);
204     end
205     end
206     end
```

A.2 Scripts

```
202
203 try
204
205 kymograp_mean=(kymograp+kymograp2+kymograp3)/3;
206 %GCA subtract the average time profile from each kymograph
207 if (doBackSubtraction)
208     kymograp_mean = kymograp_mean - repmat(mean(kymograp_mean,2)
209         ,1,size(kymograp_mean,2));
209 end
210
211 kymograp_mean=mat2gray(kymograp_mean);
212 kymograp=mat2gray(kymograp);
213 kymograp2=mat2gray(kymograp2);
214 kymograp3=mat2gray(kymograp3);
215
216 s_B=size(kymograp_mean,1)-k_len+1;
217
218 diameter=zeros(1,s_B);
219 vel=zeros(1,s_B);
220 vel_a=zeros(2,s_B);
221 %vel_a=zeros(1,s_B);
222 diameter(1)=2*out(3)*pixel_size;
223 diameter_dfs(1)=2*out(3)*pixel_size;
224
225 l=size(tsStack,2)+7;
226 %Save kymograph
227 figure
228 subplot(1,3,1)
229 imshow(kymograp);
230
231 subplot(1,3,2)
232 imshow(kymograp2);
233
234 subplot(1,3,3)
235 imshow(kymograp3);
236
237 print(strcat(s,'kymo_mean'),'-dpng');
238 close
239
240
241 figure
242
243 imshow(kymograp_mean);
```

A.2 Scripts

```
244 print(strcat(s, 'kymo_meanV_raw'), '-dpng');
245
246 close;
247
248 kymograp_mean = sgolayfilt(kymograp_mean, 2, 5);
249 kymograp_mean = adapthisteq(kymograp_mean);
250 figure
251 imshow(kymograp_mean);
252
253
254 p = impoly(gca);
255 pos = wait(p);
256
257 if (isempty(p) == 0)
258
259
260     m= abs((pos(2,1) - pos(1,1)))/abs((pos(2,2) - pos(1,2)));
261
262     %Turn pix/seg to um/min
263     v = 60*pixel_size/sampl*m/(time);
264     vel(1) = v;
265
266     tx = text(50,1,sprintf('V = %d um/min', vel(1)));
267     set(tx, 'FontSize', 10);
268     print(strcat(s, 'kymo_meanV'), '-dpng');
269     close;
270
271     vel_a=slope_analysis(kymograp_mean, pixel_size, sampl);
272
273     t_t=table([xunit_1', yunit_1']);
274     writetable(t_t, strcat(s, 'kymo_mean.txt'), 'Delimiter', '\t');
275
276
277     %Filter to exclude some of the measurements
278     %First find number of -1 values
279     minus = length(find(vel_a(2,:) == -1));
280     %Find the Inf
281     nInf = length(find(vel_a(2,:) == Inf));
282     %Find positive
283     positive = length(find(vel_a(2,:) > -1));
284
285     if(minus >= 60 | nInf <= 5 | nInf >= 100 | positive >=
        10)
```

A.2 Scripts

```
286         t_b=table([diameter ', vel ', vel_a(1,:) ', vel_a(2,:) ']);
287         writetable(t_b, strcat(s, 'kymo_vel.txt'), 'Delimiter', '\t')
288         ;
289         end
290     else
291
292         close;
293         t_t=table([xunit_1 ', yunit_1 ', diameter_dfs ']);
294
295     end
296
297     catch exception
298     close all;
299     continue
300     end
301
302 end
303
304 end
```

Appendix B

Appendix to chapter V

B.1 Figures

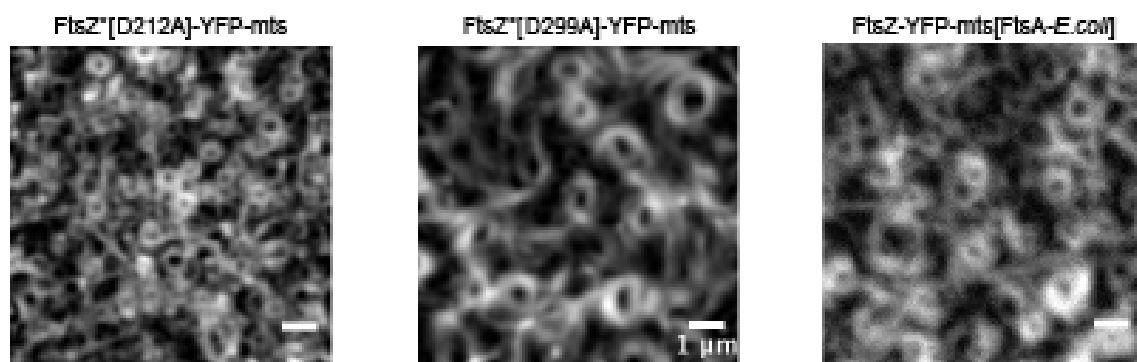


Figure B.1: Representative snapshots of the *in vitro* reconstitution of each mutant. Each variant is able to self-organise into FtsZ rings

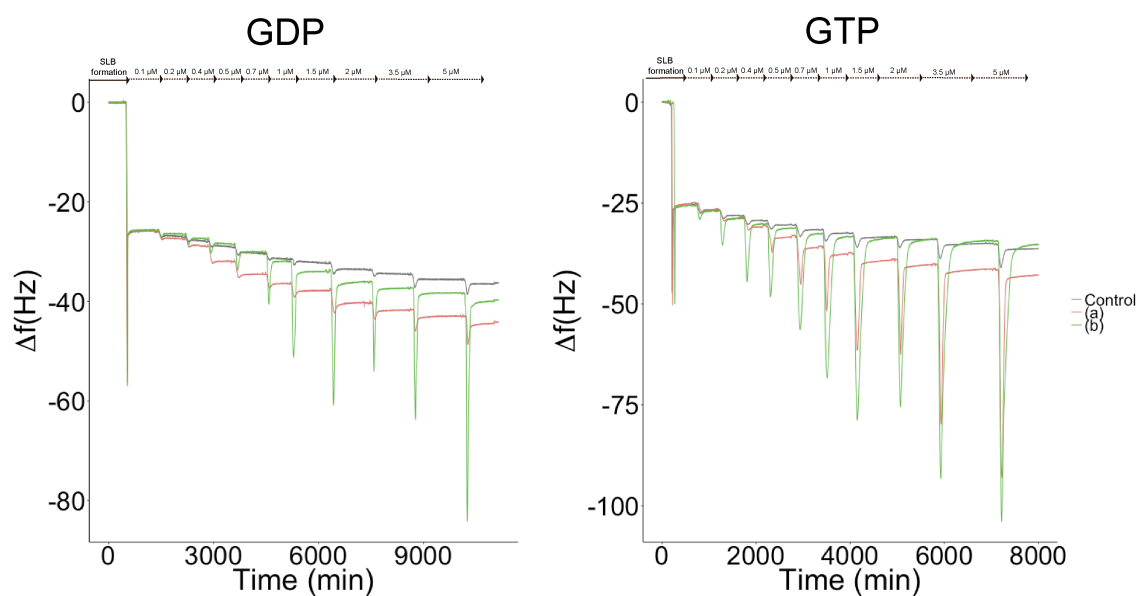


Figure B.2: An SLB of DOPC:DOPG, 70:30 mol % was formed on a silicon dioxide-coated surface of a quartz crystal. In our experiments, we added different concentrations of the three mts variants and measured the frequency (Δf). The plots show that the different variants can be absorbed on the membrane and further measurements are possible after almost complete removal of the protein added. The FtsZ solutions contained 50 mM Tris-HCl at pH 7.5, 150 mM KCl, 4 mM GDP or 4 mM GTP and 5 mM Mg^{2+} .

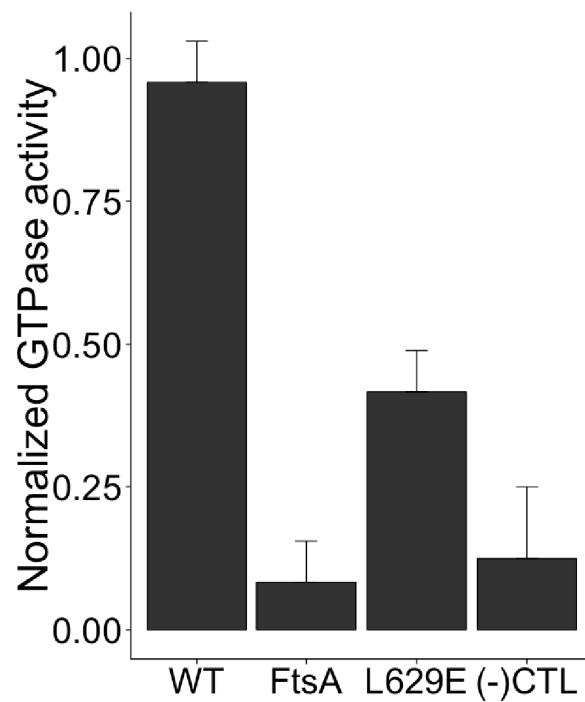


Figure B.3: Normalized GTPase activity of the rest of the chimera protein used in this study. All the different proteins show reduced GTPase activity when compared with the chimera with the WT moiety.

B.2 Tables

| Condition | FtsZYFPmts[MinD] | FtsZYFPmts*[L629E] |
|--------------------------------------|------------------|--------------------|
| buffer | 5.59 S | 2.8 S |
| buffer + 4 mM GTP | 7.5 S | 2.7 S |
| buffer + 5 mM Mg ²⁺ | 5.8 S | 3.9 S |
| buffer + 4 mM GTP + Mg ²⁺ | 11.1 S | 4.9 S |

Table B.1: Distribution of sedimentation coefficients obtained from sedimentation velocity analysis of FtsZ-YFP-mts and FtsZ-YFP-mt*[L629E]. In the presence of both GTP and Mg²⁺ the sedimentation-velocity profile shows that both proteins are polydisperse, polymers of different size are present. Only when GTP is present a main peak is observed in the sample, comparable to monomeric protein. When Mg²⁺ is only present, we observed a single main peak, but also some oligomers are present in the samples. In general, the chimera protein *[L629E] tend to stay in a monomer form, forming short oligomers when both GTP and Mg²⁺ are present.

Appendix C

Appendix to chapter VI

C.1 Figures

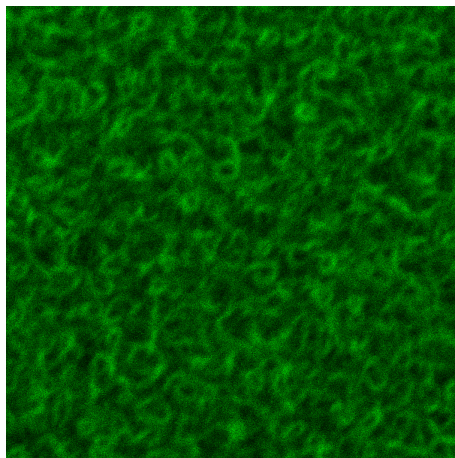


Figure C.1: Confocal microscopy shows that FtsZ-YFP-mts can self-organise into dynamic rings on supported lipid bilayers containing EggPG:DOPC, 80:20 mol %

Appendix D

Appendix to chapter VII

D.1 Figures

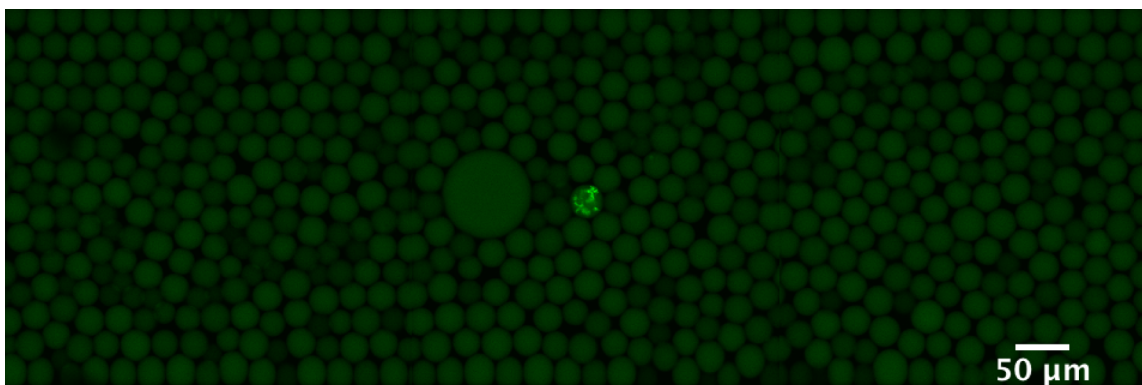


Figure D.1: Representative snapshot of FtsZ polymerization upon a Mg^{2+} titration. FtsZ filaments formation are less likely to be observed due to the absence of membrane.

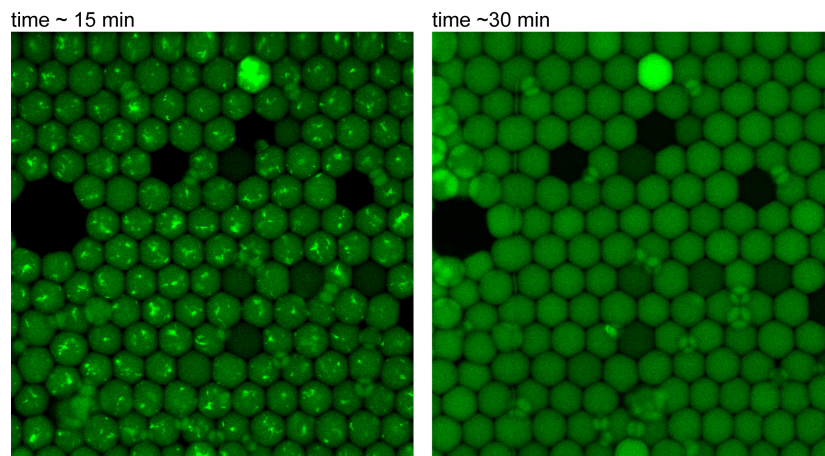


Figure D.2: Confocal microscopy shows the rapid disassemble of FtsZ filaments inside droplets in the presence of Ficoll

D.2 Scripts

```
1 %Adapted from Baccouche, A., Okumura, S., Sieskind, R., Henry,
   , Henry,
2 %E., Aubert-Kato, N., Bredeche, N., Genot, A. J. (2017).
3 %Massively parallel and multiparameter titration of biochemical
   assays
4 %with droplet microfluidics. Nature Protocols, 12(9), 1912-1932.
5
6 %this script extracts the fluorescence intensities of droplets
   for 2D
7 %experiment for 1D or 3D experiments, adjust the script
8
9
10 %Add new file here
11 file = 'file_stack';
12 dropletradius=20; % average radius of the droplet, to be
   determined manually
13
14 %define here the minimum and maximum concentration of reagents 1
   and 2.
15 c1min=0;
16 c1max=50;
17 c2min=0;
18 c2max=100;
19
20 %define the minimum and maximum level of reporter (this is an
   arbitrary unit
21 %as the precise concentration will depend on the reporter that is
22 %considered
23 reportermin=0;
24 reportermax=1;
25 normalisationMatrix=[ c1min, c1max;c2min,c2max;reportermin,
   reportermax];
26
27
28 %take the stacked tiff and load each stack image.
29 %by convention, the first image of the stack corresponds to the
   first barcode, the
30 %second image to the second barcode and the last image to the
   reporter
31
```

```
32 iamgefile=strcat(file, '.tif'); %name of the image file
33 barcode1=imadjust(imread(iamgefile,1)); %Fisrt stack is Mg2+ -
    Alexxa 647
34 barcode2=imadjust(imread(iamgefile,3)); %First stack correspondes
    to MM - cascade blue
35 reporter=imadjust(imread(iamgefile,2)); %Second stack is the
    reporter - GFP
36
37
38 %Detect disks in the image. First the barcode images are combined
    to improve
39 %the contrast of droplets. Then matlab detects disks in the
    composite image whose
40 %radius lies within the allotted bounds: 60% and 140% of the
    defined radius
41 %Note: it is important to adjust the sensitvity parameter to
    detect as many
42 %droplets as possible.
43
44 [centers, radii, metric] = imfindcircles((barcode1+barcode2+
    reporter),[0.7*dropletradius, 1.3*dropletradius], 'Sensitivity',
    0.90);
45 data = table(centers);
46 writetable(data, strcat(file, '_centers.txt'), 'Delimiter', '\t');
47
48 data = table(radii);
49 writetable(data, strcat(file, '_radii.txt'), 'Delimiter', '\t');
50
51
52 diskfilter = fspecial('disk',0.8*dropletradius); %define a disk
    filter for image convolution. It integrates
53 % the fluoresce over a radius of 80%
54
55 %convolve the primary image with the diskfilter. This creates a
    new images
56 %that locally integrates fluorescence.
57 barcode1convolved = imfilter(barcode1, diskfilter, 'replicate');
58 barcode2convolved = imfilter(barcode2, diskfilter, 'replicate');
59 reporterconvolved = imfilter(reporter, diskfilter, 'replicate');
60 %reporterconvolved = ones (size (barcode1));
61
62 %Extraction of droplet intensities in each channel by taking the
    pixel
```

```
63 %value at the center of the droplet in the convolved image (which
    has
64 %already integrated intensities.
65 %the floor function is necessary to work with integer values of
    coordinates
66 intensity=zeros(length(centers),3);
67 %x_centers=zeros(length(center),3);
68 %y_centers=zeros(length(center),3);
69
70
71 for i=1:length(centers)
72
73     intensity(i,1)=barcode1convolved(floor(centers(i,2)),floor(
        centers(i,1)));
74     intensity(i,2)=barcode2convolved(floor(centers(i,2)),floor(
        centers(i,1)));
75     intensity(i,3)=reporterconvolved(floor(centers(i,2)),floor(
        centers(i,1)));
76 end
77 data=table([intensity]);
78 writetable(data, strcat(file, '_intensity.txt'), 'Delimiter', '\t');
79 %
80 %Normalization of fluo intensities
81 intensitynormalized=intensity;
82 epsilon_quantile=0.01; %quantile to use to normalize intensity.
    By default the top 99% and bottom 1% serves to set the 0 and 1
    levels of normalized intensities
83
84
85 %Conversion of fluorescence intensities into concentration.
86 for i=1:3
87     intensitynormalized(:,i)=normalisationMatrix(i,1)+
        normalisationMatrix(i,2)*(intensity(:,i)-quantile(
            intensity(:,i),epsilon_quantile))/(quantile(intensity(:,i)
            ,1-epsilon_quantile)-quantile(intensity(:,i),
            epsilon_quantile));
88 end
89
90 data=table([intensitynormalized]);
91 writetable(data, strcat(file, '_intensitynormalized.txt'), '
    Delimiter', '\t');
92
93 % construct an array that contains the colors of each droplet
```



```
    according to
94 % its level of reporter , low reporter gives dark points , high
    reporter gives
95 % red points . This array of colour will serve for the final plot
96 colorfromReporter=zeros(length(intensitynormalized(:,3)),3);%
    prepare a matrix where the RGB values are stored
97 clippedReporter=max(0,min(intensitynormalized(:,3),1)); %the min
    and max ensures that the resulting values ends up between 0
    and 1

98
99 for i=1:length(colorfromReporter)
100 colorfromReporter(i,1)=clippedReporter(i);
101 end
102
103
104 a = figure;
105 subplot(4,1,1)
106 scatter(intensity(:,1), intensity(:,2))
107 hold on
108 title('Initial fluo. ');
109 xlabel('Barcode1 fluo. (a.u.) ');
110 ylabel('Barcode2 fluo. (a.u.) ');
111 %
112 %this plots the measured fluorescence intensities in the space (
    barcode 1, barcode 2).
113 subplot(4,1,2)
114 hist(intensity(:,1))
115 hold on
116 title('Hist Barcode1');
117 xlabel('Droplet intensity (a.u.) ');
118 ylabel('Droplet cout');
119
120 subplot(4,1,3)
121 hist(intensity(:,2))
122 hold on
123 title('Hist Barcode2');
124 xlabel('Droplet intensity (a.u.) ');
125 ylabel('Droplet cout');
126
127 subplot(4,1,4)
128 hist(intensity(:,3))
129 hold on
130 title('Hist Reporter');
```

```
131 xlabel('Droplet intensity (a.u.)');
132 ylabel('Droplet cout');
133
134
135 %We now plot the results
136 %Reagents against reporter
137 %this plot shows the detected droplets. Inspect for verifying
    quality of detection.
138 %Adjust sensitivity if needed to detect more droplets
139 b = figure;
140 subplot(1,2,1)
141 imshow(barcode1)
142 viscircles(centers , radii , 'EdgeColor' , 'b');
143
144 %this plots the measured fluorescence intensities in the space (
    barcode 1, barcode 2).
145 subplot(1,2,2)
146 sizepoints=20; %adjust the size of points if needed
147 scatter(intensitynormalized(:,1),intensitynormalized(:,2),
    sizepoints , 'black' , 'filled') %
148 hold on
149 title('Titration of reagent 1 and reagent 2');
150 %axis ([0 110, 0 110])
151 xlabel('Dextran 647 [%]');
152 ylabel('Dextran Cascade Blue [%]');
153
154
155 %Reporter against Mg2+
156 c = figure;
157 subplot(1,2,1)
158 imshow(reporter)
159 viscircles(centers , radii , 'EdgeColor' , 'b');
160
161 %this plots the measured fluorescence intensities in the space (
    barcode 1, barcode 2).
162 subplot(1,2,2)
163 sizepoints=20; %adjust the size of points if needed
164 scatter(intensitynormalized(:,1),intensitynormalized(:,3),
    sizepoints , colorfromReporter , 'filled') %
165 hold on
166 title('effect of Mg2+ on the level of reporter');
167 %axis ([0 110, 0 110])
168 xlabel('[reagent 1](nM)');
```

```
169 ylabel( '[reporter](nM) ' );
170
171
172 %Reporter against MM
173 d = figure;
174 subplot(1,2,1)
175 imshow(barcode2)
176 viscircles(centers , radii , 'EdgeColor' , 'b' );
177
178 %this plots the measured fluorescence intensities in the space (
    barcode 1, barcode 2).
179 subplot(1,2,2)
180 sizepoints=20; %adjust the size of points if needed
181 scatter(intensitynormalized(:,2) , intensitynormalized(:,3) ,
    sizepoints , colorfromReporter , 'filled' ) %
182 hold on
183 title( 'effect of MasterMix on the level of reporter' );
184 %axis ([0 110, 0 110])
185 xlabel( '[reagent 2](nM) ' );
186 ylabel( '[reporter](nM) ' );
187
188
189 %Save figures
190 savefig(a, strcat(file , '_test.fig' ))
191 print(a, strcat(file , '_test' ) , '-dpng' );
192 %close(a);
193
194 savefig(b, strcat(file , '_bar1bar2.fig' ))
195 print(b, strcat(file , '_bar1bar2' ) , '-dpng' );
196 %close(b);
197
198 savefig(c, strcat(file , '_bar1rep.fig' ))
199 print(c, strcat(file , '_bar1rep' ) , '-dpng' );
200 %close(c);
201
202 savefig(d, strcat(file , '_bar2rep.fig' ))
203 print(d, strcat(file , '_bar2rep' ) , '-dpng' );
204 %close(d);
205
206 %CORRELATION COEFFICIENT
207 [R, P] = corrcoef(intensitynormalized(:,1) , intensitynormalized
    (:,2) )
208 cR = table([R]);
```

D.2 Scripts

```
209 cP = table([P]);
210
211 writetable(cR, strcat(file, '_cR.txt'), 'Delimiter', '\t');
212 writetable(cP, strcat(file, '_cP.txt'), 'Delimiter', '\t');
213
214
215 %%%%For FtsZ analysis%%%%
216
217 %%%%Get edges, intensities that correlate to filaments%%%%
218 reporterBW = edge(reporter, 'canny');
219 figure;
220 imshow(reporterBW);
221
222 x0 = round(centers(:,1));
223 y0 = round(centers(:,2));
224 r = round(radii);
225
226 %i=1;
227 values = zeros(length(r),1);
228 intensityBW=zeros(length(r),1);
229
230 for i = 1:1:length(r)
231     [W,H] = meshgrid(x0(i)-r(i):x0(i)+r(i),y0(i)-r(i):y0(i)+r(i))
232         ;
233     values(i,1) = mean(mean(impixel(reporterBW, W,H)));
234
235 end
236
237 intensityBW=0+1*(values-quantile(values, epsilon_quantile))/(
238     quantile(values,1-epsilon_quantile)-quantile(values,
239     epsilon_quantile));
240
241 colorfromReporter=zeros(length(intensityBW),3);%prepare a matrix
242     where the RGB values are stored
243 clippedReporter=max(0,min(intensityBW,1)); %the min and max
244     ensures that the resulting values ends up between 0 and 1
245
246 for i=1:length(colorfromReporter)
247     colorfromReporter(i,2)=clippedReporter(i);
248 end
249
250 %intensitynormalized(:,1), Mg
```

```
247 z = figure;
248 scatter(intensitynormalized(:,1),intensityBW,sizepoints,
          colorfromReporter,'filled')%
249 title('effect of Mg2+ on the level of reporter');
250 %axis ([0 110, 0 110])
251 xlabel('[reagent 1](nM)');
252 ylabel('[reporter](nM)');
253
254 %intensitynormalized(:,2), Ficoll
255 y = figure;
256 scatter(intensitynormalized(:,2),intensityBW,sizepoints,
          colorfromReporter,'filled')%
257 title('effect of MasterMix on the level of reporter');
258 %axis ([0 110, 0 110])
259 xlabel('[reagent 2](nM)');
260 ylabel('[reporter](nM)');
261
262 %%%%%%%%%%%Plot on image, Mg2+ dependence%%%%%%%%%%
263 mg = intensitynormalized(:,1);
264
265
266 %Mg low and high
267 low_idx = find(mg <= 50);
268 high_idx = find(mg >= 50);
269
270 b = figure;
271 subplot(2,2,[1 2])
272 imshow(reporterBW);
273
274 viscircles(centers(low_idx,:), radii(low_idx), 'Color','k');
275 viscircles(centers(high_idx,:), radii(high_idx), 'Color','b');
276
277 hold on
278 %Plot also histogram of intensities
279 subplot(2,2,3)
280 histogram(intensityBW(low_idx), 'FaceColor','k', 'EdgeColor','k
          ');
281 title('FtsZ raw intensity at low Mg');
282 xlabel('Droplet intensity (a.u.)');
283 ylabel('Droplet count');
284
285 %Plot also histogram of intensities
286 subplot(2,2,4)
```

```
287 histogram(intensityBW(high_idx), 'FaceColor', 'b', 'EdgeColor', '
    b');
288 title('FtsZ raw intensity at high Mg');
289 xlabel('Droplet intensity (a.u.)');
290 ylabel('Droplet count');
291
292 hold off
293
294 %%%%%%%%%%%Plot on image, Ficollo dependence%%%%%%%%%%
295 ficoll = intensitynormalized(:,2)*2;
296
297
298 %Ficoll low and high
299 low_idx = find(ficoll <= 100);
300 high_idx = find(ficoll >= 100);
301
302 b = figure;
303 subplot(2,2,[1 2])
304 imshow(reporterBW);
305
306 viscircles(centers(low_idx,:), radii(low_idx), 'Color', 'k');
307 viscircles(centers(high_idx,:), radii(high_idx), 'Color', 'r');
308
309 hold on
310 %Plot also histogram of intensities
311 subplot(2,2,3)
312 histogram(intensityBW(low_idx), 'FaceColor', 'k', 'EdgeColor', 'k
    ');
313 title('FtsZ raw intensity at low Ficoll');
314 xlabel('Droplet intensity (a.u.)');
315 ylabel('Droplet count');
316
317 %Plot also histogram of intensities
318 subplot(2,2,4)
319 histogram(intensityBW(high_idx), 'FaceColor', 'r', 'EdgeColor', '
    r');
320 title('FtsZ raw intensity at high Ficoll');
321 xlabel('Droplet intensity (a.u.)');
322 ylabel('Droplet count');
323
324 hold off
```

Acronyms

AFM Atomic Force Microscopy.

ATP Adenosine triphosphate.

BCA Bicinchoninic acid.

CFE Cell-free expression.

CTL C-terminal linker.

DOPC Dipalmitoylphosphatidylcholine.

DOPG 1,2-Dioleoyl-sn-glycero-3-phosphoglycerol.

EggPC Egg phosphatidylcholine.

FRAP Fluorescence Recovery After Photobleaching.

GDP Guanosine diphosphate.

GFP Green fluorescent protein.

GTP Guanosine triphosphate.

GUV Giant unilamellar vesicles.

IPTG Isopropyl β -D-1-thiogalactopyranoside.

PBP1b Penicillin-binding protein 1b.

PCA 3,4-protocatechuic acid.

PCD Protocatechuate-dioxygenase.

PDMS Poly-(dimethyl)-siloxane.

PG Peptidoglycan.

Acronyms

PURE Protein synthesis using recombinant elements.

SLB Supported lipid bilayers.

SPR Surface Plasmon Resonance.

SUV Small unilamellar vesicles.

TIRFM Total Internal Reflection Fluorescence Microscopy.

Acknowledgments

This thesis is the end of a long, long journey that started back in Mexico and went across 4 different countries. During the bachelor I got the ultimate goal to do my PhD at a Max-Planck Institute, and here I am, after 4 years in Germany and 6 years away from home, I managed to accomplish my dream.

I would like to thank to Petra, she opened her doors multiple times, first as an intern and second as a PhD student. Thanks for the freedom. I would like to thank the Schwillle Lab. Thank you so much Sigi for keeping the membrane lab pristine, to Michaella and Katharina for all the cloning help, to Kerstin and Bea for all the protein help. To Frank, Micha, Kristina and Lei for all the help and fruitful discussions. To all the people I have the chance to work with, special thanks to the DDA team.

Thanks a lot to QBM and my QBM family. Big thanks to Vicente, Andrea, Madlin, Linda, Laia, Alena, Victor, Elena, Gökçen, Basak, Rahmi; for all the great memories, for unforgettable PhD retreats (and our short holidays in Italy) and for the many times we met in Munich.

Vielen Dank an Leo und Alex, für die Musik, den Tanz und das Glück (Bier), die wir gemeinsam geteilt haben. Ohne dich wären meine Wochenenden wirklich langweilig gewesen. Auch Leo für alle gemeinsamen Mahlzeiten am MPI und die Hilfe bei der Arbeit.

Muchas gracias a Ariadna, por haber sido mi guía en todo este camino, por enseñarme con paciencia muchas cosas nuevas no solo en Múnich, sino también Dresden. Muchas, muchas gracias a Ana, que me llenaba de energía con cada visita a Múnich, y porque logramos sobrevivir a ese, nuestro paper, por todos esos días de plática. Muchas gracias a mi lab extendido en Madrid, muchas gracias a Germán por darme la bienvenida no solo en su laboratorio sino también en su casa. Gracias Germán también por toda la guía y los consejos.

Muchas gracias a la comunidad hispana en el MPI y por todos esos alimentos que compartimos juntos. Muchísimas gracias a Maria Antonia, Araceli, Favio y Natalia por estar siempre ahí con una sonrisa.

Ahora vienen los agradecimientos a mi raza genómica. Muchas gracias a los genómicos en Múnich, en especial a Ilse por todos esos días de desestrez. Millones de gracias a mis genómicos, en especial a Sama y Mayela porque siempre, a pesar de la distancia, estar ahí, leyendonos a diario. A ustedes también Marquito, Amhed y Yuvia, y todos esos encuentros en europa que estos años nos ha dejado.

Muchas gracias a todos mis amigos que sigue en México, por hacerme sentir como en

Acknowledgments

casa cada visita. Muchas gracias a Massiel porque sin su entrenamiendo no habría sobrevivido nunca. Muchas gracias a Paty, Karen, Natalia, Katty, Daniel, Jannu, Gina y todos aquellos que siempre buscarón tiempo para verme cuando visitaba la tierra prometida.

Muchisimas gracias a mi familia. A mi madre Norma y mi padre Miguel por todo su apoyo. A mis abuelos Cruz, Miguel Ángel, Cris y Miguel por todo su amor. A mis tías, primos y primas. Gracias a los que ya se nos adelantaron, tío Ángel esto va por tí. Muchas, muchas gracias a mi hermana Evelyn Adalia, por siempre estar ahí, por cuidarme y enseñarme muchas cosas nuevas. Tenemos muchas aventuras por delante.

Slutligen så vill jag tacka Erik för att han har varit en del av den här resan. Jag vill tacka honom för hans tålmod och att han alltid får mig att komma hem tack vare hans fantastiska mat. Tack för all glädje du gett mig under denna tiden och all glädje du kommer ge mig i framtiden.

Thank you all the people who have been part of this journey!

Danke allen Leuten, die Teil dieser Reise waren!

Gracias a todos los que compartieron este viaje (o malviaje) conmigo!

Jag vill tacka alla som har varit med på den här resan!